Dynamics of the Jovian Atmosphere from Observation and Theory

Thesis by

Liming Li

In Partial Fulfillment of the Requirements

for the Degree of

Doctor of Philosophy

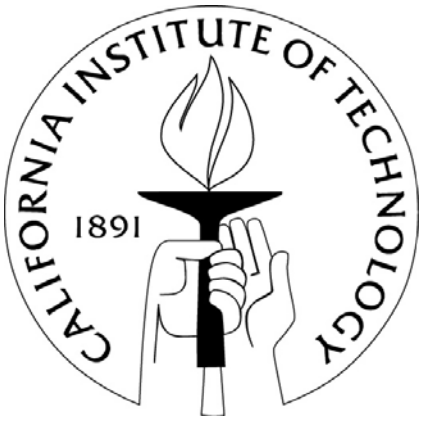

California Institute of Technology

Pasadena, California

2006

(Defended September 8, 2006)

Acknowledgements

I would like to thank the many people without whom this thesis would not have been possible. Foremost is my advisor, Andrew P. Ingersoll, whom I thank for his insightful guidance and generous support. I also want to thank Ashwin R. Vasavada, Shawn P. Ewald, Ulyana Dyudina, Yuk L. Yung, and the Cassini ISS team members for their support of my research.

I thank the Information Technology Services (ITS) staff Mike Black, and staff members Loreta Young, Leticia Calderon, Nora Oshima, and Irma Black for their support.

To all members of my family: thank you for all your encouragement and advice. This truly would have been impossible without you. It is to you that this thesis is dedicated.

Abstract

The atmospheric dynamics of Jupiter is studied by the Cassini observations and numerical models.

The multi-filter imaging data sets and the global thermal maps acquired by two instruments on Cassini — the Imaging Science Subsystem (ISS) and the Cassini Composite Infrared Spectrometer (CIRS) during the Jupiter flyby, are utilized to study atmospheric activities on Jupiter including small-scale spots, the Great Red Spot (GRS), the Dark Oval (DO), the vertical structure of zonal winds, and wave propagation. These new observations enrich the library of atmospheric activities and offer more clues and constraints on theoretical studies.

A reduced-gravity quasi-geostrophic (QG) model is combined with a parameterization of moist convections based on observations, to study the interaction between moist convection and zonal jets on Jupiter and Saturn. The numerical experiments support the idea that the zonal jets get their energy from moist convective events. Strong jets in Jupiter and Saturn, which violate the barotropic stability criterion, are reproduced by assuming westward flows in the deep underlying layer. Furthermore, our simulations suggest that the width and strength of jets on Jupiter and Saturn are controlled by the classical Rhines scale and a new velocity scale determined by characteristics of moist convection.

Contents

List of Figures

List of Tables

Overview

Jupiter is one of the giant planets, which are characterized by their massive fluid envelopes. The red giant has the most dynamic atmosphere in our solar system. The intensely turbulent atmosphere of the planet displays almost all important dynamic processes — lightning, storms, vortices, waves, clouds, jets, and so on. Some of these processes have a wide range of length scales. Examples include vortices ranging from the Great Red Spot (GRS) with a size larger than Earth to small eddies approaching the finest spacecraft resolution of a few tens of kilometers, waves ranging from planetary waves with horizontal wavelength on the order of 10,000 kilometers to gravity waves with wavelength on the order of 10-100 kilometers, and jets ranging from the strong equatorial jets with velocity larger than 100 m/s to the relatively weak high-latitude jets on the order of 10 m/s. Interestingly, the complicated jovian atmosphere has a simple dynamic environment since it has no mountain ranges, air-sea interfaces, and surface drag. The quasi-idealized dynamic environment means that some important dynamic principles can be identified more clearly, and some hypotheses in geophysical fluid dynamics can be tested more cleanly. This abundance of dynamic processes with a quasi-idealized environment make the jovian atmosphere an ideal laboratory of fluid mechanics that can not be achieved elsewhere.

Observation and theory are two important methods to study planetary sciences including atmospheric dynamics. Observations can constrain theories and offer clues to new theories. Theories can explain observations and point to the direction of further

observations. Numerical modeling is a powerful tool to validate theories and augment classical means of validation from laboratory experiments and observations. Observation and numerical modeling are becoming more active in the planetary sciences due to the advance of spacecraft observing time and computer time. From the first encounter with Jupiter by the Pioneer 10 and 11 in 1973 and 1974, to the grand tours of the twin Voyagers in 1979, to the 8-year (1995-2003) orbiting by the Galileo, to the Cassini's flyby in 2000, observations from spacecrafts continue to progress our understanding of the jovian atmosphere. Specifically, the lengthy 6-month observations with numerous instruments and high transmission rate, a large data storage capacity, and a wide spectral range enabled Cassini to acquire high-quality time-lapse data during its Jupiter flyby. These data have enriched our knowledge of the jovian atmosphere, and more studies associated with the new Cassini observation are still being conducted. On the other hand, many numerical models have been applied to study the jovian atmospheric dynamics including convective storms, vortices, and multiple jets since the Voyager time. These models range from deep convection models (Busse, 1976; Aurnou and Olson, 2001; Christensen, 2001; Heimpel *et al.,* 2005), to quasi-geostrophic (QG) models (singular layer or multi-lyaer) (Williams, 1979; Panetta, 1993; Marcus et al., 2000), to shallow water models (Dowling and Ingersoll, 1989; Cho and Polvani, 1996), to general circulation models (GCMs) (Dowling *et al*., 1998, 2006). The great success of these models suggests that numerical modeling plays an ever important role in the study of planetary sciences.

In this thesis, we utilize the observations from the Cassini Jupiter flyby and numerical

modeling to answer some important dynamic questions associated with vortices, waves, convective storms, jets, and interactions between them: What are the characteristics of small-scale vortices, and what is their interaction with the GRS? What are the vertical structures of zonal jets? Why are some planetary waves confined to specific latitudes and altitudes, and what are the generating mechanisms of these waves? What drives the jovian multiple jets, and what controls their width and strength? Why are some zonal jets stable even though they violate the barotropic stability criterion?

We processed the multi-filter imaging data sets acquired by the Cassini Imaging Science Subsystem (ISS), and combined these data with the global thermal maps constructed by the Cassini Composite Infrared Spectrometer (CIRS), to extensively study the atmospheric activity on Jupiter. In chapter 1 (Li *et al.*, 2004), we observed over 500 compact oval spots (vortices) including convective storms based on the 70-day continuum-band ISS images, and measured the distributions of their locations and lifetimes. The interaction between some compact oval spots and the GRS suggests a maintaining mechanism of the GRS. In chapter 2 (Li *et al.*, 2006a), the ISS multi-filter images are utilized to measure zonal winds at altitudes above and below the visible cloud deck. These are the first direct measurements of wind shear on Jupiter, confirming the inferences on high-altitude winds based on the thermal wind equation (Gierasch *et al*., 1986; Flasar *et al*., 2004) and extending the measurements on low-altitude winds from the Galileo probe (Atkinson *et al*., 1998). In chapter 3 (Li *et al.*, 2006b), the ISS images are combined with the vertical structures of zonal winds from Chapter 2 and the CIRS data, to discuss a North Equatorial Belt (NEB) wave. The 3-D zonal wind structures offer

a possible explanation of why the NEB wave is confined to specific latitudes and altitudes, and the calculation of the gradient of potential vorticity suggests that baroclinic instability is a possible generating mechanism of the NEB wave.

Based on these new observations on convective storms from Chapter 1 and other studies (Little, et al., 1999; Porco *et al.,* 2003), we suggest a new theory of the dynamic processes involving radiation, internal heat, convective storms, and zonal jets on Jupiter. In chapter 4 (Li *et al.,* 2006c), a reduced-gravity quasi-geostrophic model, with a parameterization of moist convection that is based on observations, is developed to validate the new theory. The theory demonstrates that an "inverse cascade" of energy, from small-scale motions to large-scale jets, can operate even when the small-scale convective storms on Jupiter occupy only 0.01% of the planet's surface area and are confined to latitudes where the vorticity is of one sign only. In addition, our experiments suggest that a velocity scale and a length scale, which are determined by characteristics of convective storms, control the strength and width of jets on Jupiter.

In order to get a broader perspective on the dynamics of the jovian atmosphere, some excellent reviews on the dynamics of the jovian atmosphere (Ingersoll, 1976, 1990; Marcus, 1993; Dowling, 1995; Marcus *et al*., 2000; Williams, 2002; 2003; Ingersoll et al., 2004; Vasavada and Showman, 2005) are recommended in a sense of the historical development.

References

Atkinson, D. H., J. B. Pollack, and A. Seiff, 1998. The Galileo Probe Doppler Wind Experiment: Measurement of the deep zonal winds on Jupiter, *J. Geophys. Res.* **103**, 22,911- 22,928**.**

Aurnou, J.M., Olson, P.L., 2001. Strong zonal winds from thermal convection in a rotating spherical shell. *Geophys. Res. Lett.* **28**, 2557-2559.

Busse, F.H., 1976. A simple model of convection in the jovian atmosphere. *Icarus* **29**, 255-260.

Cho, J.Y.K., Polvani, L.M., 1996. The morphogenesis of bands and zonal winds in the atmospheres on the giant outer planets. *Science* **273**, 335-337.

Christensen, U.R., 2001. Zonal flow driven by deep convection in the major planets. *Geophys. Res. Lett.* **28**, 2553-2556.

Dowling, T.E., Ingersoll, A.P., 1989. Jupiter's Great Red Spot as a shallow-water system. *J. Atmos. Sci.* **46**, 3256-3278.

Dowling et al., 1998. The explicit planetary isentropic-coordinate (EPIC) atmospheric model. *Icarus* **132**, 221-238.

Dowling et al., 2006. The EPIC atmospheric model with an isentropic/terrain-following hybrid vertical coordinate. *Icarus* **182**, 259-273.

Flasar, F. M., et al., 2004. An intense stratospheric jet on Jupiter, *Nature* **427**, 132-135.

Gierasch, P. J., B. J. Conrath, and J. A. Magalhaes, 1986. Zonal mean properties of Jupiter upper troposphere from Voyager infrared observations, *Icarus* **67**, 456 - 483.

Heimpel, M., Aurnou, J., Wicht, J., 2005. Simulation of equatorial and high-latitude jets on Jupiter in a deep convection model. *Nature* **438**, 193-196.

Ingersoll, A.P., 1976. The atmosphere of Jupiter. *Space Sci. Rev.* **18**, 603-609.

Ingersoll, A.P., 1990. Atmospheric dynamics of the outer planets, *Science* **248**, 308-315.

Ingersoll, A.P., Dowling, T.E., Gierasch, P.J., Orton, G.S., Read, P.L., Sanchez-Lavega, A., Showman, A.P., Simon-Miller, A.A., and Vasavada, A.R., 2004. Atmospheric dynamics. *Jupiter: The Planet, Satellites and Magnetosphere* ed F Bagenal *et al.* (New York: Cambridge University Press) pp 105-128.

Li, L., A. P. Ingersoll, A. R. Vasavada, C. C. Porco, A. D. Del Genio, S. P. Ewald, 2004. Life cycles of spots on Jupiter from Cassini images. *Icarus* **172**, 9-23.

Li, L., A. P. Ingersoll, A. R. Vasavada, A. A. Simon-Miller, A. D. Del Genio, S. P. Ewald, C. C. Porco, and R. A. West, 2006. Vertical wind shear on Jupiter from Cassini images. *Journal of Geophysical Research* **111**, doi:10.1029/2005JE002556.

Li, L., A. P. Ingersoll, A. R. Vasavada, A. A. Simon-Miller, R. K. Achterberg, S. P. Ewald, U. A. Dyudina, C. C. Porco, R. A. West, and F. M. Flasar, 2006. Waves in Jupiter's atmosphere observed by the Cassini ISS and CIRS instruments. In press.

Li, L., A. P. Ingersoll, X. L. Huang, 2006. Interaction of moist convection with zonal jets on Jupiter and Saturn. *Icarus* **180**, 113-123.

Marcus, P.S., 1993. Jupiter's Great Red Spot and other vortices. *Ann. Rev. Astron. Astrophys.* **31**, 523-573.

Marcus, P.S., Kundu, T. and Lee, C., 2000. Vortex dynamics and zonal flows. *Phys. Plasmas* **7**, 1630-1640.

Panetta, R.L., 1993. Zonal Jets in wide baroclinically unstable regions — Persistence and scale selection. *J. Atmos. Sci.* **50**, 2073-2106.

Vavavada, A.R., Showman, A.P., 2005. Jovian atmospheric dynamics: an update after Galileo and Cassini. *Rep. Prog. Phys.* **68**, 1935-1996.

Williams, G.P., 1979. Planetary circulation 2: Jovian quasi-geostrophic regime. *J. Atmos. Sci.* **36**, 932-968.

Williams, P.S., 2002. Jovian dynamics. Part II: The genesis and equilibration of vortex sets. *J. Atmos. Sci.* **59**, 1356-1370.

Williams, P.S., 2003. Jovian dynamics. Part III: Multiple, migrating, and equatorial jets. *J. Atmos. Sci.* **60**, 1270-1296.

Chapter 1: Life Cycles of Spots on Jupiter from Cassini Images

1.1 Abstract

Using the sequence of 70-day continuum-band (751 nm) images from the Cassini Imaging Science System (ISS), we record over 500 compact oval spots and study their relation to the large-scale motions. The ~100 spots whose vorticity could be measured — the large spots in most cases — were all anti-cyclonic. We exclude cyclonic features (chaotic regions) because they do not have a compact oval shape, but we do record their interactions with spots. We distinguish probable convective storms from other spots because they appear suddenly, grow rapidly, and are much brighter than their surroundings. The distribution of lifetimes for spots that appeared and disappeared during the 70-day period follows a decaying exponential with time constant (mean lifetime) of 3.5 days for probable convective storms and 16.8 days for all other spots. Extrapolating the exponential beyond 70 days seriously underestimates the number of spots that existed for the entire 70-day period. This and other evidence (size, shape, distribution in latitude) suggests that these long-lived spots with lifetime larger than 70 days are from a separate population. The zonal wind profile obtained manually by tracking individual features (this study) agrees with that obtained automatically by correlating brightness variations in narrow latitude bands (Porco *et al.* 2003). Some westward jets have developed more curvature and some have developed less curvature since Voyager times, but the number of westward jets that violate the barotropic stability criterion is about the same. In the northern hemisphere the number of spots is greatest at the latitudes of the westward jets, which are the most unstable regions according to the barotropic stability criterion. During the 70-day observation period the Great Red Spot (GRS) absorbed nine westward-moving spots that originated in the South Equatorial Belt (SEB), where most of the

probable convective storms originate. Although the probable convective storms do not directly transform themselves into westward-moving spots, their common origin in the SEB suggests that moist convection and the westward jet compose a system that has maintained the GRS over its long lifetime.

1.2 Introduction

Jupiter's atmosphere is full of spots — compact, oval-shaped cloud features whose appearance, at some wavelengths at least, is different from that of their surroundings. This contrast may reflect differences in composition or size of the cloud particles, differences in optical thickness or altitude of the cloud, or differences in small-scale texture of the cloud (Smith *et al.* 1979, Ingersoll *et al.* 1979, Mitchell *et al.* 1979). Some spots have lightning in them, as revealed in night side images (Little *et al.* 1999, Gierasch *et al.* 2000).

Spots form in a variety of ways (Mac Low and Ingersoll 1986). Some gather contrast slowly in an otherwise featureless region; some develop coherence and emerge from the turbulent flow; and others appear suddenly as bright points and grow by expansion. Likewise, some spots are absorbed by the turbulent flow; some are destroyed by mergers; and others simply fade away. "Life cycles" refers to appearances and disappearances, mutual interactions, and interactions with the zonal jets. Comparing the observed life cycles with those produced in numerical models (*e.g.*, Ingersoll and Cuong 1981,

Williams and Yamagata 1984, Marcus 1988, Dowling and Ingersoll 1989) leads to a better understanding of the dynamics of Jupiter's atmosphere.

Our study uses data spanning 70 days (October 1 to December 9, 2000) of observation by the Cassini Imaging Science System (ISS) in a filter centered at 751 nanometers. The only other comparable study (Mac Low and Ingersoll 1986) used 58 days of observation by the Voyager imaging system in the violet filter. In both cases the resolution of the raw images ranged from ~500 km/pixel at the beginning of the sequence to ~100 km/pixel at the end. Voyager imaged the disk of the planet every 1/5 of a jovian rotation and covered the entire planet once per jovian rotation, *i.e.,* once every 10 hours. The mosaics became a movie with time step ~10 hours and duration ~58 Earth days. Cassini operated in much the same way, except it often skipped a rotation so that the time step was sometimes 10 hours and sometimes 20 hours. Morales-Juberias *et al.* (2002), hereinafter MJ, studied spots using HST data over a 6-year period. The temporal sampling is less dense than ours, but we will compare our results with theirs wherever possible.

Each Cassini image was navigated by fitting (in the image plane) the observed planetary limb to its predicted location. Radiometric calibration was performed using the CISSCAL software developed by the Cassini ISS Team. The images for each rotation were projected into a simple cylindrical map spanning 360° of longitude. Illumination effects were removed by dividing by the cosine of the incidence angle, and regions shared by multiple images were averaged. The final maps were converted to 8-bit images using the same linear stretch for all maps and are stored without compression. To date, these steps

have been performed for the 751 nm filter only, although raw images spanning the same 70-day period exist for several other filters.

Each Cassini mosaic is 3600 x 1801 pixels and spans 360° of longitude and 180° of latitude. Therefore each pixel spans 0.1° of longitude and 0.1° of latitude. The scale of 0.1°/pixel, or ~125 km/pixel at the equator, was chosen such that all the 70-day images could be mapped consistently without loss of information. The spatial areas over which spots are measured include all 360° in longitude and 80°S to 80°N in latitude. The gases in Jupiter's troposphere are transparent in the 751-nm band, so these near-infrared continuum band images can capture a multitude of spots at different altitudes in the troposphere of Jupiter.

We use the term "spot" to describe a structure having the following four characteristics: (1) compact oval shape, (2) appearance in at least three successive images (life–history at least 40 hours), (3) a marked brightness difference from the surrounding clouds, and (4) diameter at least 700 km during some part of the spot's life. According to this definition, we record over 500 spots. We observe the sign of the vorticity for about 100 of the largest spots, whose rotation direction can be determined from a movie made from these images, and find that all these spots are anticyclonic (clockwise in the northern hemisphere, counterclockwise in the southern hemisphere). Among the 517 compact spots we record, 306 compact spots are bright and 211 compact spots are dark. The dark spots may be holes in the clouds or they may be dark cloud material that absorbs the light at 751 nm. Other studies (Banfield *et al,* 1998) suggest that bright and dark contrast originates at

~0.7 bar. We use planetographic latitudes, System III west longitudes, and positive zonal winds in the eastward direction. Mac Low and Ingersoll (1986) recorded over 100 spots in the Voyager mosaics. Their study focused on interactions between spots. Our study is larger (500 *vs.* 100 spots) and more general; it includes appearances, disappearances, distribution of lifetimes, size distribution, mutual interactions, interactions with the Great Red Spot (GRS), distribution with respect to latitude, and motion relative to the zonal jets.

We use the term chaotic region (CR) to define a patch of rapidly changing, amorphous features. CR's are distinct from compact spots, and are not included in our study except as they interact with spots. In many cases it is difficult to define the boundaries of a CR, and in some cases a CR is simply a cyclonic band circling the entire planet. Smith *et al.* (1979) called these patches "disturbed regions." Ingersoll *et al.* (1979) and Mitchell *et al.* (1979) used the term "turbulent, folded-filament regions." They also used the term "oblong cyclones," since the vorticity of the CR's is always cyclonic. These authors used the term "wakelike" to describe the CR's to the west of the large ovals. The largest wakelike region is the South Equatorial Belt (SEB) to the west and slightly equatorward of the Great Red Spot (GRS). Youssef and Marcus (2003) point out that a row of cyclonic CR's alternating with a row of anticyclonic ovals resembles a Karman vortex street. With a numerical model they show that the relative positions of the vortices are stable. In a classic vortex street the cyclones and anticyclones have the same size. On Jupiter the east-west dimension of the CR's is usually greater than that of the associated ovals.

1.3 Appearances and disappearances

Figure 1 shows that the number of appearances minus disappearances oscillates around zero. Over the whole period the numbers of appearances (393) and disappearances (356) are basically in balance, and their difference (393 – 356 = 37) is not statistically significant. The null hypothesis is that both appearances and disappearances in a 70-day period have a mean of 374.5 = (393+356)/2. The standard deviation of each is $374.5^{1/2}$ = 19.4. The standard deviation of their difference is $(2*374.5)^{1/2}$ = 27.4. The actual difference is 37, which is 1.35 standard deviations and not statistically significant.

Mac Low and Ingersoll (1986) observed 23 mergers, 23 other kinds of disappearances, and 19 appearances, roughly an order of magnitude fewer events than in our study. These authors noted that the number of spots destroyed was a factor of 2 greater than the number created during the 58-day observation period, and recommended further study of the budget. However, the main goal of their paper was to study the time-dependent behavior of interacting spots. The appearance of a spot is a solitary event. The fact that they observed less than one appearance per day whereas we observed more than four appearances per day suggests that Mac Low and Ingersoll did not record most of those events. In the long run, the appearance and disappearance of spots should be in balance.

We divide appearances into three types: (1) development of contrast in an otherwise featureless region, (2) development of a coherent structure in an otherwise turbulent

region, and (3) sudden appearance of a bright point followed by rapid expansion in size. Type 1 usually takes place outside the CR's, whereas Types 2 and 3 usually take place in the CR's. Type 2 often involves ejection of the spot from a CR. Type 3 describes the rapidly growing, easily identified features that often have lightning in them (Little *et al.*1999, Gierasch *et al.* 2000, Ingersoll *et al.* 2000). Porco *et al*. (2003) referred to these as "convective storms" in their analysis of the Cassini data. However neither Porco *et al.* (2003) nor we observed the lightning directly, so we will call them "probable convective storms." The resolution in our images ranges from 100 km to 500 km, which is enough to resolve the probable convective storms in the SEB (10°S-16°S) and the NEB (10°N-15°N). Compared with Porco *et al.* (2003) we did not find many convective storms at other latitudes, probably because we used just the 751 nm filter and they used other filters including those in the strong and weak methane bands. Convective storms are important for the jovian atmosphere because they can transport much of the heat flux from the deeper troposphere (Gierasch *et al.* 2000).

Figure 2a displays an example of a spot developing in a relatively calm area (Type 1). This is the most frequent kind of appearance among the three types (221 out of 393 cases). The gradual appearance of the spot in Fig. 2a is not due to the change in resolution, because in the first two sub-images we can see that the embryo did not have elliptical shape and we can see much smaller scale features than the embryo itself. Figure 2b shows a spot that emerged from the turbulence in a CR (Type 2). This is the next most frequent kind of appearance (141 out of 393). Figure 3a shows a very bright spot that

grows rapidly (Type 3), and is probably a convective storm. This is the least frequent kind of appearance (31 out of 393 cases).

We also divide disappearances into three types: (1) disappearance due to merging, (2) destruction by the turbulence, usually in a CR, and (3) gradual fading. Figure 3b shows a merger between two spots. This type of disappearance is different from destruction by turbulence (Fig. 4a) because it results in a recognizable spot. Absorption by turbulence results in more turbulence □amorphous, rapidly changing patterns that have no definite spots. Mac Low and Ingersoll (1986) were especially interested in mergers because the solitary wave model (Maxworthy *et al.* 1978) predicted that when one spot overtakes another at the same latitude they would pass through each other, whereas other models (Ingersoll and Cuong 1981, Williams and Yamagata 1984) predicted that the two spots would merge. We record 119 mergers and 7 near misses □where spots passed around each other □out of the total 126 interactions during the 70-day period. Our result seems to support these merging models.

Figure 4a shows a small spot that is destroyed by turbulence inside a CR. This kind of disappearance accounts for more than one-fourth of the total number of disappearances (90 out of 356). CR's are not only an important source of spots but also an important sink of spots. Figure 4b shows a spot that fades away. It disappears without undergoing any interaction with other spots or CR's. The number of this kind of disappearance is largest among the three types of disappearance (147 out of 356 cases).

1.4 Dimensions

In Fig. 5 we record the sizes of all spots and give a scatter plot of north-south (NS) and east-west (EW) diameters based on the brightness and lifetime. In our study, long-lived spots are those that existed throughout the entire 70-day period, and short-lived spots are those that both appeared and disappeared during the 70-day period. The GRS and white oval at -33° are not included in the list of long-lived spots. Figure 5 offers two different linear fits between the two diameters by assuming that the uncertainties of measurement in major and minor diameters are the same (Meyer 1986). The fitting lines from the origin indicate that long-lived spots and dark spots have smaller NS/EW ratios than short-lived spots and bright spots. The two-parameter fit presents a different result because it is more sensitive to spots having extreme low and high ratios than the fit from the origin.

Figure 5 shows that all the long-lived spots have major diameters greater than ~2000 km. The short-lived spots have major diameters ranging from below 1000 km to over 6000 km. There is no correlation between lifetime and size for the short-lived spots, and we cannot measure the lifetimes of the long-lived spots. Our results are generally in agreement with Figs. 4 and 6 of MJ, although our study has a smaller minimum spot size (700 km *vs*. 1500 km) and a shorter time base than theirs.

1.5 Distribution of lifetimes

The time between the appearance and disappearance of a spot is its lifetime. Figure 6 is a histogram of lifetimes, constructed using those spots having a complete life history during Cassini's 70-day observation window. The histogram has a bias, which is correctable: A spot with lifetime $t < 70$ days must appear in the initial $(70-t)$ days of the observation window to be included in the histogram. Spots with lifetimes $t > 70$ days are not included in the histogram. Thus if n_A is the average number of spots that appear during a 70 day window and $p(t)\,dt$ is the fraction whose lifetimes are in the range $(t, t+dt)$, then $(70-t)/70\ n_A\ p(t)\,dt$ is the number in this lifetime range that appear and disappear in the window. This is the histogram displayed in Fig. 6.

In Fig. 6, the fitted curves show $(70-t)/70\ n_A\ p(t)\,dt$, where dt = 1 day and $p(t) = (1/\tau)\exp(-t/\tau)$. For the value of n_A we average the number of appearances and the number of disappearances, since the two are the same except for statistical fluctuations. This gives n_A =29.5 for the upper panel and n_A = 345 for the lower panel. The one adjustable parameter is τ, and the fitting yields τ = 3.5 days for the probable convective storms and τ = 16.8 days for all other spots. We separated the latter (other spots) into a bright group and a dark group, and fit the distribution of lifetimes for the two groups separately (not shown). The fitting shows that the time constant of bright spots having a complete life history (τ =14 days) is smaller than the time constant of dark spots having a complete life history (τ =21 days).

The expectation value for the total number of spots that appear and disappear in the window is

$$n_{AD} = n_A \int_0^{70} (70 - t)/70 \; p(t)\, dt .$$

The expected number n_{AO} of spots that only appear in the window and disappear later is $n_A - n_{AD}$. The expected number n_{DO} of spots that only disappear in the window and appear earlier is also $n_A - n_{AD}$. Actual numbers will be different because of statistical fluctuations.

Information about lifetime $t > 70$ days is contained in the number n_{LL} of long-lived spots that existed throughout the observation period. To be included in this number, a spot with lifetime t must appear no more than $(t\text{-}70)$ days before the start of the Cassini observation window. Thus if $n_A\, p(t)\, dt$ is the average number of spots appearing in a 70 day window with lifetimes in the range $(t,\ t+dt)$, then $(t\text{-}70)/70\ n_A\, p(t)\, dt$ is the number that exist throughout the observation period. The integral is the expectation value of n_{LL}:

$$n_{LL} = n_A \int_{70}^{\infty} (t - 70)/70 \; p(t)\, dt$$

In Table I we compare the observed and expected values of n_{LL}, n_{AO}, n_{DO}, and n_{AD} for probable convective storms and for all other spots. The expected values use the best fit to the histogram in Fig. 6, with $\tau = 3.5$ days for the probable convective storms and $\tau = 16.8$ days for all other spots. The number of appearances is $n_{AO} + n_{AD}$, and the number of

disappearances is $n_{DO} + n_{AD}$. Except for n_{LL}, the differences between the observed and expected numbers are consistent with statistical fluctuations. However, the expected number of non-convective (other) spots that survive for the entire 70-day period is 1, whereas the observed number is 35. Evidently there are more spots with long lifetimes than the exponential distribution would suggest. There is even some evidence that the spots with lifetimes longer than 70 days are from a different population: As shown below, the long-lived spots have different distributions with respect to latitude and size than the spots that appear and disappear in the Cassini observation window.

1.6 Relation to zonal winds

Much work on zonal winds of Jupiter has been done based on the data sets of Voyager, Galileo, and HST (Ingersoll *et al.* 1981, Limaye 1986, Vasavada *et al*. 1998, Garcia-Melendo and Sanchez-Lavega 2001). These studies support the idea that the zonal wind profile at the cloud level has remained basically unaltered in spite of some minor variations in jet shape and speed. This implies that the global circulation of Jupiter is stable even though there are turbulence and convection in the atmosphere.

Feature tracking and correlation are two methods for measuring the wind velocity on Jupiter. By manually following the target clouds in images taken at different times, the feature tracking method can determine the wind speed at the latitudes where these target clouds sit, if clouds can be regarded as passive tracers of atmospheric mass motion. For this method, the change of feature shape, the interaction between these clouds and their

environment, and operator judgment will cause some errors. On the other hand, the correlation method takes a narrow latitude band spanning 360° in longitude as the target and determines its mean east-west movement by finding the largest correlation coefficient between two images taken at different times. Systematic errors caused by changes of the clouds, wave-like phenomena, and large vortices (GRS, for example) will affect the correlation method (Garcia-Melendo and Sanchez-Lavega 2001). Both methods are sensitive to spots, but the correlation method is also sensitive to amorphous features and large-scale structures that a human operator might ignore.

In our study, we record the position of each spot every 60 hours and compute a velocity based on its displacement over this 60-hour time interval. If the spot changes latitude by less than 1°, and if it changes velocity from the average value for its complete life history by less than 10 m s^{-1}, then we will use the spot as a record for the wind velocity of the latitude in which it sits. In addition, for these latitudes in which there are few spots we use other features having stable non-oval shape as tracking targets to get the wind velocity for these latitudes. Then we average these records in different 1° bins to get the wind velocity for latitudes from 78°S to 83°N. This was impossible for some latitudes (77°N, 25°N, 21°N, 16°N, 10°N, 2°N-5°N, 1°S, 14°S, 26°S, 30°S, 37°S, 44°S, 54°S, 61°S, 63°S, 67°S-70°S and 77°S) where we could not find good tracking targets. We use interpolation to get the values of wind velocity at these latitudes.

Figure 7 shows that the wind profile obtained from Cassini by the feature tracking method is in good agreement with the wind profile obtained by the correlation method

(Porco *et al.* 2003). The correlation coefficient between the two profiles from 78°S to 83°N is 0.9257. Porco *et al* (2003) study changes in the jets from the Voyager time to the Cassini time. Further study of the changes of wind profiles requires a detailed discussion of the accuracy of data from different sources (Voyager, HST and Cassini) and an error analysis of velocity measurement in all these studies. Such an effort is beyond the scope of this study.

Using the data of Voyager, Ingersoll *et al* (1979, 1981) and Limaye (1986) discussed the curvature of the westward jets and the jets' stability according to the barotropic stability criterion. In this paper, we repeat this work based on more data including Voyager, HST and Cassini. The Voyager data (Limaye, 1986) were taken in 1979. The HST data (Garcia-Melendo and Sanchez-Lavega 2001) were taken from 1995 to 2000. The Cassini data were taken in 2000.

The barotropic stability criterion says that a two-dimensional (barotropic) flow is stable when $\beta - \overline{u}_{yy} > 0$ at all latitudes. Here $\beta = df/dy = 2\Omega\cos\phi/R_J$ is the planetary vorticity gradient, $f = 2\Omega\sin\phi$ is the Coriolis parameter, ϕ is planetographic latitude, Ω and R_J are Jupiter's angular rate of rotation and planetary radius, respectively; $\overline{u}$ is the mean zonal wind, y is the northward coordinate, and $\overline{u}_{yy}$ is the curvature of the jets. Since β is positive everywhere and $\overline{u}_{yy}$ is positive at the latitudes of the westward jets, the criterion is most likely to be violated at these latitudes. Vertical structure in the flow can alter its stability, but it is uncertain and we do not discuss it here.

Figure 8 shows parabolas with curvature β that are centered on the westward jets. The figure shows that some jets developed more curvature than β and others developed less curvature than β during the 21 years 1979-2000. The jet at 39°N had $\overline{u}_{yy} > \beta$ during HST time and less at other times. The jet at 31°N had $\overline{u}_{yy} > \beta$ during Voyager time and less at other times. The jet at 17°N had $\overline{u}_{yy} > \beta$ during Voyager times and less at other times. The jet at 20°S had $\overline{u}_{yy} > \beta$ during HST and Cassini times and less during Voyager times. The jet at 32°S had $\overline{u}_{yy} > \beta$ during Voyager time and less at other times. The general agreement between HST and Cassini and between the feature tracking and correlation methods suggests that the differences relative to β are significant. In general, the number of westward jets that clearly violate the barotropic stability criterion is about the same during Cassini time as during Voyager and HST times.

The left panel of Fig. 9 shows that in the northern hemisphere the spots are concentrated at the latitudes of the westward jets. The appearances and disappearances (not shown) of these compact spots have almost the same latitude distributions as the spots themselves. Since the westward jets are most likely to violate the barotropic stability criterion, they are most likely to develop waves and eddies, which could coalesce into spots (*e.g.*, Dowling and Ingersoll 1989). This may explain the distribution of spots in the northern hemisphere. However in the southern hemisphere there is not a good correlation between the latitude distribution of spots and zonal winds. Obviously, the barotropic stability criterion cannot explain the difference between the northern and southern hemispheres.

Perhaps the GRS and the large White Oval Spot centered at –33° affect the distribution of spots in the southern hemisphere due to their large size.

The right panel of Fig. 9 shows that long-lived spots are concentrated at middle latitudes, mainly in anticyclonic bands. Their distribution is significantly different from that of all spots, which on average are concentrated in the westward jets (left panel of Fig. 9). Since the long-lived spots are anticyclonic, this observation is consistent with numerical models, which show that vortices of one sign are stable when they are imbedded in a region whose vorticity has the same sign (Ingersoll and Cuong 1981, Williams and Yamagata 1984, Marcus 1988, Dowling and Ingersoll 1989).

MJ found differences between the vortex speed and the mean zonal velocity at the central latitude of each vortex (see their Fig. 8). They found that the difference is anti-correlated with the mean zonal velocity. Figure 10 is the same as MJ Fig. 9, and shows the relative velocity (difference between the zonal velocity of the spot and that of the mean flow) vs. the mean zonal velocity at the center of the spot. There is no obvious anti-correlation (negative slope) between the two variables, except possibly for the long-lived spots (bottom half) if one ignores the three points farthest to the right. The absolute value of the slope of the remaining points is less than that of the line in MJ Fig. 9. Our data in Fig. 10 are not too different from those in MJ Fig. 9, considering that their time base is much longer than ours and we have more data for short-lived spots (top half of Fig. 10).

1.7 Interaction with the GRS

As the largest anticyclone of the jovian atmosphere, the GRS has existed for at least 100 years and probably for over 300 years (Rogers 1995). Smith *et al.* (1979) and Mac Low and Ingersoll (1986) recorded that the GRS absorbed smaller anticyclones, which suggests that the GRS maintains itself in this way (Ingersoll and Cuong 1981, Ingersoll *et al*. 2000). Their conclusion is derived from Voyager observations, when the SEB was in one of its disturbed phases (labeled SEBD1 by Sanchez-Lavega and Gomez 1996). During the Cassini encounter, from which our study was taken, the SEB was also in a disturbed phase. Our conclusions may not apply when the SEB is in its faded phase, as it was during the Pioneer 10 encounter in 1973.

During the 70-day period, we find nine large spots (major diameter greater than 2000 km) that were absorbed by the GRS from the east. These large spots are shown in Fig.11. Further information about them is given in Table II. In those cases where we could determine the vorticity (7 out of 9 cases), it was anticyclonic. In addition to these large spots, small dark spots were absorbed by the GRS from the west. Because these spots are small and because we could not determine their vorticity, we have not included them in this discussion.

The large spots absorbed by the GRS probably originate from the CR's in the SEB west of the GRS. They are entrained into the westward jet to the south of the SEB and encounter the GRS from the east. Figure 12 shows a time history of spots coming from

the chaotic regions in the SEB west of the GRS. Lightning observations (Gierasch *et al.* 2000) show that moist convection associated with convective storms is very active in the SEB west of the GRS. The last four sub-images contain a probable convective storm that appears in Fig. 3 of Porco *et al.* (2003). Figure 12 also shows two other probable convective storms (white arrows) appearing in the same chaotic regions in the SEB. The fact that the westward-moving spots that are absorbed by the GRS originate in the same chaotic region as the probable convective storms suggests that development of westward-moving spots is related to the latent energy released by these storms. Some uncertainty remains, however, because there is no one-to-one correspondence between the compact spots and the convective storms (Fig. 12). They both originate in the same region, but they do not appear to be the same features.

Nevertheless, these observations support the idea that the chaotic regions in the SEB, probable convective storms, and the westward jet compose a system that supports the GRS (Gierasch *et al.* 2000, Ingersoll *et al.* 2000). In this system, convective storms in the SEB get energy from the interior of Jupiter by moist convection and deliver energy to the compact spots that will be absorbed by the GRS.

1.8 Conclusions

In this study, we record properties of over 500 spots during a 70-day period from the continuum band ISS images of Cassini. The relation between the spots and mean zonal wind profile and interactions between spots and the GRS are also discussed.

The appearance and disappearance of compact vortices maintained a balance during the period, and the CR's are an important source and sink for compact vortices. The major diameter of long-lived spots is greater than 2000 km.

Exponential functions provide a good fit to the distribution of lifetimes, with time constants of 3.5 days for probable convective storms and 16.8 days for all other spots.

Our wind profile from feature tracking is in good agreement with the one from the correlation method. The wind profile shows that the number of westward jets violating the barotropic stability criterion is about the same during Cassini time as during Voyager and HST times. The barotropic stability criterion can explain the observation that spots are concentrated at the latitudes of westward jets in the northern hemisphere, but the theory cannot explain why there is no such concentration in the southern hemisphere. The fact that long-lived spots are concentrated in anticyclonic bands is consistent with numerical models.

Spots that originate in the chaotic regions in the SEB are absorbed by the GRS. This and other observations suggest that the chaotic regions in the SEB, moist convection, the westward jet, and spots in the SEB latitudes compose a system supporting the GRS.

1.9 References

Banfield, D., P. J. Gierasch, M. Bell, E. Ustinov, A. P. Ingersoll, A. Vasavada, and M. J. S. Belton 1998. Jupiter's cloud structure from Galileo imaging data. *Icarus* **135,** 230-250.

Dowling, T. E., and A. P. Ingersoll 1989. Jupiter's Great Red Spot as a shallow water system. *J. Atmos. Sci.* **46,** 3256-3278.

Garcia-Melendo, E., and A. Sanchez-Lavega 2001. A study of the stability of jovian zonal winds from HST images: 1995-2000. *Icarus* **152,** 316-330.

Gierasch, P. J., A. P. Ingersoll, D. Banfield, S. P. Ewald, P. Helfenstein, A. Simon-Miller, A. Vasavada, H. H. Breneman, and D. A. Senske 2000. Observation of moist convection in Jupiter's atmosphere. *Nature* **403,** 628-630.

Ingersoll, A. P., R. F. Beebe, S. A. Collins, G. E. Hunt, J. L. Mitchell, J. P. Muller, B. A. Smith, and R. J. Terrile 1979. Zonal velocity and texture in the Jovian atmosphere inferred from Voyager images. *Nature* **280,** 773-775.

Ingersoll, A. P., R. F. Beebe, J. L. Mitchell, G. W. Garneau, G. M. Yagi, and J. P. Muller 1981. Interaction of eddies and mean zonal flow on Jupiter as inferred from Voyager 1 and Voyager 2 Images. *J. Geophys. Res.* **86,** 8733-8743.

Ingersoll, A. P., and P.-G. Cuong 1981. Numerical model of long-lived jovian vortices. *J. Atmos. Sci.* **38,** 2067-2074.

Ingersoll, A. P., P. J. Gierasch, D. Banfield, and A. R. Vasavada 2000. Moist convection as an energy source for the large-scale motions in Jupiter's atmosphere. *Nature* **403,** 630-632.

Limaye, S. S. 1986. New estimates of the mean zonal flow at the cloud level. *Icarus* **65,** 335-352.

Little B., C. D. Anger, A. P. Ingersoll, A. R. Vasavada, D. A. Senske, H. H. Breneman, and W. J. Borucki 1999. Galileo images of lightning on Jupiter. *Icarus* **142**, 306-323.

Mac Low, M.-M., and A. P. Ingersoll 1986. Merging of vortices in the atmosphere of Jupiter: An analysis of Voyager images. *Icarus* **65,** 353-369.

Marcus, P. S. 1988. Numerical simulation of Jupiter's Great Red Spot. *Nature* **331,** 693-696.

Maxworthy. T., L. G. Redekopp, and P. D. Weidman 1978. On the production and interaction of planetary solitary waves: Application to the Jovian atmosphere. *Icarus* **33,** 388-409.

Meyer, S. L. 1986. *Data Analysis for Scientists and Engineers,* pp.74-75. Peer Management Consultants, Ltd., Evanston.

Mitchell, J. L., R. J. Terrile, B. A. Smith, J. P. Müller, A. P. Ingersoll, G. E. Hunt, S. A. Collins, and R. F. Beebe 1979. Jovian cloud structure and velocity fields. *Nature* **280,** 776-778.

Morales-Juberias, R., A. Sanchez-Lavega, J. Lecacheux, and F. Colas 2002. A comparative study of jovian anticyclone properties from a six-year (1994-2000) survey. *Icarus* **157**, 76-90.

Porco, C. C, R. A. West, A. McEwen, A. D. Del Genio, A. P. Ingersoll, P. Thomas, S. Squyres, L. Dones, C. D. Murray, T. V. Johnson, J. A. Burns, A. Brahic, G. Neukum, J. Veverka, J. M. Barbara, T. Denk, M. Evans, J. J. Ferrier, P. Geissler, P. Helfenstein, T. Roatsch, H. Throop, M. Tiscareno, and A. R. Vasavada 2003. Cassini imaging of Jupiter's atmosphere, satellites, and rings. *Science* **299,** 1541-1547.

Rogers, J. H. 1995. *The Giant Planet Jupiter*. Cambridge University Press, Cambridge, UK.

Sanchez-Lavega, A., and J. M. Gomez 1996. The South Equatorial Belt of Jupiter, I: Its life cycle. *Icarus* **121**, 1-17.

Smith, B.A., L.A. Soderblom, T.V. Johnson, A.P. Ingersoll, S.A. Collins, E.M. Shoemaker, G.E. Hunt, H. Masursky, M.H. Carr, M.E. Davies, A.F. Cook, II, J. Boyce, G.E. Danielson, T. Owen, C. Sagan, R.F. Beebe, J. Veverka, R.G. Strom, J.F. McCauley, D. Morrison, G.A. Briggs, and V.E. Suomi 1979. The Jupiter system through the eyes of Voyager 1. *Science* **204**, 951-972.

Vasavada, A. R., A. P. Ingersoll, D. Banfield, M. Bell, P. J. Gierasch, M. J. S. Belton, G. S. Orton, K. P. Klaasen, E. De Jong, H. H. Breneman, T. J. Jones, J. M. Kaufman, K. P. Magee and D. A. Senske 1998. Galileo imaging of Jupiter's atmosphere: The Great Red Spot, equatorial region, and White Ovals. *Icarus* **135,** 265-275.

Williams, G. P., and T. Yamagata 1984. Geostrophic regimes, intermediate solitary vortices and Jovian eddies. *J. Atmos. Sci.* **41,** 453-478.

Youssef, A., and P. S. Marcus 2003. The dynamics of jovian white ovals from formation to merger. *Icarus* **162**, 74-93.

Table 1.1 Number of Appearances and Disappearances

		n_{LL}	n_{AO}	n_{DO}	n_{AD}
probable convective storms	(expected)	0	2	2	27
probable convective storms	(observed)	0	3	0	28
all other compact spots	(expected)	1	82	82	263
all other compact spots	(observed)	35	123	89	239

n_{LL} = long-lived spots, lifetime > 70-days

n_{AO} = appear only, disappear later

n_{DO} = disappear only, appeared earlier

n_{AD} = appear and disappear in the 70-day period.

Table 1.2 Nine Spots Absorbed by the GRS

number	time of absorbing	long diameter	short diameter	vorticity
1	Oct 14 00:57	3513 km	1466 km	anticyclone
2	Oct 18 14:37	5387 km	2053 km	anticyclone
3	Nov 08 17:33	6675 km	2443 km	unknown
4	Nov 12 14:37	5738 km	2443 km	anticyclone
5	Nov 17 01:10	3513 km	1662 km	anticyclone
6	Nov 17 21:02	2576 km	1173 km	anticyclone
7	Nov 28 16:19	2928 km	1759 km	unknown
8	Dec 02 20:02	3748 km	1759 km	anticyclone
9	Dec 09 11:42	5270 km	2150 km	anticyclone

Figure 1.1 The numbers of appearances and disappearances of spots every 60 hours during the 70-day period. The figure also shows the value of appearance minus disappearance during the period.

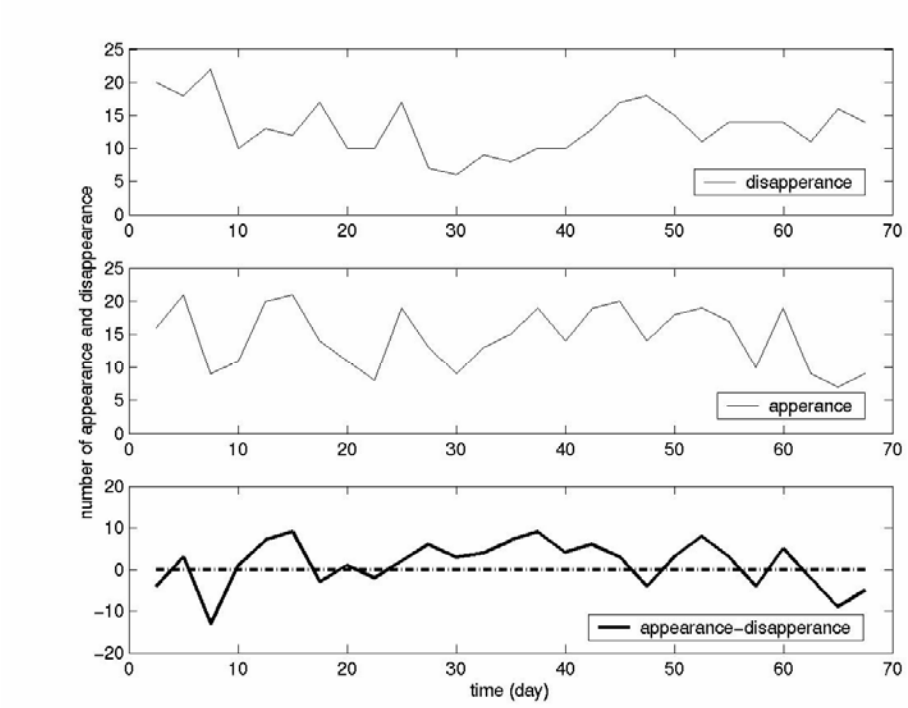

Figure 1.2 (a) Large spot developing slowly outside of a CR. In this figure and all other figures like it (Figs. 2b, 3a, 3b, 4a, and 4b), time increases from top to bottom. Note that the time step between neighboring sub-images of Fig. 2a is 10 days, so the spot is developing very slowly. The time step for all other such figures (Figs. 2b, 3a, 3b, 4a, and 4b) is 20 hours. The range for every frame of Fig. 2a is (12°N-23°N, 350°-17°). The time of the first sub-image (the top one) is Oct 5, 2000. The large spot covers the center of the 17°N westward jet. (b) Spot coming from a CR. The range for every frame is (42°N-54°N, 230°-267°). The time of the first sub-image is Nov 5, 2000. The spot sits in an anti-cyclonic band.

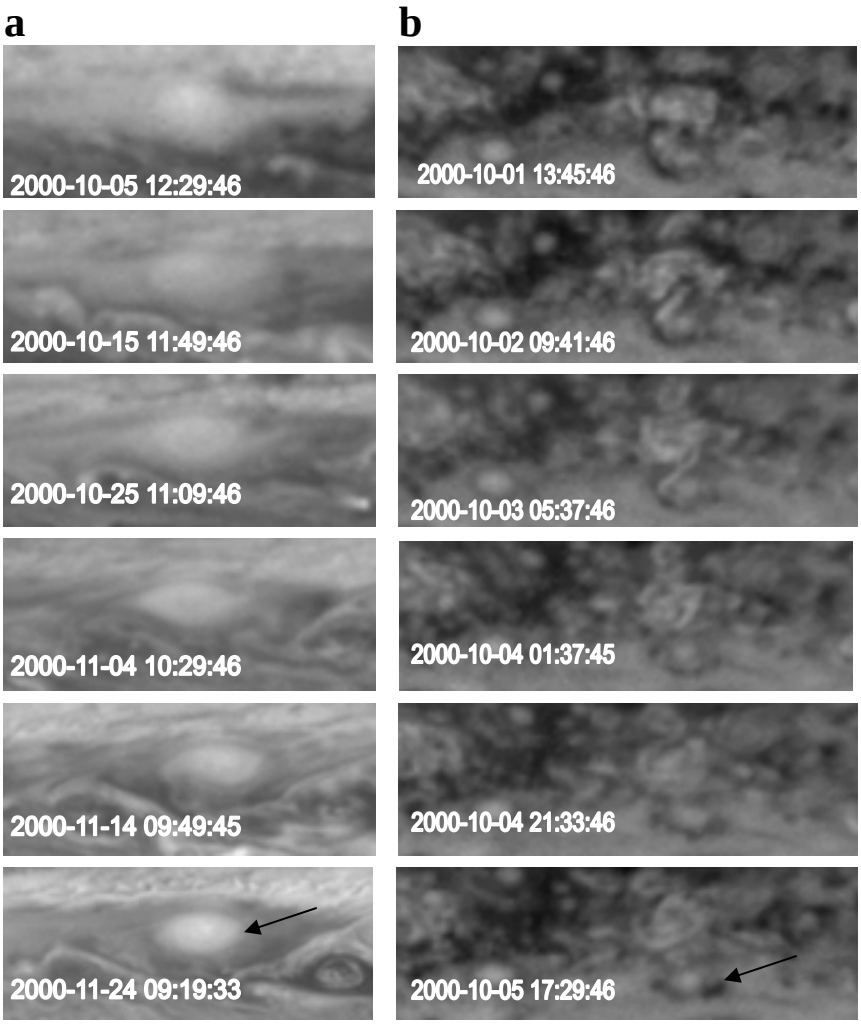

Figure 1.3 (a) A fast-developing spot in a CR, probably a convective storm. The range for every frame is (9°N-17°N, 8°-30°). The time of the first sub-image is Oct 29, 2000. The spot sits in a cyclonic band. (b) Two spots merging with each other. The range for every frame is (38°N-45°N, 280°-295°). The time of the first sub-image is Nov 13, 2000. The two spots sit in an anti-cyclonic band.

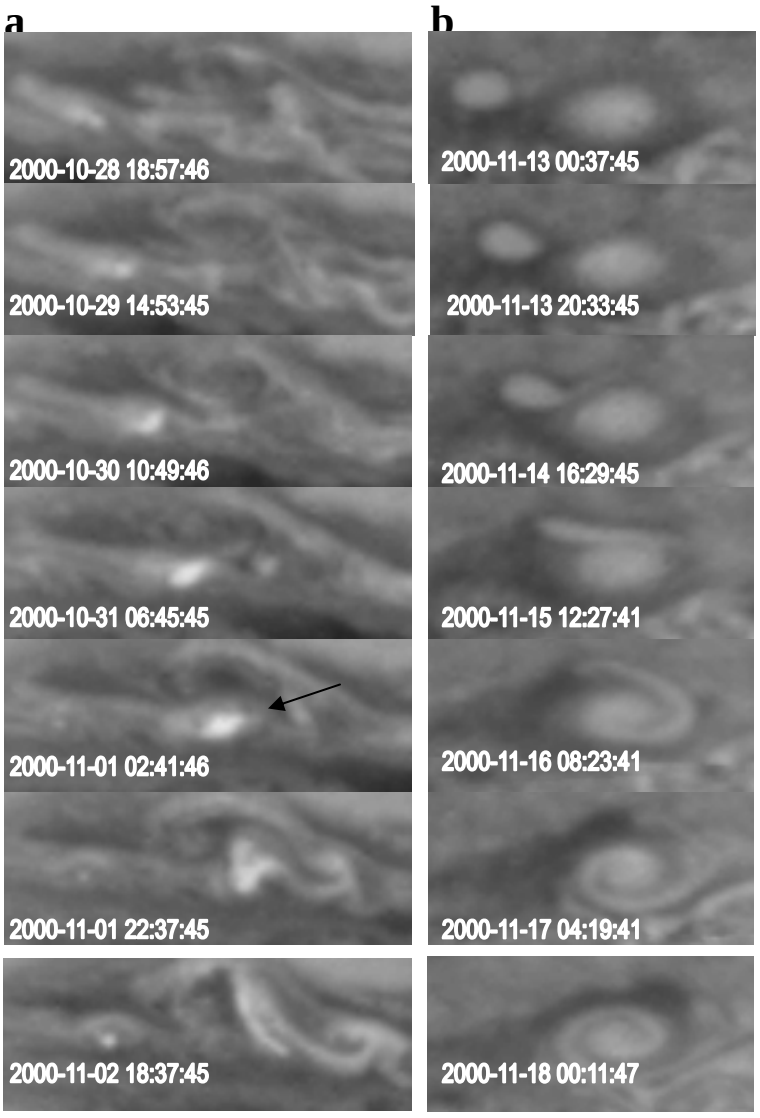

Figure 1.4 (a) A small spot destroyed by a CR. The range for every frame is (46°N-57°N, 90°-117°). The time of the first sub-image is Nov 25, 2000. The spot sits in an anticyclonic band and meets the left side of a turbulent structure in the CR. (b) A spot that lost contrast and faded away. Sometimes this case resembles that in Fig. 4a, absorption by turbulence. The range for every frame is (42°N-48°N, 310°-324°). The time of the first sub-image is Nov 18, 2000. The spot covers the center of the 45°N eastward jet.

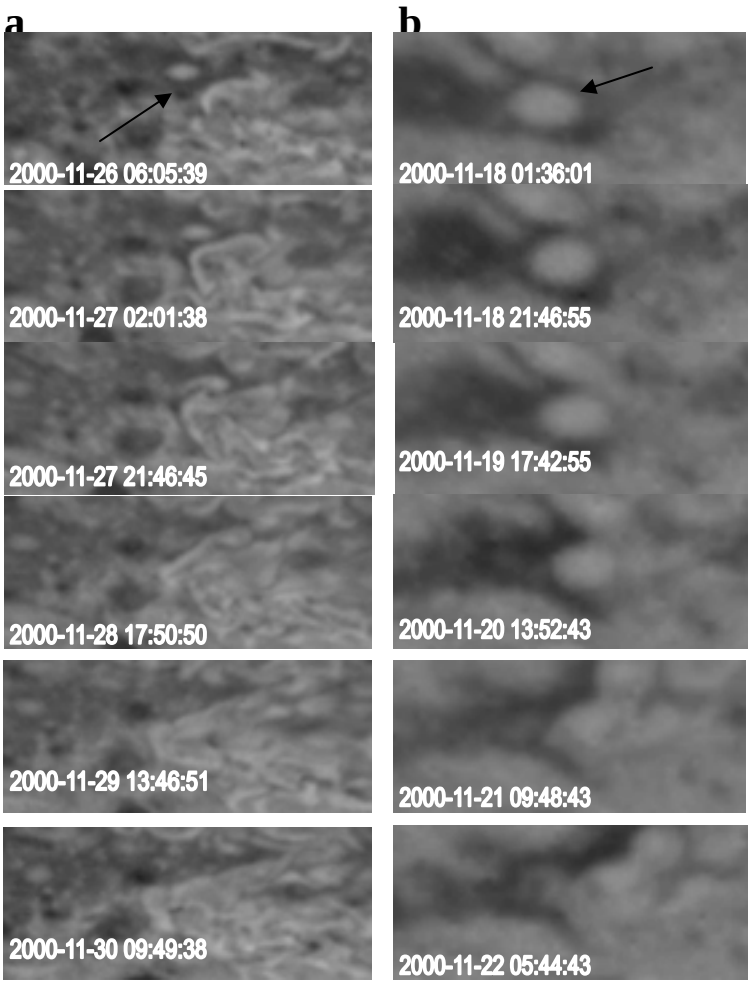

Figure 1.5 Scatter plot of the major and minor diameters of spots. The left-top panel is for bright short-lived spots, and the left-bottom panel is for dark short-lived spots. The right-top panel is for bright long-lived spots, and the right-bottom is for dark long-lived spots. Solid lines are one-parameter (slope) linear fitting from origin, and the dashed lines are two-parameter (slope and intercept) linear fitting.

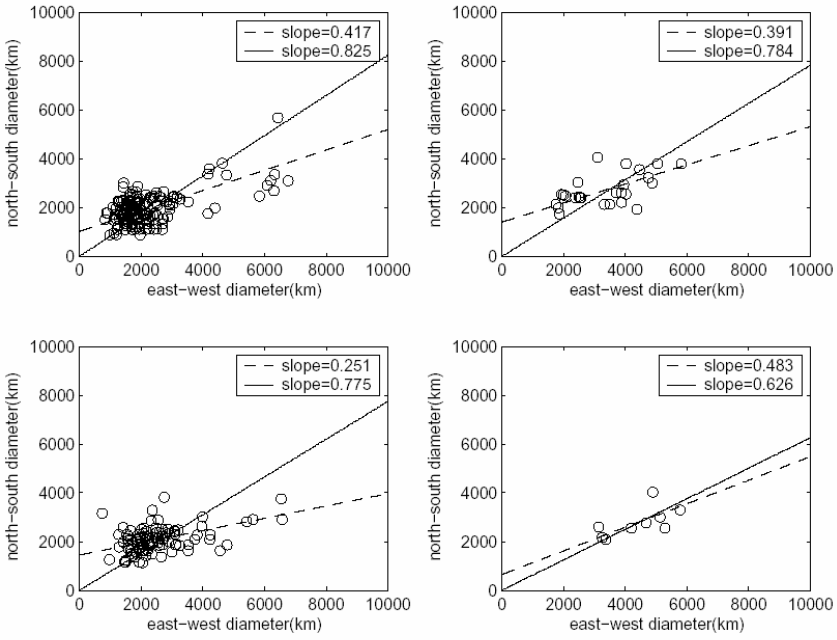

Figure 1.6 The distribution of lifetimes of spots having complete life cycles during the 70-day period. Each point represents the average number of spots in a lifetime bin 1 day wide. The upper panel is for probable convective storms and the bottom panel is for all other spots.

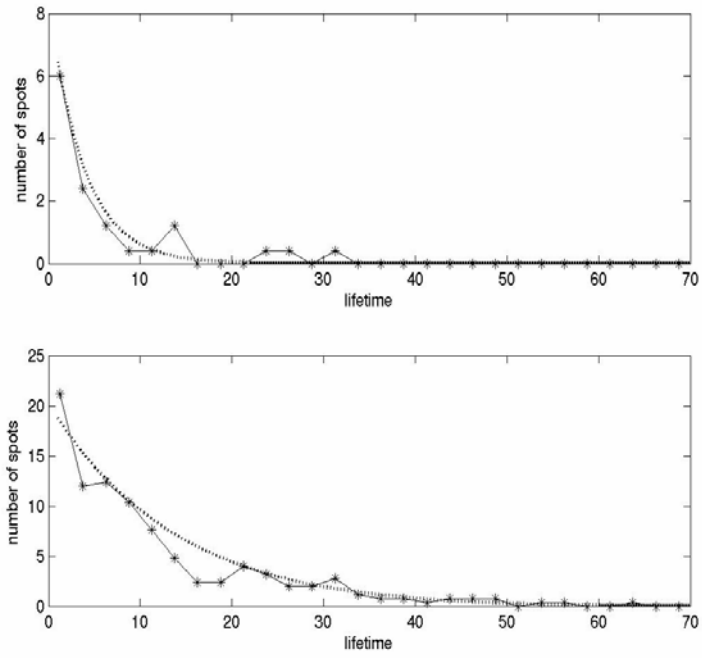

Figure 1.7 The zonal wind profile obtained from Cassini by two different methods — feature tracking and correlation. Both wind profiles use planetographic latitudes. In the left panel, each point is a single feature, and the solid line is the average of the points in a 1° bin. In the right panel, the two lines are from feature tracking in this study and correlation method from Porco *et al.* (2003).

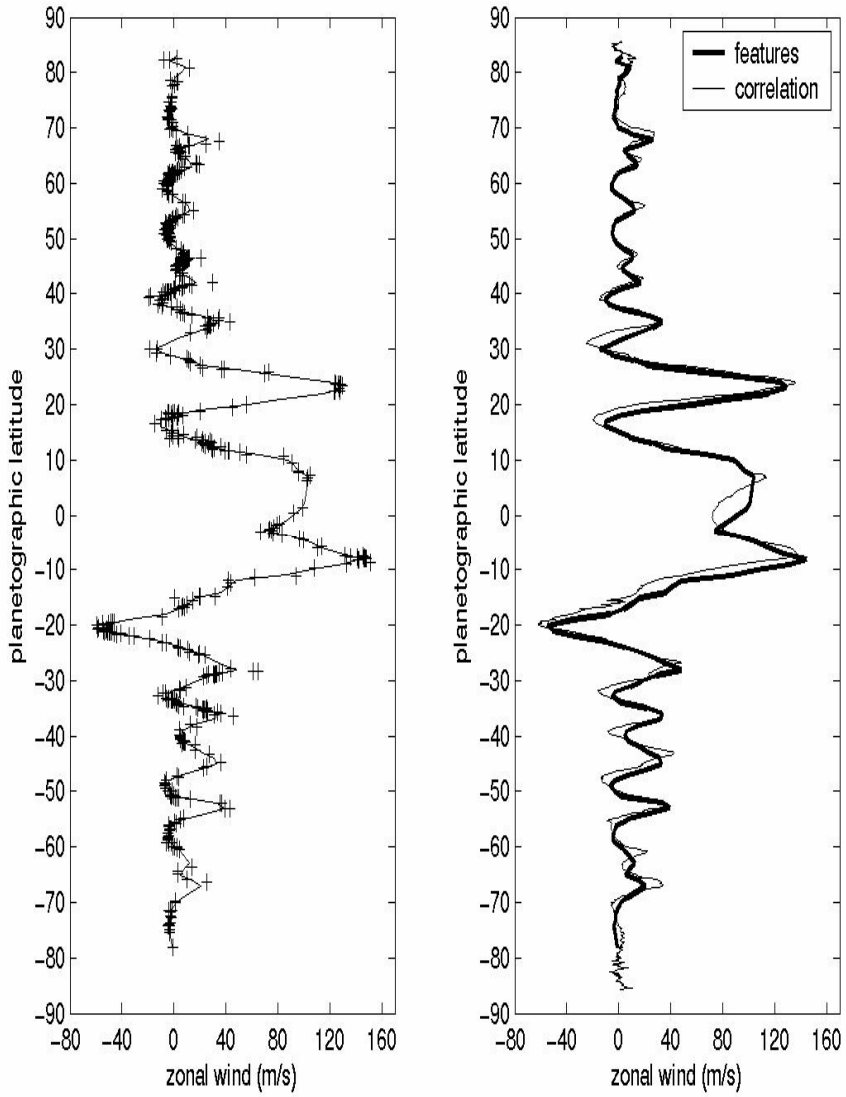

Figure 1.8 Curvature $d^2\overline{u}/dy^2$ of the zonal velocity profile compared to β. From left to right the data are from Voyager(1979), HST(1995-2000), Cassini (2000) feature tracking, and Cassini correlation. The parabolic curves are defined by $d^2\overline{u}/dy^2 = \beta$, and are centered on the westward jet maxima. For the Cassini feature tracking profile, each point is an average of features in a 1° latitude bin. For the other profiles the resolution is 2-3 times better. Where the measured profile lies inside the parabola, the flow violates the barotropic stability criterion.

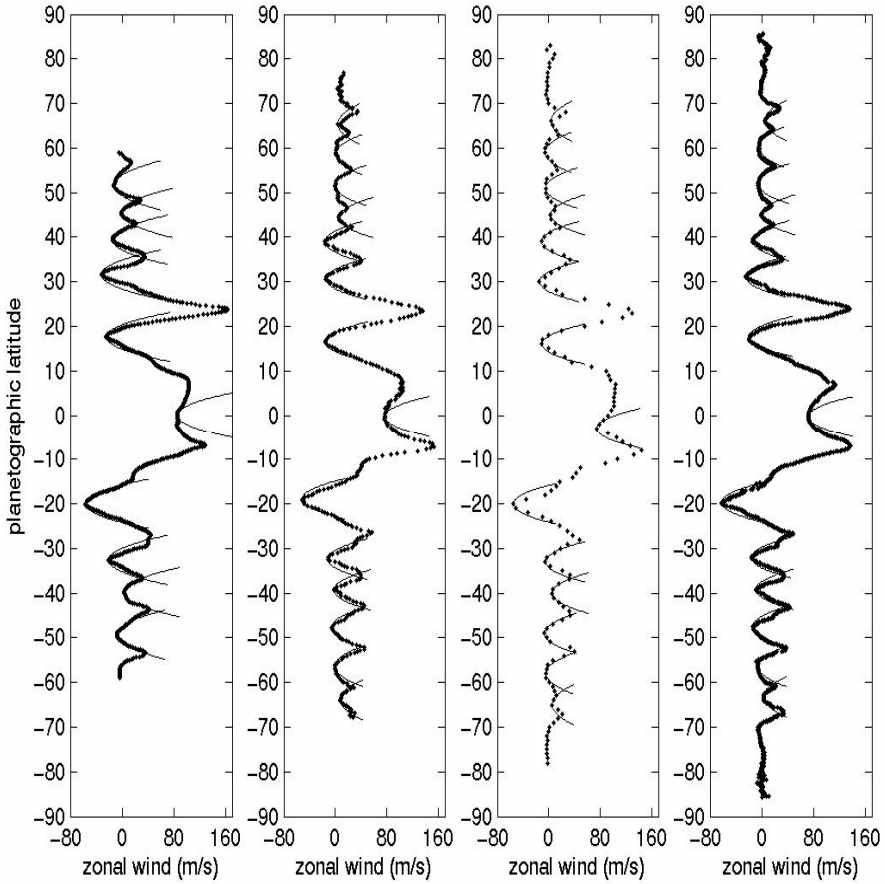

Figure 1.9 Comparison between the latitude distribution of spots and the zonal wind profile. The left panel gives the number of all spots per degree of latitude with a scaling factor 4 (light line) along with the zonal wind profile determined by the feature tracking method (heavy line). The right panel is same as the left panel except for long-lived spots and scaling factor 20.

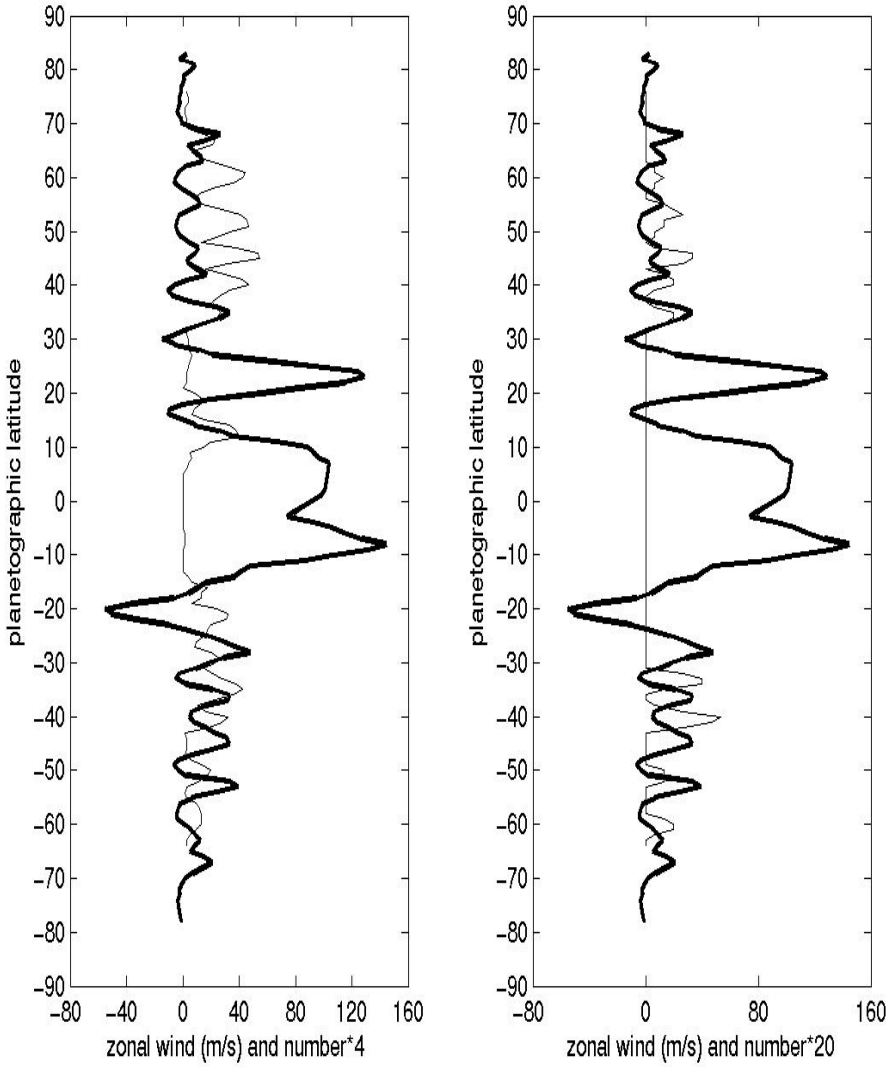

Figure 1.10 Relative velocity (difference between the zonal velocity of the spot and that of the mean flow) vs. mean zonal velocity. The mean zonal velocity is from Cassini (Porco *et al.*, 2002). The top panel is for all spots, and the bottom panel is for long-lived spots. Each dot represents a spot. Compare with Fig. 9 of MJ.

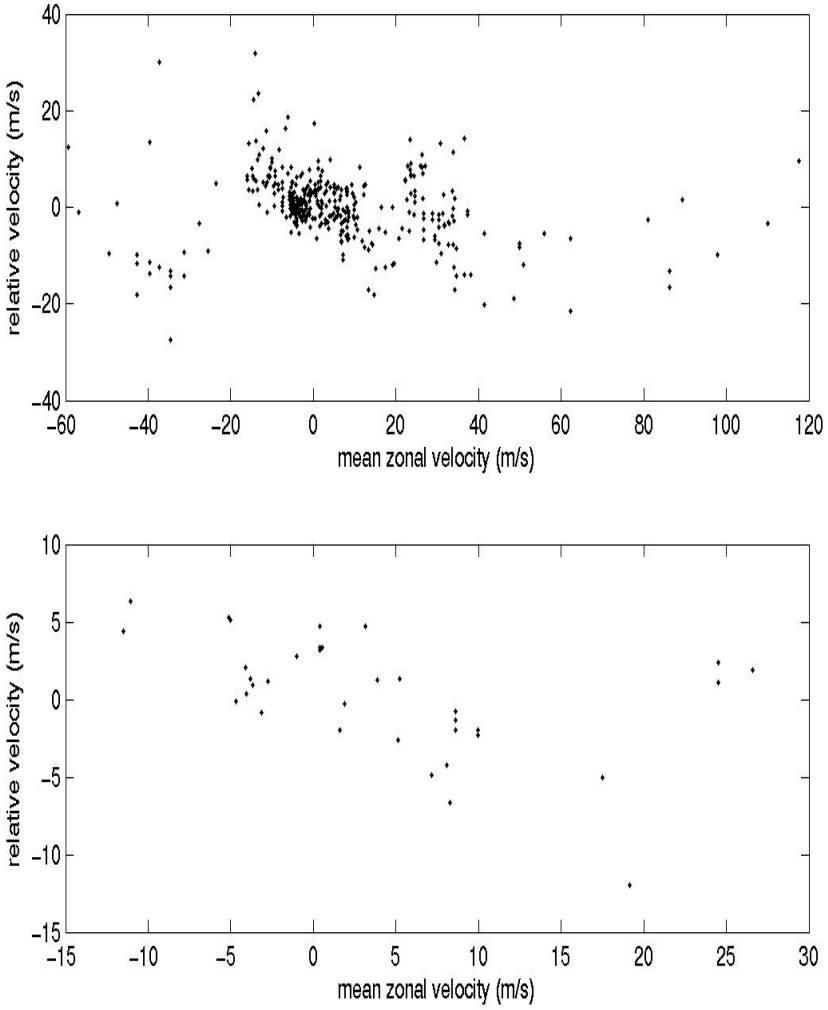

Figure 1.11 Nine large spots absorbed by the GRS during the 70-day period. The range for every frame is (10°S-28°S, 130°-185°). This figure is not a time sequence like Figs. 2-4. Every sub-image in this figure records a different large spot that will be absorbed by the GRS from the east at a different time.

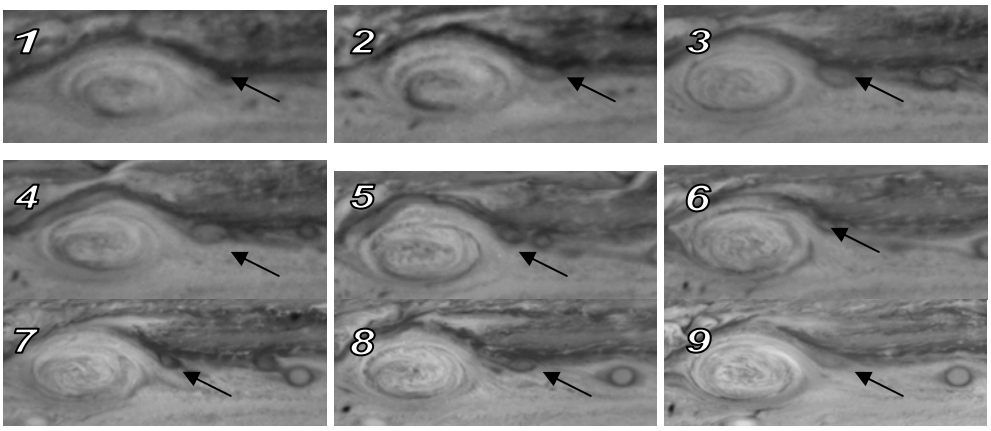

Figure 1.12 Spots originating from the chaotic regions in the SEB west of the GRS. The range for every frame is (10°S-24°S, 320°-190°). Time increases down page 1 and then down page 2. The time of the first sub-image is Nov 10, 2000. The time between two neighboring sub-images is 20 hours. Two examples of compact spots originating from the SEB and being absorbed finally by the GRS are shown with dark arrows. Tracing these spots from lower left to upper right (backwards in time), we find that all of them come from the chaotic regions in the SEB west of the GRS. In addition, two bright probable convective storms are shown with white arrows.

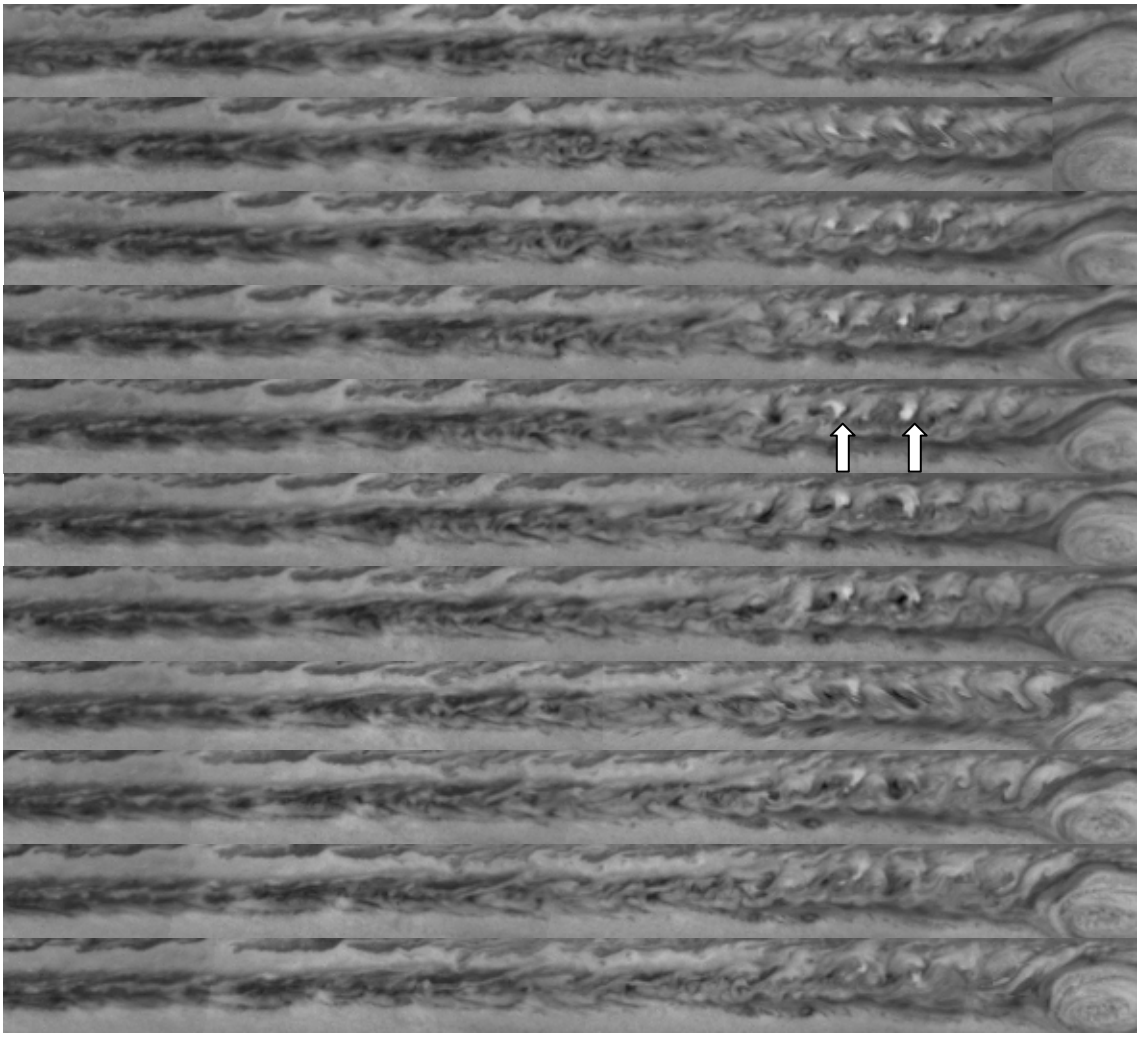

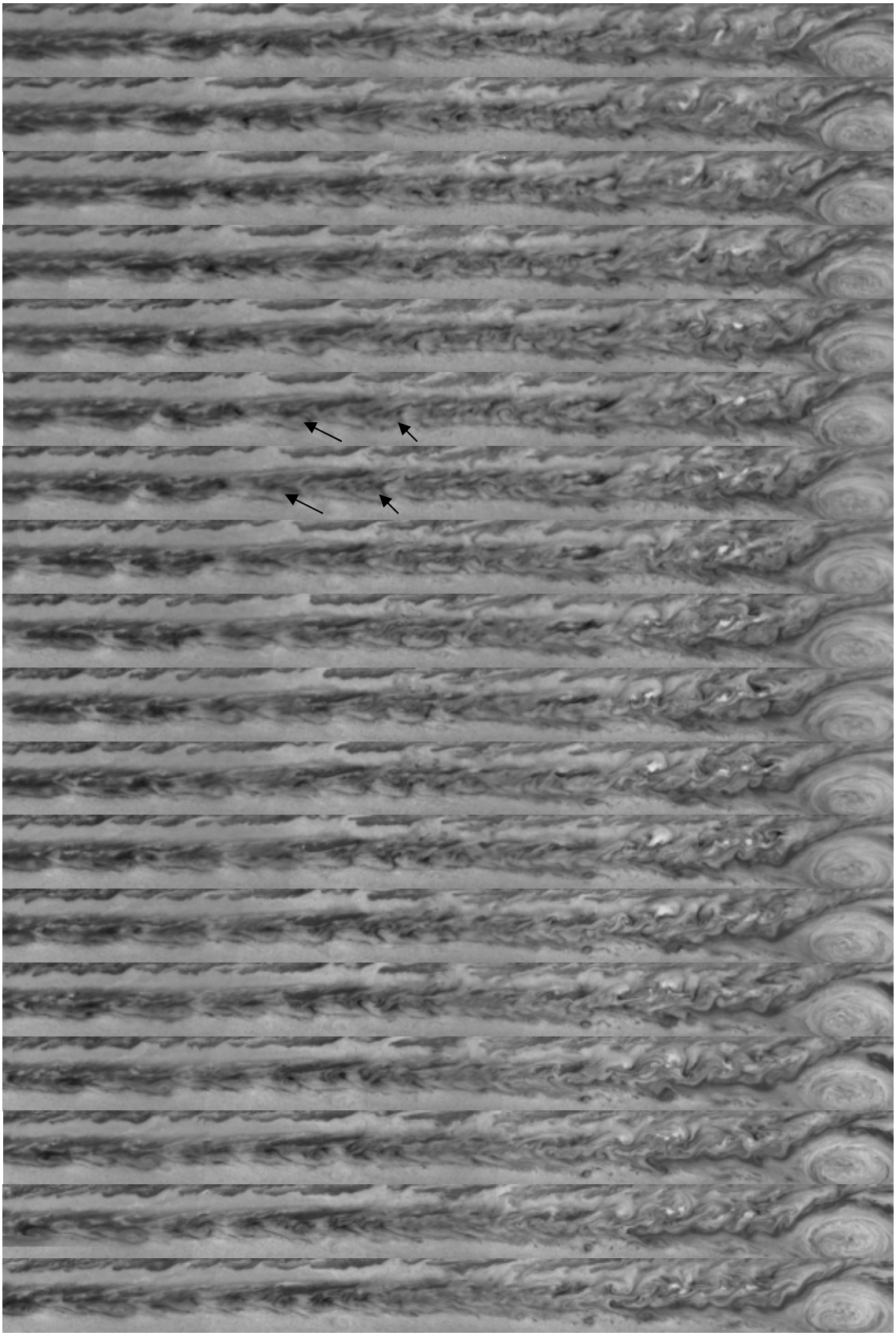

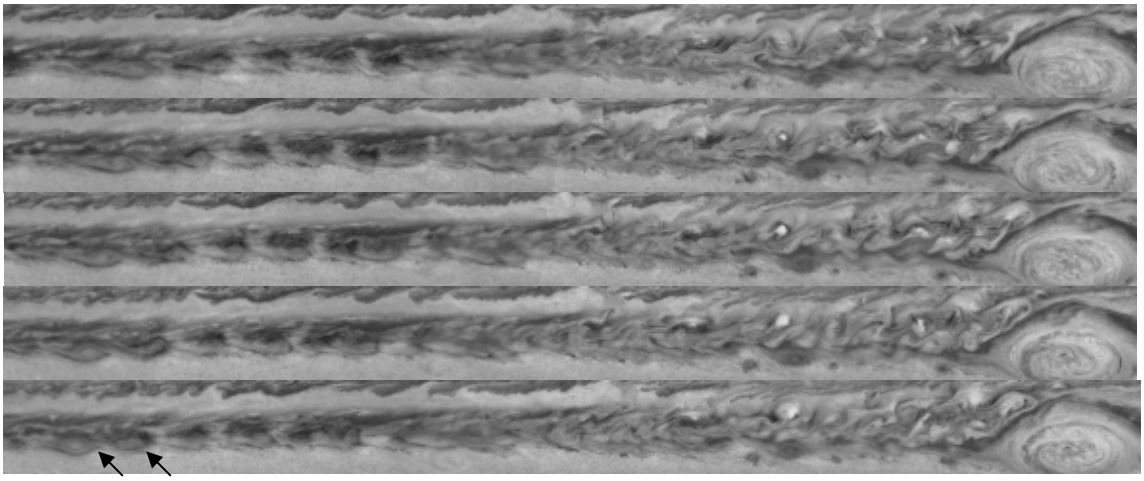

Chapter 2: Vertical Wind Shear on Jupiter from Cassini Images

2.1 Abstract

Multi-filter images of Jupiter acquired by the Cassini Imaging Science Subsystem (ISS) are used to derive zonal winds at altitudes above and below the visible cloud deck. Small features unique to the ultraviolet images of ISS are tracked to get the systematic high-altitude zonal winds. Comparison between the zonal winds from ultraviolet images and the vertical profile of zonal winds from the Cassini Composite Infrared Spectrometer (CIRS) shows that the zonal winds from the ultraviolet images are from a pressure level that is ~ 0.2 scale heights higher than the pressure level of the zonal winds from continuum-band images. Deeper zonal winds at different latitudes of the equatorial region are measured by tracking cloud features observed within hot spots on continuum-band images. The deeper zonal winds in this study extend the measurement of the Galileo probe to different latitudes of the equatorial region. Comparison between the Galileo probe and this study suggests that these fast-moving clouds within hot spots are deeper than 3 bars and are therefore probably water clouds.

2.2 Introduction

The vertical structure of zonal winds on Jupiter is critical for understanding the origin of the global-scale circulation on the giant planet [*Barcilon and Gierasch*, 1970; *Gierasch*, 1976; *Ingersoll and Pollard*, 1982; *Busse*, 1992]. Most measurements of zonal winds from ground-based telescopes, Voyager, HST, Galileo, and Cassini are limited to motions within the visible cloud deck and are made by tracking clouds in sequences of images taken at time intervals of ~1 hour to ~1 day [*Garcia-Melendo and Sanchez-Lavega*, 2001; *Ingersoll et al.*, 1979; *Ingersoll et al.*, 1981; *Limaye*, 1986; *Limaye*, 1989; *Porco et al.*, 2003; *Rogers*, 1995; *Simon*, 1999; *Smith*, 1976; *Vasavada et al.*, 1998]. In this paper, the visible cloud deck refers to the features seen at visible wavelengths in broadband continuum filters. Although the chemical components and pressure levels are uncertain [*Banfield et al.,* 1998; *Irwin et al.,* 2005], the principal cloud is probably ammonia (NH_3) at a pressure level around 0.7 bar, in agreement with the classical cloud scheme from thermodynamic modeling [*Atreya et al.,* 1997].

The Galileo Doppler Wind Experiment (DWE) is the only measurement of the winds below the visible cloud deck [*Atkinson et al.*, 1998]. High-altitude zonal winds decaying with altitude above the visible cloud deck are suggested by the Voyager Infrared Interferometer Spectrometer (IRIS) thermal measurements and the thermal wind equation [*Gierasch et al.*, 1986]. Several attempts to detect vertical wind shear by tracking clouds in images at different wavelengths were inconclusive [*Simon*, 1999; *Garcia-Melendo and Sanchez-Lavega*, 2001]. Banfield *et al* [1996] measured high-altitude zonal winds at

limited sites in the southern hemisphere of Jupiter by studying the impact debris from Comet Shoemaker-Levy 9. Vincent *et al* [2000] performed measurements of the zonal motions in Jupiter's high-altitude atmosphere by tracking selected features on the HST ultraviolet images, but the measurements are limited by poor limb-darkening correction of images in low latitudes and irregular intervals between images ranging from 10 to 70 hours. Here we present the Cassini imaging data that yield the zonal winds above and below the level of the visible cloud deck.

The Cassini flyby of Jupiter produced a wealth of scientific data. The wide spectral range of the Imaging Science Subsystem (ISS), from the ultraviolet (UV) into the near-infrared (near-IR), can discriminate Jupiter's multi-level clouds and hazes [*Porco et al.,* 2003]. Multi-filter ISS images taken at different times make it possible to measure zonal winds at different pressure levels by tracking multi-level clouds and hazes. During the encounter, the Cassini Composite Infrared Spectrometer (CIRS) returned spectra of the jovian atmosphere from 10-1400 cm^{-1} (1000-7 μm) at a programmable spectral resolution of 0.5 to 15 cm^{-1}. The vertical profile of zonal winds above the visible cloud deck has been estimated by combining the temperature maps constructed from these spectra with the thermal wind equation [*Flasar et al.*, 2004; *Simon-Miller et al*., 2005]. The simultaneous observations of the ISS and the CIRS offer an unprecedented opportunity to compare estimates of the zonal winds above the visible cloud deck from these two subsystems of Cassini.

The Galileo probe entered into a 5-micron hot spot, which is a hole in the visible cloud deck [*Young*, 2003]. The wind velocity was ~100 m/s at the level of the visible cloud deck, which agrees with the cloud-tracked winds for the latitude (7.4°N planetographic) at which the probe entered. From there the winds increased to 180 m/s at the 4-5 bar level. After that, the winds stayed constant at 170-180 m/s down to the 21 bar level [*Atkinson et al.,* 1998]. Seen from outside the atmosphere, the hot spots appear to move with most of the other visible cloud features in Jupiter's bright equatorial band (7°-10°N) [*Vasavada et al.*, 1998]. If there are clouds at deeper levels, it should be possible to see them through holes in the upper clouds – they should appear as small clouds within the hot spots. We have examined some of the hot spots in the continuum filter (CB2), where the gases are transparent and the only significant opacity above 10 bars is due to clouds [*Banfield et al.,* 1998], to check the possibility of measuring the deep wind by tracking these deep clouds through the hot spots.

2.3 Description of image sets

The ISS images analyzed in Section 3 consist of narrow-angle camera (NAC) images in 9 filters (UV1, BL1, GRN, MT1, CB1, MT2, CB2, MT3, and CB3) acquired over a 45-day period (October 1 to November 14, 2000) [*Porco et al.*, 2004]. The ISS images analyzed in Section 4 include additional CB2 images after the 45-day period (November 15 to December 9, 2000) and 1×2 North-South mosaics acquired every 63 minutes in a separate image set (December 11-13, 2000). Information including center wavelength, observation time, and effective pressure level (optical depth $\tau = 1$ in the absence of cloud

opacity) for the 9 filters are shown in Table 1. The methane filters MT1, MT2, and MT3 are centered on weak, medium, and strong absorption bands, respectively. The continuum filters CB1, CB2, and CB3 are paired to the corresponding MT filters, but are at wavelengths where the atmospheric gases are relatively transparent. Global mosaics of the same filter are separated by either 10 or 20 hours. Mosaics of different filters are taken 40 seconds apart so that each 9-filter set is near-simultaneous.

Each image was navigated by fitting (in the image plane) the observed planetary limb to its predicted location. This procedure locates the limb to a precision much less than one pixel, but may introduce systematic errors due to imprecise knowledge of the altitude of limb-defining opacity. However, wind measurements are performed on images that were navigated using the same portion of the planetary limb, resulting in systematic errors that occur in the same direction and that are partially mitigated by a relative wind measurement. The spatial resolution in the image plane of the October-November data ranged from 506-262 km/pixel, while that in the December data is ~120 km/pixel. The full width at half maximum (FWHM) of the point spread function (PSF) of the NAC through the clear filters is 1.3 pixels. At these resolutions, a one-pixel uncertainty in the navigation of the raw images would result in wind-speed errors of 3-14 m/s at the equator, when measured using images separated by 10 hours. Navigation error can be estimated directly when the images are mapped and combined into global mosaics. Inspection of the overlap regions reveals errors of less than a few map pixels, often less than one map pixel (one map pixel is 0.1 degree, or ~125 km at the equator), giving an error of less than 3 m/s in wind speed. Radiometric calibration was performed using the

CISSCAL software developed by the Cassini ISS Team [*Porco et al*., 2004]. The map projection is simple cylindrical (rectangular) with equal increments of planetocentric latitude and longitude. Every map is 1801×1801 pixels (180 degrees of latitude and longitude at 0.1 degree per pixel). In this paper, we use planetographic latitude and west longitude defined in System III [*Riddle and Warwick*, 1976].

2.4 High-altitude winds

Figure 1 shows an example of the near-simultaneous 9-filter maps. The same features show up in most of the filters, indicating that one is viewing the same clouds at roughly the same altitudes in most of the images. The UV1 map differs the most from the others, suggesting that it is viewing features at a different altitude. Previous wind measurements trying to detect zonal winds at different altitudes [*Garcia-Melendo and Sanchez-Lavega*, 2001; *Simon*, 1999] probably track the same features appearing in different wavelength images so that no significant velocity differences between these different wavelength images are detected. Many features in the Cassini images behave the same way. Figure 2 shows an example where the same features appearing in different filter maps have the same velocities. Here we show 4-filter maps (UV1, MT3, MT2, and MT1) with significantly different effective pressure levels (350 mbar for UV1, 600 mbar for MT3, 4 bar for MT2, and 10 bar for MT1) under cloud-free conditions. The two ovals existing in longitude 123° and 167° appear in the four filters of Fig.2, which suggests that the two ovals have large vertical structure. Furthermore, each of the two ovals keeps the same positions in the four filters even after 15 days (groups **A** and **B** of Fig. 2 are separated by

15 days). It shows that the vertical shear of ambient zonal winds (if there is any) does not shift the vertical structure of the two ovals, probably because the ovals are coherent in the vertical. In addition, the anti-correlation of brightness in UV1 and MT3 (dark in UV1 and bright in MT3) suggests that the ovals have UV-absorbing components at high altitude that appear dark relative to the Rayleigh scattering gas. These same components appear bright in MT3 relative to the methane absorbing gas. An exception to the anti-correlation between UV1 and MT3 is shown in Fig. 3. The moist convective storm shown in Fig.3 has a bright appearance in both UV1 and MT3, which suggests that the cloud particles are bright in the UV and penetrate to higher altitude than the effective pressure level of UV1 ~ 350 mbar. The moist convective storm keeps the same position in the four filter images of each group **A** and **B** (separated by 20 hours), which also suggests that the vertical shear of the ambient zonal winds does not affect the vertical structure of the moist convective event.

We selected small features unique to the UV1 filter images in order to track high-altitude winds. A sample of such features is shown in Fig. 4. Column A and B are two multi-filter image sets separated by 20 hours. The dark feature sitting at latitude 24º in the UV1 image, which does not appear in the MT3 and CB3 images, suggests that this feature is high-altitude UV-absorbing haze. The feature has a velocity of 110 m/s, which is slower than the corresponding velocity, 130 m/s, in the CB2 filter at the same latitude. Figure 4 also shows that the dark feature changes shape during the 20-hour period. The rapidly-varying characteristic of features in UV1 filter combined with lower feature contrast in the UV1 filter makes it difficult to measure zonal winds by an automated correlation

method [*Limaye et al.*, 1982]. Therefore, we manually track these features unique to the UV1 images to measure the high-altitude zonal winds. Features appearing in both UV1 images and other filter images are not included in this study. We increase the feature contrast of UV1 images by removing the mean value of every constant-latitude line of the UV1 images and utilizing the VICAR software developed by the Jet Propulsion Laboratory. Most of these features have sizes less than 4 degrees in latitude and longitude, which are equivalent to 4000 km at latitude 30 degree and are much larger than the spatial resolution, which is 500-250 km/pixel during the observing epoch (October 1 to November 14, 2000). Some features are bright relative to their surroundings and others are dark. The features we tracked have different shapes (ovals, elongated, and irregular). All the above characteristics of these features unique to UV1 images are independent of latitude.

Table 2 summarizes our measurements of high-altitude zonal winds by tracking these small features unique to the UV1 images. The uncertainties of zonal winds (column 3 of table 2), which are estimated by the standard deviation of the multiple measurements, vary around 10 m/s with the maximal value less than 20 m/s. In Fig. 5A we present all 1529 measurements of high-altitude zonal winds by tracking small features unique to the UV1 images. The solid curves in Fig. 5B are the zonal wind profiles derived from the continuum filter CB2 images, with the black solid line coming from the automatic correlation method [*Porco et al*., 2003] and the red solid line coming from the manual-tracking method [*Li et al.,* 2003]. The points with error-bars in Fig. 5B are averages in 1° latitude bins of individual velocity vectors shown in Fig. 5A. The error-bars are estimated

by the standard deviation of these individual velocity vectors within the 1° latitude bins. The figure shows that the winds in UV1 are slower than those in CB2 except near zero latitude. The differences between the UV1 zonal winds and the CB2 zonal winds, which are displayed in Fig. 6, further suggest that relatively large differences are concentrated in the centers of westward and eastward jets. This is consistent with the inference from the thermal wind equation that the winds decay with altitude in the high troposphere of Jupiter [*Geirasch et al*., 1986; *Flasar et al.,* 2004].

Figure 7 shows a comparison between the average UV1 zonal winds and the results from the CIRS data [*Flasar et al.,* 2004; *Simon-Miller et al*. 2005]. In Fig. 7, the blue and red lines are the zonal winds at 499 mbar and 315 mbar, respectively, inferred by integrating the thermal wind equation. The integration starts with the cloud-tracked wind profile derived from the CB2 filter of Cassini imaging data [*Porco et al*., 2003], assigning it to the 600-mbar level, and uses the temperatures derived from the Cassini CIRS data to integrate upward [*Simon-Miller et al*. 2005]. The points in Fig. 7 are the same as those shown in Fig. 5B, and represent the high-altitude zonal wind from the UV1 filter. Figure 7 shows a good match between the UV1 zonal wind and 499-mbar zonal winds from the CIRS data. The match suggests that the UV1 zonal winds probably correspond to a pressure level that is around 499 mbar if we assume the pressure level of CB2 zonal winds is 600 mbar. The 499-mbar pressure level of UV1 zonal wind is reasonable based on the optical characteristics of UV1 filter. The effective pressure level of the UV1 filter with optical depth $\tau = 1$ is 350 mbar (Table 1). It is not much different than 499 mbar, so the contrast from deeper atmosphere (499 mbar) can propagate up to higher level (350

mbar) via scattering. The Pioneer experiences on Venus show that we see through a UV scattering gas and haze down to about $\tau = 2-3$ quite easily [*Delgenio and Rossow*, 1990]. The recent Cassini observations of Titan also verify that we can see the surface in CB3 filter with the optical depth $\tau = 3$ at surface [*Porco et al*., 2005]. Therefore, if these feature contrasts in UV1 images are produced at 499 mbar they can still be seen at the top of the atmosphere. At latitudes > 35°N the stratospheric haze has significant opacity, especially in the ultraviolet (West *et al.,* 2004). This suggests that the UV1 zonal winds correspond to higher altitudes (pressures < 0.5 bar) than the UV1 winds at lower latitudes. Unfortunately, the vertical structure of zonal winds from the CIRS [*Flasar et al.*, 2004; *Simon-Miller et al*., 2005] does not show obvious vertical changes of zonal winds above 0.5 bar for latitudes > 35°N, so that it is difficult to estimate the pressure level of the UV1 zonal winds at latitudes > 35°N from the CIRS data.

The exact altitude of the UV1 zonal winds depends on the choice of 600 mbar as the level to start the integration of the CIRS data, and that has a large uncertainty. Estimates range from 0.5 bar to 1.0 bar [*Banfield et al.,* 1998; *Irwin et al.,* 2005]. A safer statement is that the features used for cloud tracking in the UV are ~ 0.2 scale heights higher than those used in CB2, which follows because the measured temperature gradient determines the wind shear with respect to log (*P*), *i.e.,* scale heights. In addition, the resolution of the CIRS data (~ 2.5° of latitude) and the UV1 average zonal winds in this study (~ 1° of latitude) are much lower than the resolution of the CB2 zonal wind (~ 0.1 of latitude), which suggests that the high-altitude zonal winds from this study and the CIRS may have lost some fine structures.

This difference in resolution could account for some of the difference between the UV1 profile and the CB2 profile shown in Fig. 5, but it is a small effect. If the zonal velocity profile were a sinusoid with wavelength L, averaging in a box of width h would reduce the apparent amplitude by a factor $\sin x / x$, where $x = \pi h / L$. For $h = 1°$ and $L = 10°$, this factor is 0.98. For $h = 1°$ and $L = 5°$, which is the wavelength at high latitudes, the factor is 0.94. Both of these factors correspond to a small reduction in amplitude compared to the reduction from CB2 to UV1 shown in Fig. 5.

Previous measurements of high-altitude zonal winds utilizing the debris of Comet Shoemaker-Levy 9 [*Banfield et al.,* 1996] and using the UV filter at 218 nm [*Vincent et al.,* 2000] also show zonal winds decreasing from the principal cloud deck. In this respect, our UV1 zonal winds are consistent with the previous measurements. However, previous measurements [*Banfield et al*., 1996; *Vincent et al*., 2000] refer to higher altitudes (a few tens of millibars) than the estimated pressure level of the UV1 measurement in this study. The higher altitude is where the impact debris of Comet Shoemaker-Levy 9 was deposited [*Banfield et al.,* 1996]. In addition, the UV filter at 218 nm is at a shorter wavelength than Cassini's UV1 filter [*Vincent, et al.,* 2000]. The estimation of the pressure level in the previous wind measurements utilized the decay rate of zonal winds at 270 mbar derived by the Voyager IRS data [*Gierasch et al.,* 1986] and assumed the decay rate keeps constant through the upper troposphere to stratosphere [*Banfield et al*., 1996; *Vincent et al*., 2000]. The CIRS data generates a zonal wind profile in a wide altitude range (600 mbar to less than 1 mbar) [*Flasar et al.,* 2004] so it offers an

opportunity to check the pressure level of wind measurements in the previous studies.

The thermal wind equation does not hold at the equator, so we estimate the vertical change of the zonal wind at the equator by extrapolating the thermal winds at ± 3° latitudes. The extrapolation for both 315 mbar and 499 mbar (Fig. 6) suggests that the vertical shear of zonal winds near the equator would have the same sign as the thermal wind shear at ± 3° latitude, which has winds decreasing with altitude. However, Fig. 5B shows that the UV1 zonal winds are not less than the CB2 zonal winds within ± 3° of the equator, which means that zonal winds do not decrease with altitude. The different sense of vertical shear of zonal winds near the equator probably offers some clues to the mechanisms of prograde equatorial jets on the giant planets, and is worthy of further study.

2.5 Low-altitude Winds

The information on deep winds is relatively scarce compared to that on high-altitude winds because of obscuration from over-lying clouds. The DWE on the Galileo probe measured the deep zonal wind profiles to the 22-bar pressure level [*Atkinson et al.*, 1998], but this measurement was limited to a single site at 7.4° N. The probe entered one of Jupiter's 5-μm hot spots, where a hole 5000 km wide exists in the visible top clouds. Fortunately, some deeper clouds are detected through the hot spots in the Cassini ISS high-quality images. The motions of these deeper clouds make it possible to directly measure the deeper zonal winds below the visible top clouds.

The left column A of Fig. 8 is a time sequence of CB2 images separated by 10.5 hours, in which a cloud feature moves across a hot spot from west to east. The cloud feature has a velocity of 175 m/s, which is much stronger than the corresponding CB2 zonal wind in the visible cloud deck (110 ± 20 m/s at this latitude). The hot spots move at the latter speed. The substantial vertical shear suggested by Fig. 8 is consistent with the Galileo DWE and the numerical simulation [*Showman and Dowling*, 2000]. The right column B is a multi-filter image set corresponding to the top panel of A. The MT3, MT2, CB2 images of column B are near-simultaneous images separated by 40 seconds. The multi-filter images show that the cloud is visible in CB2 and MT2 and invisible in MT3, which suggests that the cloud is not a high-altitude feature. Therefore, the cloud pointed to by white arrows in Fig. 8 is probably a deeper cloud below the visible cloud deck. There are two kind of clouds below the principal cloud deck: ammonia hydrosulfide (NH_4SH) with cloud base ~ 2 bars and water (H_2O) with cloud base ~ 6 bars [*Atreya et al.,* 1997]. In addition, the fact that the cloud is visible in MT2 images suggests that the top of the cloud is above the 3-bar level, which is the pressure level of the optical depth $\tau = 1$ for the MT2 filter [*West et al.*, 2004]. Model simulations [*Delgenio and McGrattan*, 1990; *Hueso and Sanchez-Lavega*, 2001] suggest that strong moist convection, originated at the pressure level ~ 5 bars, can extend above the 0.5-bar pressure level on Jupiter. The moist convective storm appearing in 4-filter maps of Fig. 3 also shows that some convective storms have large vertical extent. Based on these factors, the features within hot spots could be either ammonium hydrosulfide clouds, whose cloud base is ~2 bars or water clouds that extend above 3 bars.

The previous wind measurements in the regions of hot spots [*Hueso and Sanchez-Lavega,* 1996; *Vasavada et al.,* 1998] mainly tracked features around the hot spots. In this study, these features we tracked are different from these features measured in the previous two papers [*Hueso and Sanchez-Lavega,* 1996; *Vasavada et al.,* 1998]. They move across the centers of hot spots and have faster zonal wind than the zonal winds at the principal cloud deck, which suggests that these features moving across the hot spots probably are deep clouds and are mainly controlled by the deep faster ambient zonal wind.

Figure 9 shows the measurements of deep zonal winds by tracking these cloud features observed within hot spots and comparison with the results of Galileo DWE. In total, 15 cloud features sitting at 13 different latitudes of the equatorial regions of Jupiter are tracked in this study. Our deep zonal winds at different latitudes (from latitude 6° to 9° N) extend the results of Galileo DWE, and are consistent with the theoretical and numerical results of deep convection models, which say that the strong equatorial prograde jets of the giant planets penetrate to deep levels [*Busse*, 1976; *Sun et al.*, 1993; *Christensen*, 2001; *Aurnou and Olson*, 2001; *Yano et al.*, 2003]. The velocity that we measure at the latitude of the Galileo probe (7.4° N planetographic) is around 170 m/s, which is equal to the zonal wind at the 3-bar pressure level determined by the Galileo probe (bottom panel of Fig. 8) [*Atkinson et al.,* 1998]. If the Galileo probe results in 1995 can be applied to the Cassini flyby in 2000, the ammonium hydrosulfide (NH_4SH) cloud can be ruled out as a candidate for the deeper clouds detected through hot spots because

the temperature at the 3 bar level is too high for ammonium hydrosulfide to condense. Therefore, the cloud features detected through hot spots are probably thick water clouds extending above 3 bars.

2.6 Conclusions

High-quality images from the Cassini ISS, acquired in 9 filters, are used to measure the high-altitude and low-altitude zonal winds of Jupiter. The first systematic measurements of the high-altitude zonal winds by tracking these small features unique to UV1 images certify that the winds are weaker at the higher altitudes. Winds at the lower altitudes are measured by tracking cloud features through hot spots. The deep zonal winds are consistent with the results from the Galileo probe, provided the clouds are at a pressure level around 3 bars. These new results will shed light on the dynamics of the jovian atmosphere and the internal structure of Jupiter.

2.7 References

Atkinson, D.H., J.B. Pollack, and A. Seiff, The Galileo Probe Doppler Wind Experiment: Measurement of the deep zonal winds on Jupiter, *Journal of Geophysical Research-Planets*, *103* (E10), 22911-22928, 1998.

Atreya, S. K., M.H. Wong, T. C. Owen, H. B. Niemann, and P. R. Maha.y, Chemistry and clouds of the Jupiter's atmosphere: A *Galileo* perspective, in *The Three Galileos the Man, the Spacecraft the Telescope*, p. 249, 1997.

Aurnou, J.M., and P.L. Olson, Strong zonal winds from thermal convection in a rotating spherical shell, *Geophysical Research Letters*, *28* (13), 2557-2559, 2001.

Banfield, D., P.J. Gierasch, S.W. Squyres, P.D. Nicholson, B.J. Conrath, and K. Matthews, 2 □m spectrophotometry of Jovian stratospheric aerosols - Scattering opacities, vertical distributions, and wind speeds, *Icarus*, *121* (2), 389-410, 1996.

Banfield, D., P.J. Gierasch, M. Bell, E. Ustinov, A.P. Ingersoll, A.R. Vasavada, R. A. West, and M.J.S. Belton, Jupiter's cloud structure from Galileo imaging data, *Icarus*, *135*, 230-250, 1998.

Barcilon, A., and P. Gierasch, A Moist, Hadley Cell Model for Jupiters Cloud Bands, *Journal of the Atmospheric Sciences*, *27* (4), 550-560, 1970.

Busse, F.H., Simple Model of Convection in Jovian Atmosphere, *Icarus*, *29* (2), 255-260, 1976.

Christensen, U.R., Zonal flow driven by deep convection in the major planets, *Geophysical Research Letters*, *28* (13), 2553-2556, 2001.

Delgenio, A.D., and K.B. McGrattan, Moist Convection and the Vertical Structure and Water Abundance of Jupiters Atmosphere, *Icarus*, *84* (1), 29-53, 1990.

Delgenio, A.D., and W.B. Rossow, Planetary-Scale Waves and the Cyclic Nature of Cloud Top Dynamics on Venus, *Journal of the Atmospheric Sciences*, *47* (3), 293-318, 1990.

Flasar, F.M., V.G. Kunde, R.K. Achterberg, B.J. Conrath, A.A. Simon-Miller, C.A. Nixon, P.J. Gierasch, P.N. Romani, B. Bezard, P. Irwin, G.L. Bjoraker, J.C. Brasunas, D.E. Jennings, J.C. Pearl, M.D. Smith, G.S. Orton, L.J. Spilker, R. Carlson, S.B. Calcutt, P.L. Read, F.W. Taylor, P. Parrish, A. Barucci, R. Courtin, A. Coustenis, D. Gautier, E. Lellouch, A. Marten, R. Prange, Y. Biraud, T. Fouchet, C. Ferrari, T.C. Owen, M.M. Abbas, R.E. Samuelson, F. Raulin, P. Ade, C.J. Cesarsky, K.U. Grossman, and A. Coradini, An intense stratospheric jet on Jupiter, *Nature*, *427* (6970), 132-135, 2004.

Garcia-Melendo, E., and A. Sanchez-Lavega, A study of the stability of jovian zonal winds from HST images: 1995-2000, *Icarus*, *152* (2), 316-330, 2001.

Gierasch, P.J., Jovian Meteorology - Large-Scale Moist Convection, *Icarus*, *29* (4), 445-454, 1976.

Gierasch, P.J., B.J. Conrath, and J.A. Magalhaes, Zonal Mean Properties of Jupiter Upper Troposphere from Voyager Infrared Observations, *Icarus*, *67* (3), 456-483, 1986.

Hueso, R., and A. Sanchez-Lavega, Motions in jovian hot spot-plume regions using voyager images, *Icarus*, *136* (2), 353-357, 1998.

Hueso, R., and A. Sanchez-Lavega, A three-dimensional model of moist convection for the giant planets: The Jupiter case, *Icarus*, *151* (2), 257-274, 2001.

Ingersoll, A.P., R.F. Beebe, S.A. Collins, G.E. Hunt, J.L. Mitchell, P. Muller, B.A. Smith, and R.J. Terrile, Zonal Velocity and Texture in the Jovian Atmosphere Inferred from Voyager Images, *Nature*, *280* (5725), 773-775, 1979.

Ingersoll, A.P., R.F. Beebe, J.L. Mitchell, G.W. Garneau, G.M. Yagi, and J.P. Muller, Interaction of Eddies and Mean Zonal Flow on Jupiter as Inferred from Voyager-1 and Voyager-2 Images, *Journal of Geophysical Research-Space Physics*, *86* (NA10), 8733-8743, 1981.

Ingersoll, A.P., and D. Pollard, Motion in the Interiors and Atmospheres of Jupiter and Saturn - Scale Analysis, Anelastic Equations, Barotropic Stability-Criterion, *Icarus*, *52* (1), 62-80, 1982.

Irwin, P.G.J., K. Sihra, N. Bowles, F.W. Taylor, and S.B. Calcutt, Methane absorption in the atmosphere of Jupiter from 1800 to 9500 cm^{-1} and implications for vertical cloud structure, *Icarus,* 176, 255-271, 2005.

Li, L., Ingersoll, A.P., Vasavada, A.R., Porco, C.C., Del Genio A. D., Ewald, S.P., Life cycles of spots on Jupiter from Cassini images. *Icarus,* 172, 9-23, 2004.

Limaye, S.S., Jupiter - New Estimates of the Mean Zonal Flow at the Cloud Level, *Icarus*, *65* (2-3), 335-352, 1986.

Limaye, S.S., Jupiter: Short-term variations of the mean zonal flow at the cloud level., *In Time-Variable Phenomena in the Jovian system (M. J. S. Belton, R. A. West, and J. Rahe, Eds)*, *NASA SP-494*, 311-323, 1989.

Limaye, S.S., H.E. Revercomb, L.A. Sromovsky, R.J. Krauss, D.A. Santek, V.E. Suomi, S.A. Collins, and C.C. Avis, Jovian Winds from Voyager-2 .1. Zonal Mean Circulation, *Journal of the Atmospheric Sciences*, *39* (7), 1413-1432, 1982.

Porco, C.C., R.A. West, A. McEwen, A.D. Del Genio, A.P. Ingersoll, P. Thomas, S. Squyres, L. Dones, C.D. Murray, T.V. Johnson, J.A. Burns, A. Brahic, G. Neukum, J. Veverka, J.M. Barbara, T. Denk, M. Evans, J.J. Ferrier, P. Geissler, P. Helfenstein, T. Roatsch, H. Throop, M. Tiscareno, and A.R. Vasavada, Cassini imaging of Jupiter's atmosphere, satellites, and rings, *Science*, *299* (5612), 1541-1547, 2003.

Porco, C.C., R.A. West, S. Squyres, A. McEwen, P. Thomas, C.D. Murray, A. Delgenio, A.P. Ingersoll, T.V. Johnson, G. Neukum, J. Veverka, L. Dones, A. Brahic, J.A. Burns, V. Haemmerle, B. Knowles, D. Dawson, T. Roatsch, K. Beurle, and W. Owen, Cassini Imaging Science: Instrument characteristics and anticipated scientific investigations at Saturn, *Space Science Reviews*, *115* (1-4), 363-497, 2004.

Porco, C.C., E. Baker, J. Barbara, K. Beurle, A. Brahic, J.A. Burns, S. Charnoz, N. Cooper, D.D. Dawson, A.D. Del Genio, T. Denk, L. Dones, U. Dyudina, M.W. Evans, S. Fussner, B. Giese, K. Grazier, P. Helfenstein, A.P. Ingersoll, R.A. Jacobson, T.V. Johnson, A. McEwen, C.D. Murray, G. Neukum, W.M. Owen, J. Perry, T. Roatsch, J. Spitale, S. Squyres, P. Thomas, M. Tiscareno, E.P. Turtle, A.R. Vasavada, J. Veverka, R. Wagner, and R. West, Imaging of Titan from the Cassini spacecraft, *Nature*, *434* (7030), 159-168, 2005.

Riddle, A.C., and J.W. Warwick, Redefinition of System-3 Longitude, *Icarus*, *27* (3), 457-459, 1976.

Rogers, J.H., The Giant Planet Jupiter, *Cambridge University Press, New York*, 1995.

Showman, A.P., and T.E. Dowling, Nonlinear simulations of Jupiter's 5-micron hot spots, *Science,* 289, 1737-1740, 2000.

Simon, A.A., The structure and temporal stability of Jupiter's zonal winds: A study of the north tropical region, *Icarus*, *141* (1), 29-39, 1999.

Simon-Miller, A.A., B.J. Conrath, P.J. Gierasch, G.S. Orton, R.K. Achterberg, F.M. Flasar and B.M. Fischer, Jupiter's Atmospheric Temperatures: From Voyager IRIS to Cassini CIRS, *Icarus,* submitted, 2005.

Smith, B.A., Motion and morphology of clouds in the atmosphere of Jupiter, *in Jupiter, edited by T. Gehrels*, 564-618, 1976.

Sun, Z.P., G. Schubert, and G.A. Glatzmaier, Banded Surface Flow Maintained by Convection in a Model of the Rapidly Rotating Giant Planets, *Science*, *260* (5108), 661-664, 1993.

Vasavada, A.R., A.P. Ingersoll, D. Banfield, M. Bell, P.J. Gierasch, M.J.S. Belton, G.S. Orton, K.P. Klaasen, E. DeJong, H.H. Breneman, T.J. Jones, J.M. Kaufman, K.P. Magee, and D.A. Senske, Galileo imaging of Jupiter's atmosphere: The Great Red Spot, equatorial region, and White Ovals, *Icarus*, *135* (1), 265-275, 1998.

Vincent, M.B., J.T. Clarke, G.E. Ballester, W.M. Harris, R.A. West, J.T. Trauger, R.W. Evans, K.R. Stapelfeldt, D. Crisp, C.J. Burrows, J.S. Gallagher, R.E. Griffiths, J. Hester, J.G. Hoessel, J.A. Holtzman, J.R. Mould, P.A. Scowen, A.M. Watson, and J.A. Westphal, Jupiter's polar regions in the ultraviolet as imaged by HST/WFPC2: Auroral-aligned features and zonal motions, *Icarus*, 143, 205-222, 2000.

West, R.A., K.H. Baines, A.J. Friedson, D. Banfield, B. Ragent, F.W. Taylor, Jupiter: The Planet, Satellites and Magnetosphere, *Cambridge Planetary Science, edited by F. Bagenal, T. E. Dowling, W. B. McKinnon, D. Jewitt, C. Murray, J. Bell, R. Lorenz, F. Nimmo*, 2004.

Yano, J.I., O. Talagrand, and P. Drossart, Outer plants: Origins of atmospheric zonal winds, *Nature*, *421* (6918), 36-36, 2003.

Young, R.E., The Galileo probe: How it has changed our understanding of Jupiter, *New Astronomy Review*, 47,1-51, 2003.

Table 2.1 The information of the Cassini ISS 9 filters

Filter	λ_{center}	$\lambda_{effetive}$	Observation time	Pressure ($\tau = 1$)
UV1	258 nm	264 nm	Oct.1 – Nov. 14	350 mbar
BL1	451 nm	455 nm	Oct.1 – Nov. 14	4.5 bar
GRN	568 nm	569 nm	Oct.1 – Nov.14	10 bar
MT1	619 nm	619 nm	Oct.1 – Nov.14	10 bar
CB1	619 nm	619 nm	Oct.1 – Nov.14	> 10 bar
MT2	727 nm	727 nm	Oct.1 – Nov.14	4 bar
CB2	750 nm	750 nm	Oct.1 – Dec. 9, Dec.11 – Dec. 13	> 20 bar
MT3	889 nm	889 nm	Oct.1 – Nov.14	600 mbar
CB3	938 nm	938 nm	Oct.1 – Nov. 14	> 50 bar

Notes: Column 1 is the names of different filters. Column 2 and 3 are center and effective wavelengths of the different filters. The effective wavelengths are computed using the full system transmission function convolved with a solar spectrum [*Porco et al.,* 2005], which are more relevant to the optical characteristics of filters. Column 4 is the observation times for different filters. The last column is the effective pressure level, which is defined as optical depth $\tau = 1$ in the absence of cloud opacity. The effective pressure levels are estimated by taking account of Rayleigh scattering and methane-absorption for these ultraviolet, visible, and near-infrared filters [*West et al., 2003*].

Table 2.2 Zonal Wind by Tracking Features Unique to UV1 Images

Latitude (graphic)	Wind (m/s)	Error (m/s)	number	Latitude (graphic)	Wind (m/s)	Error (m/s)	number
54.8	9.4	---	1	-58.9	-1.3	6.9	3
53.6	0.0	---	1	-58.1	0.5	7.2	2
52.1	-8.9	---	1	-57.4	-3.9	---	1
50.7	-3.1	3.3	11	-54.8	-4.7	2.6	2
50.0	-2.1	4.0	22	-54.0	6.0	6.4	21
49.1	-1.0	4.3	14	-53.0	12.7	7.8	32
47.9	4.2	5.7	10	-52.0	10.0	6.3	22
46.8	2.5	3.2	6	-50.9	7.3	5.6	8
46.1	1.1	5.8	13	-50.1	5.1	6.8	19
45.0	2.6	4.8	27	-48.9	4.7	7.1	19
44.0	1.7	5.5	30	-48.0	-1.9	5.5	7
43.0	3.6	7.4	13	-47.0	11.6	8.8	7
42.1	1.1	6.9	37	-44.8	18.8	14.4	4
40.9	-0.2	6.5	60	-43.2	15.6	---	1
40.1	-4.7	5.8	88	-41.0	13.5	---	1
39.1	-4.7	6.8	65	-39.9	4.8	6.6	10
38.0	-3.0	7.3	34	-39.0	7.1	6.5	45
37.2	0.9	3.9	8	-38.4	11.8	6.3	2
36.0	-1.7	7.4	43	-36.8	14.2	0.0	1
35.1	10.7	11.5	8	-35.9	23.0	0.0	1
34.0	8.1	11.6	18	-35.2	10.1	1.5	2
33.0	3.5	12.2	35	-33.0	0.0	---	1
32.0	-2.3	18.0	4	-32.0	-2.8	5.9	19
30.9	-9.2	13.1	10	-31.1	3.3	5.3	90
30.0	-9.9	6.6	85	-27.5	28.0	---	1
29.4	-0.9	12.9	9	-26.8	19.8	2.9	3
28.3	32.5	---	1	-26.3	18.9	3.2	2
27.0	32.4	5.4	3	-23.8	9.1	5.9	3
26.2	60.8	17.1	8	-22.9	-15.5	18.8	11
25.2	95.1	---	1	-22.2	-21.5	16.4	27
23.7	111.5	8.4	30	-21.1	-32.9	11.8	6
23.3	108.6	6.7	64	-20.0	-38.7	10.0	23
22.2	72.3	19.7	3	-19.3	-40.7	8.4	11
20.9	57.1	19.0	2	-18.0	-16.9	10.8	15
19.7	27.0	12.2	11	-17.1	-13.0	9.0	17
19.1	9.2	10.0	32	-16.5	-10.0	---	1
18.3	3.0	7.2	5	-13.8	20.3	---	1
17.1	6.2	8.2	4	-12.9	22.9	2.6	2
15.9	3.6	8.2	17	-12.2	10.2	3.4	2
15.0	5.0	11.8	15	-11.1	47.5	15.9	7
13.9	16.3	6.6	9	-10.0	63.7	16.7	11
13.0	27.0	11.4	24	-9.2	73.3	11.8	23
12.0	30.2	10.0	29	-7.9	61.9	3.7	4
11.1	47.1	13.8	20	-7.0	95.9	17.4	10
10.2	49.7	9.8	13	-6.0	86.8	14.8	18
9.3	71.9	6.8	2	-5.0	89.3	16.2	17
7.9	82.5	3.4	2	-4.2	77.4	12.4	22
6.9	79.6	6.0	9	-1.0	88.4	7.9	3
6.1	76.3	7.7	4	-0.5	83.2	---	1
4.2	79.5	---	1				
1.1	81.7	11.2	6				

Notes: The planetographic latitudes in column 1 and 5 are average latitudes of the features tracked within the 1° latitude bin. Column 2 and 6 are the corresponding average zonal winds within the 1° latitude bin. Column 3 and 7 are uncertainties calculated by the standard deviation of the multiple measurements within the 1° latitude bin. Dash lines

in Column 3 and 7 indicate that only one measurement was done within the corresponding latitude bin. Column 4 and 8 are the number of measurements in the corresponding 1° latitude bin.

Figure 2.1 Map-projected images of the same area in nine filters. The images were taken at intervals of 40 seconds, which makes them virtually simultaneous. The mean value of every constant-latitude line in the MT3 and UV1 images is removed so that the feature contrast covered by the equatorial haze in MT3 and UV1 can be seen.

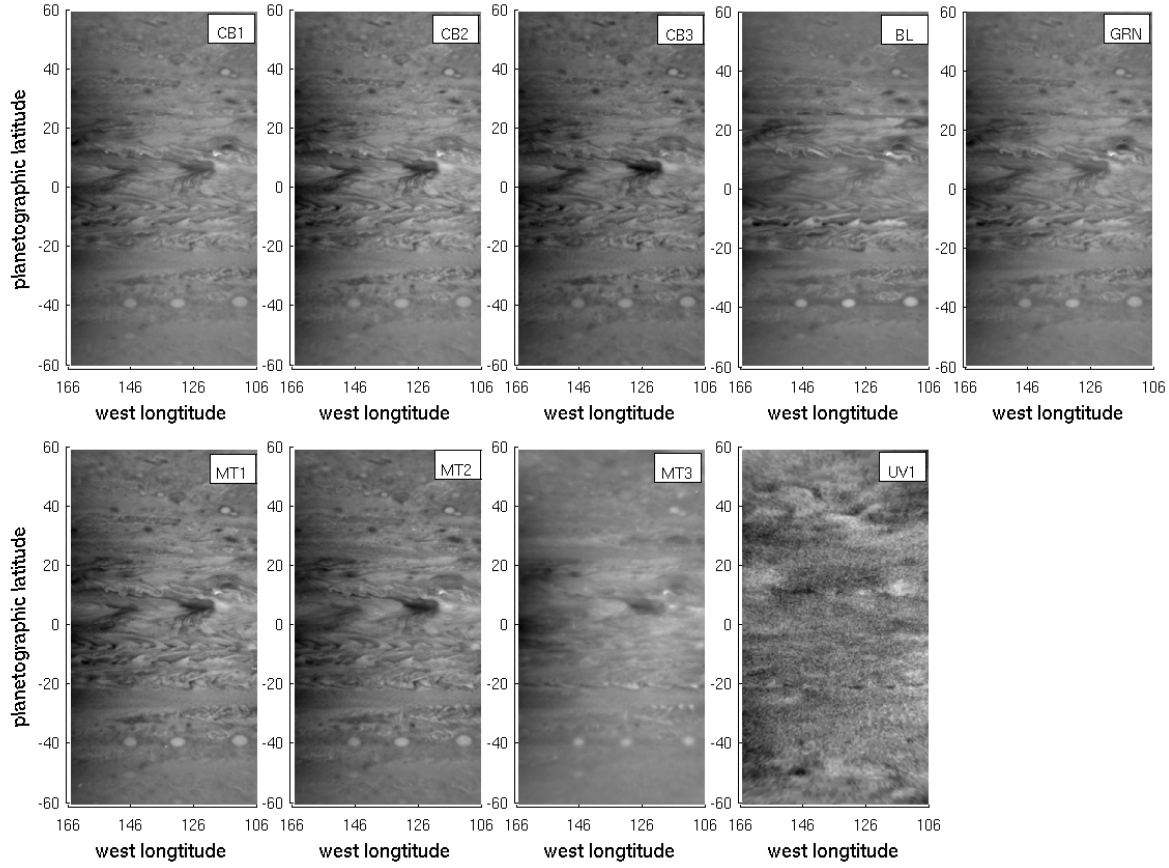

Figure 2.2 Features visible in UV1, MT3, MT2, and MT1 images at two different times. For columns **(A)** and **(B)** the UV1, MT3, MT2 and MT1 are near-simultaneous images separated by 40 or 80 seconds. The time separation between **(A)** and **(B)** is 15 days. The mean value of every constant-latitude line in the UV1 images is removed to make the feature contrast clear.

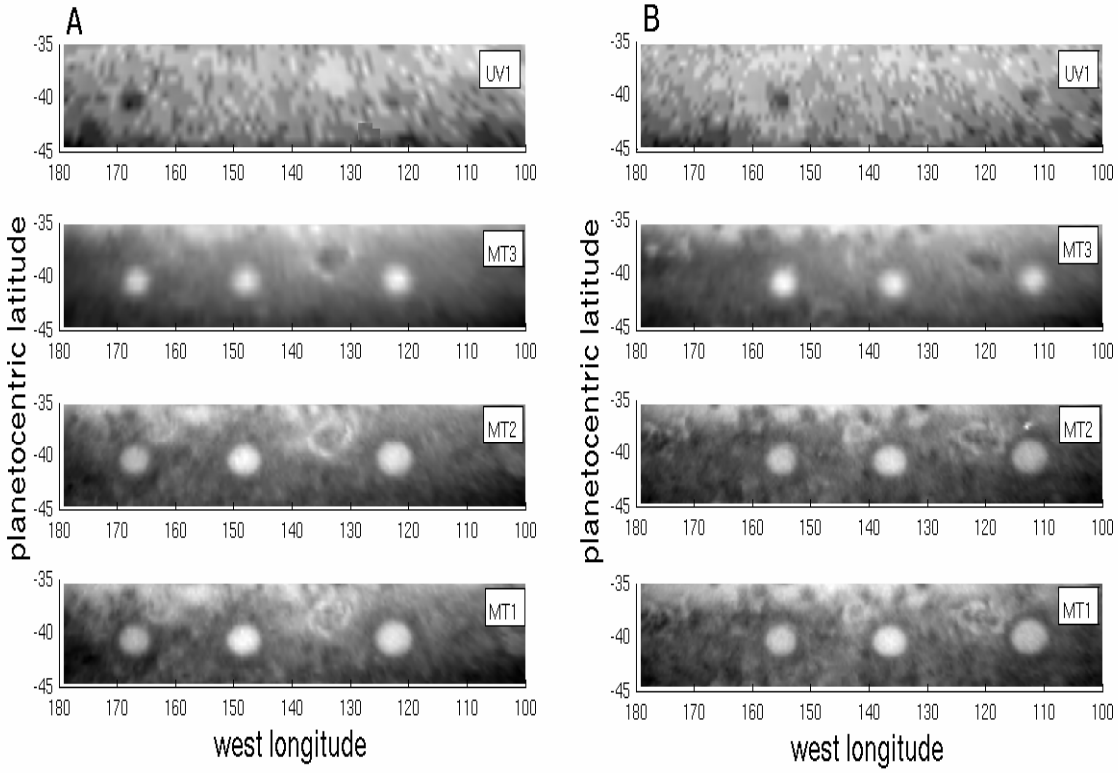

Figure 2.3 One moist convective storm visible in UV1, MT3, MT2, and MT1 images at two different times. For columns **(A)** and **(B)** the UV1, MT3, MT2 and MT1 are near-simultaneous images separated by 40 or 80 seconds. The time separation between **(A)** and **(B)** is 20 hours. The mean value of every constant-latitude line in the MT3 and UV1 images is removed to make the feature contrast clear.

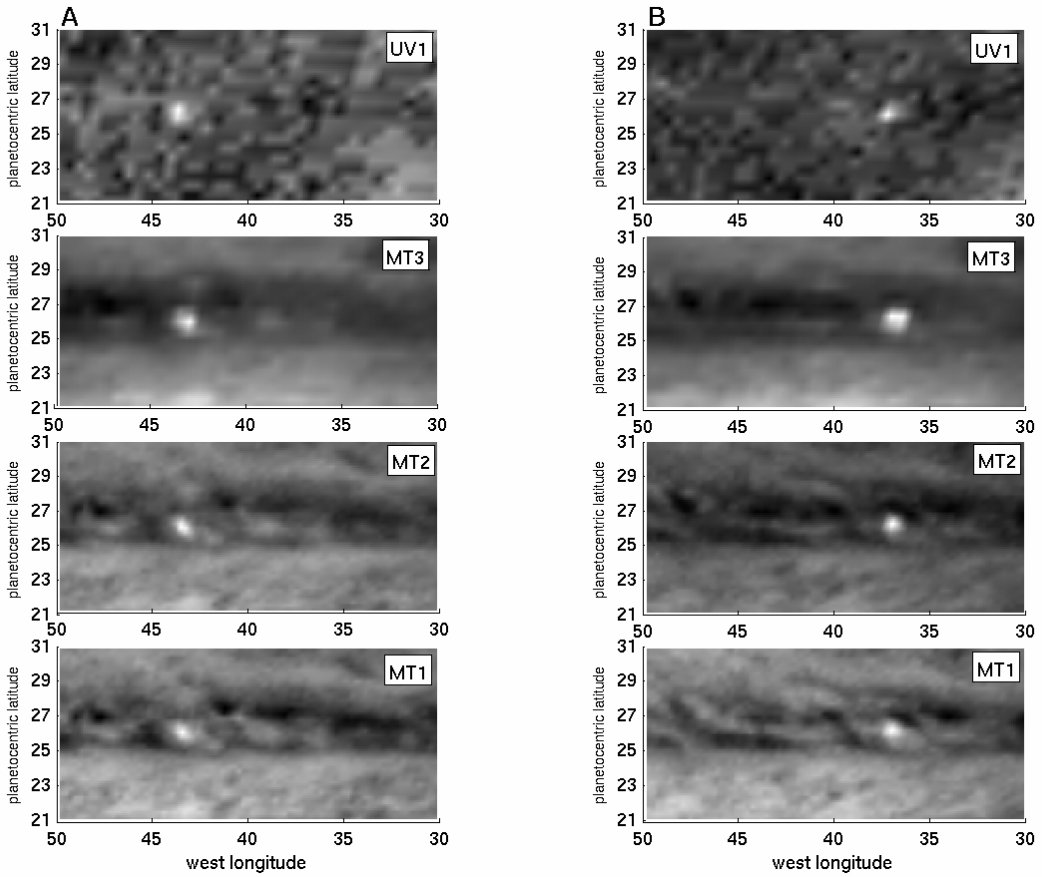

Figure 2.4 Feature visible in UV1 image and invisible in MT3 and CB3 images at two different times. For columns **(A)** and **(B)** the UV1, MT3, and CB3 are near-simultaneous images separated by 40 seconds. The time separation between **(A)** and **(B)** is 20 hours. The mean value of every constant-latitude line in the MT3 and UV1 images is removed to make the feature contrast clear.

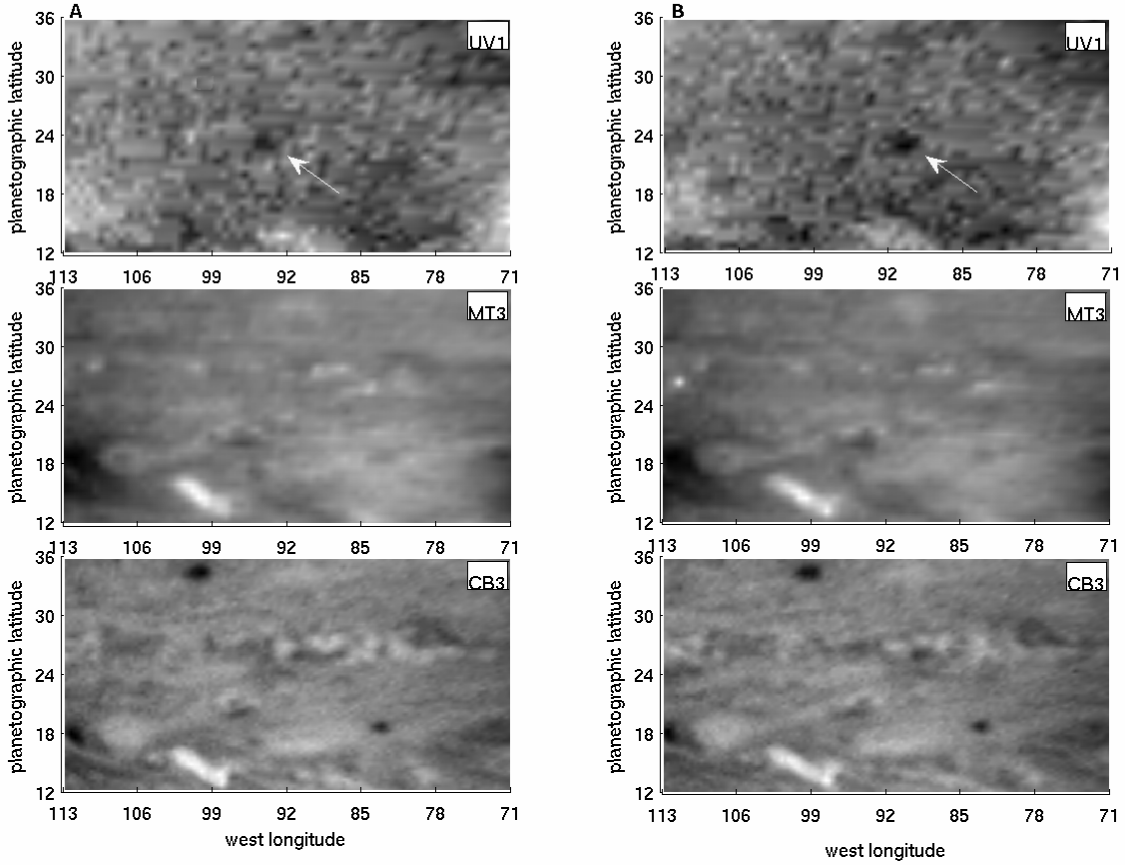

Figure 2.5 Measurements of zonal wind by tracking features unique to the UV1 images and comparison to the CB2 zonal wind profiles. **(A)** All 1529 measurements performed on the UV1 images. **(B)** Comparison of the average UV1 zonal winds and two zonal winds from CB2 images [*Porco et al.*, 2003; *Li et al.*, 2004]. Each dot in **(A)** represents a single measurement. Each dot in **(B)** represents the average zonal wind of these measurements in **(A)** within a 1° latitude bin. The $CB2_a$ zonal wind profile comes from automated correlation method utilizing 29 pairs of Cassini CB2 images separated by 10 hours [*Porco et al.*, 2003] and the $CB2_b$ comes from manually feature-tracking method utilizing CB2 images from Oct.1 to Dec.9, 2000 [*Li et al.*, 2004]. The uncertainties in **(B)** are estimated by the standard deviation of the multiple measurements within the 1°-latitude bins.

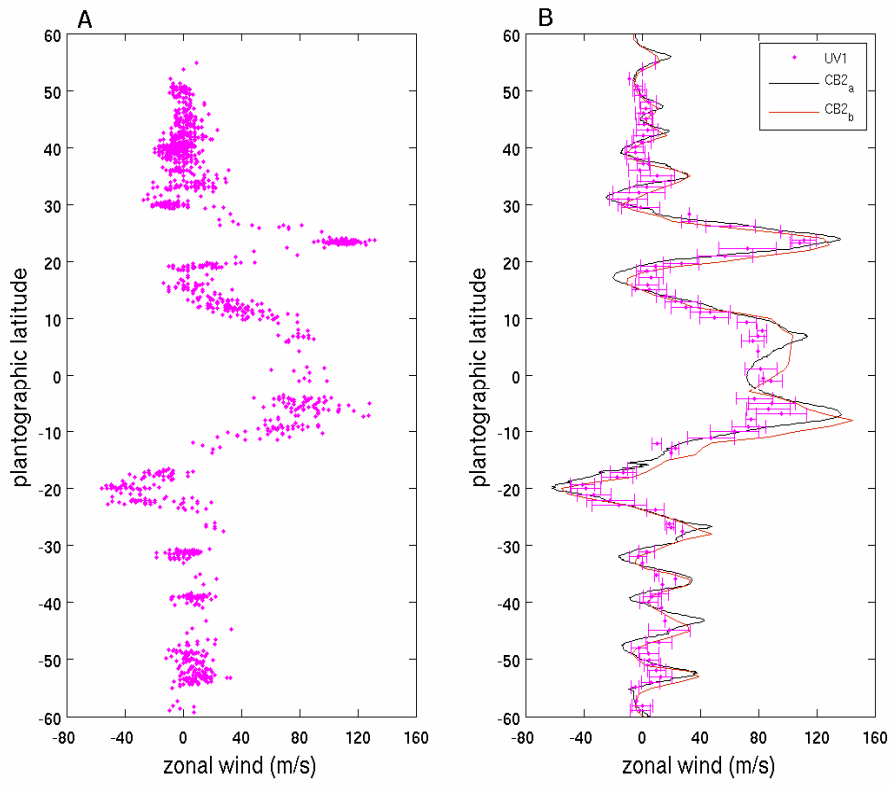

Figure 2.6 Differences between the UV1 zonal winds and the CB2 zonal winds. **(A)** Difference between the UV1 zonal winds and the $CB2_a$ zonal winds [*Porco et al.*, 2003]. **(B)** Difference between the UV1 zonal winds and the $CB2_b$ zonal winds [*Li et al.*, 2004].

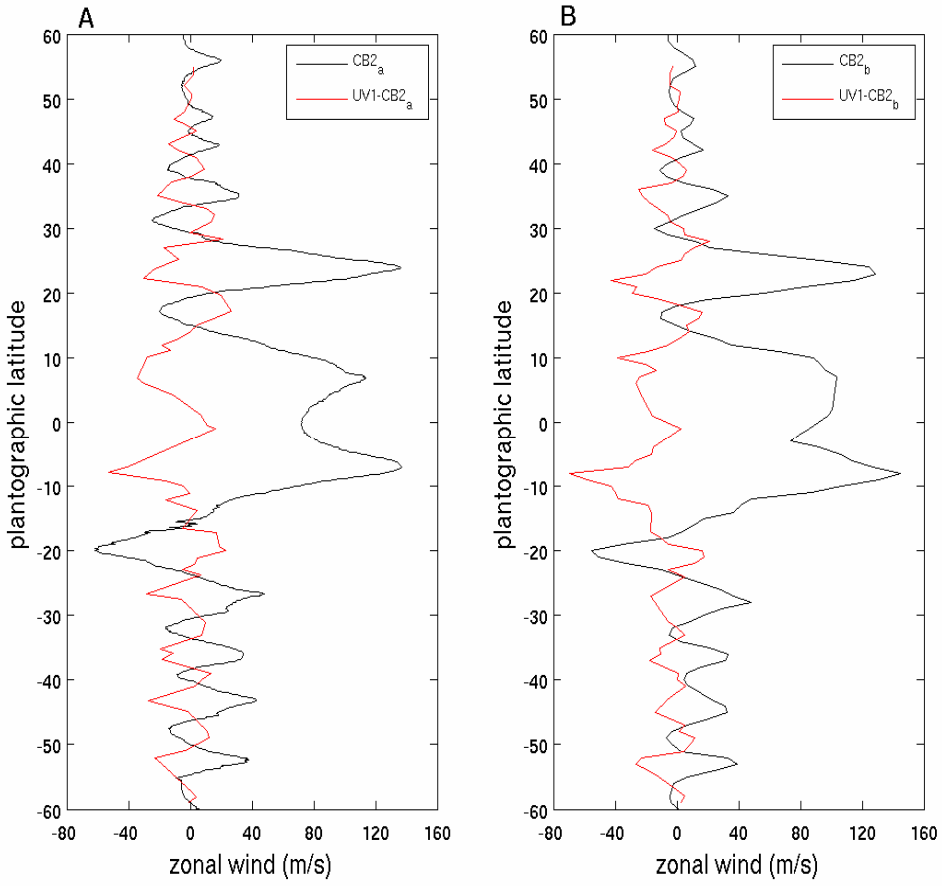

Figure 2.7 Comparison between the average UV1 zonal winds and the results from the CIRS data. The high-altitude zonal wind profiles at 315 mbar and 499 mbar come from the CIRS data on the assumption that the base zonal winds from CB2 are at 600 mbar [*Flasar et al.*, 2004; *Simon-Miller et al*. 2005]. Equatorial latitudes between -3° and 3° are omitted in the CIRS profile because the thermal wind equation greatly amplifies the errors in temperature when latitude is small.

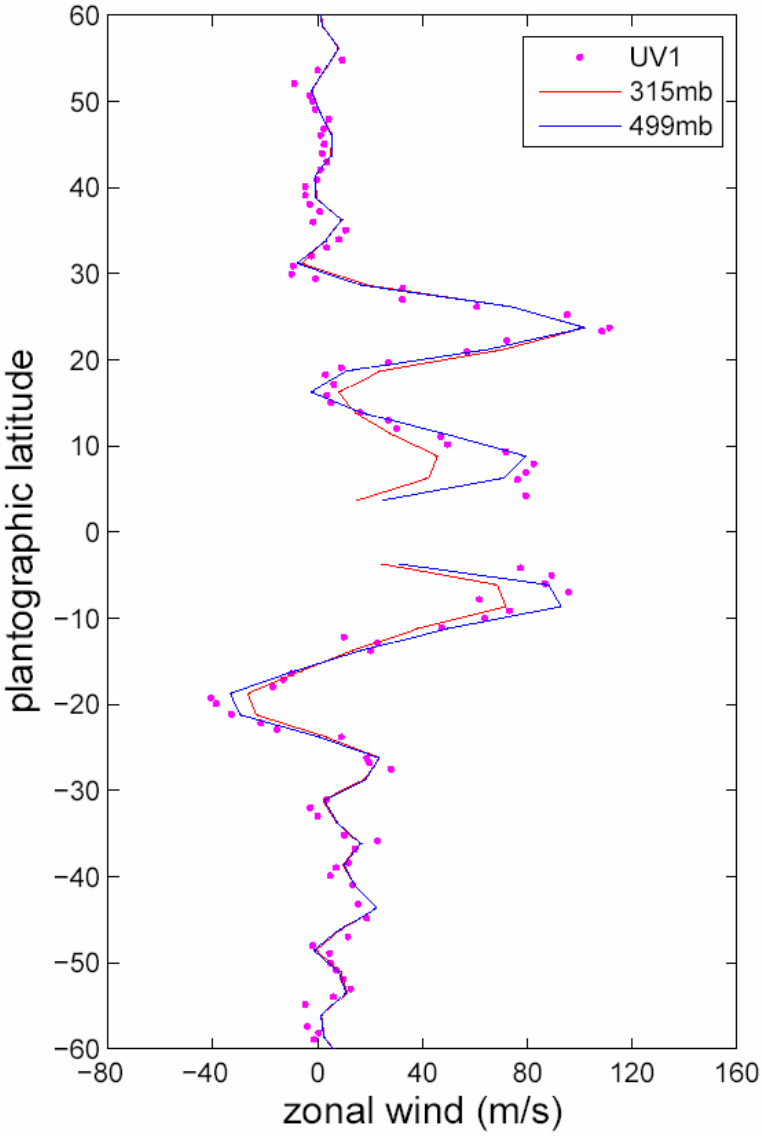

Figure 2.8 Time series of a deep cloud through a hot spot. **(A)** Time series of CB2 images separated by 10.5 hours. **(B)** Multi-filter images corresponding to the top panel of **(A)**. The MT3, MT2, CB2 images of group **(B)** are near-simultaneous images separated by 40 seconds. The mean value of every constant-latitude in MT3 images is removed so that these feature contrasts covered by the equatorial haze of MT3 can be seen.

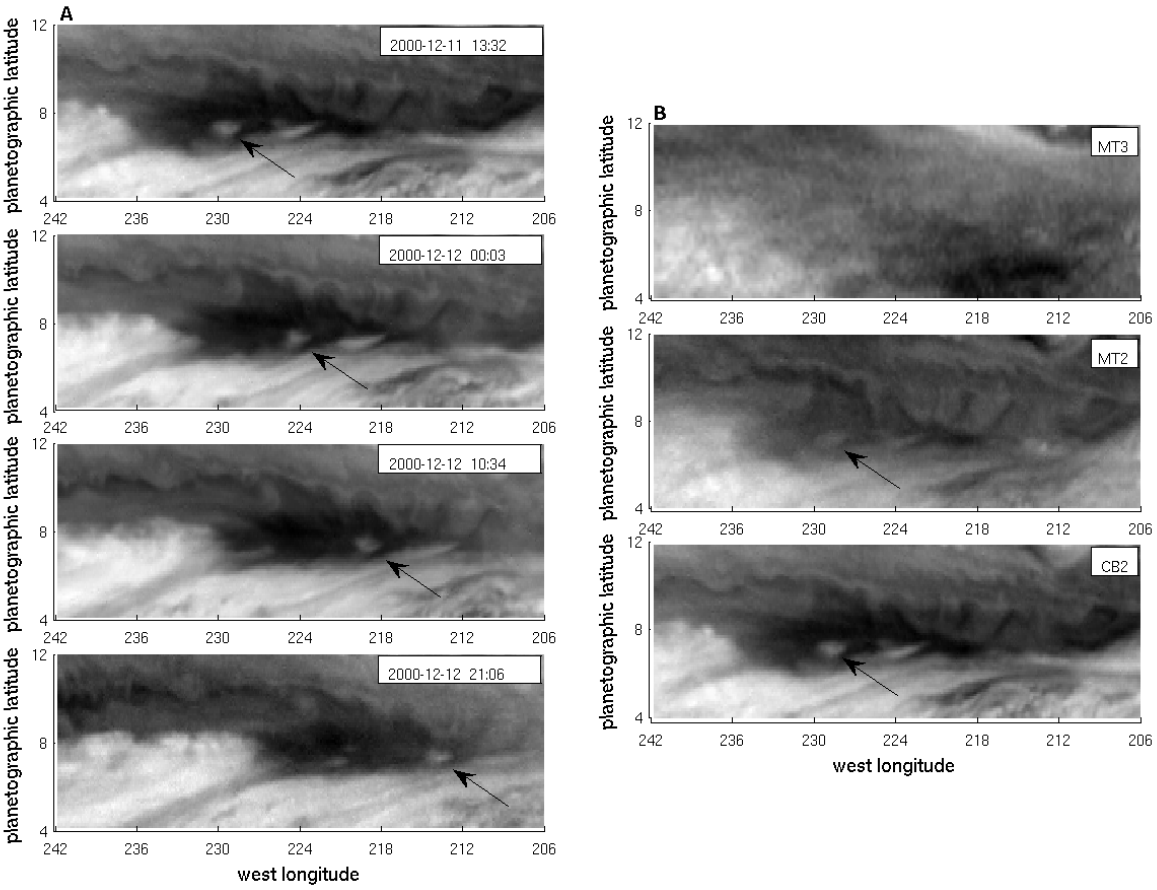

Figure 2.9 Comparison between the zonal winds by tracking features through hot spots, the zonal winds for all features in CB2 images, and the deep zonal winds from the Galileo probe [*Atkinson et al.*, 1998]. Each red circle without an error bar is the velocity of a deep feature that only can be tracked in a pair of images. Each red circle with an error bar is the velocity of a deep feature that is tracked in more than one pair of images, or the velocity of multiple measurements on different features at the same latitude. Error bars are calculated by the standard deviation of the multiple measurements at the same latitude. The CB2 zonal wind profile between latitudes 5° and 10°N is the same as the $CB2_a$ zonal wind in Fig.5 [*Porco et al.*, 2003]. The dashed line in the upper panel represents the latitude of Galileo probe. The results of the DWE on the Galileo probe [*Atkinson et al.*, 1998] are show in the bottom panel.

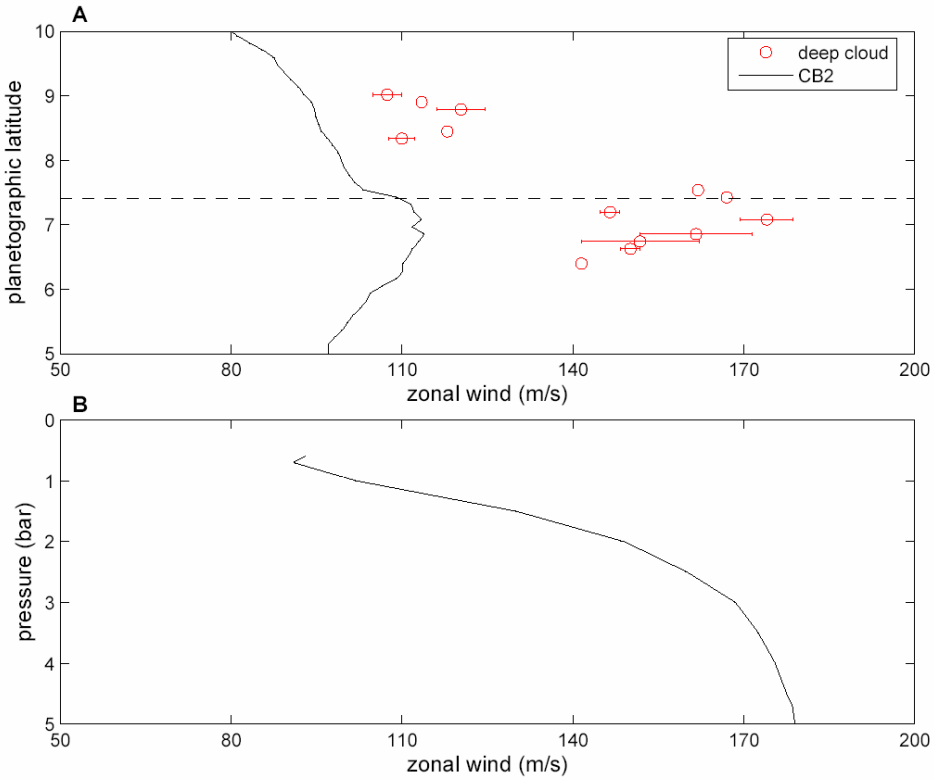

Chapter 3: Waves in Jupiter's Atmosphere Observed by the Cassini ISS and CIRS Instruments

3.1 Abstract

The Cassini Imaging Science Subsystem (ISS) and Composite Infrared Spectrometer (CIRS) reported a North Equatorial Belt (NEB) wave in Jupiter's atmosphere from optical images (Porco et al., 2003) and thermal maps (Flasar et al., 2004), respectively. The connection between the two waves remained uncertain because the two observations were not simultaneous. Here we report on simultaneous ISS images and CIRS thermal maps that confirm that the NEB wave shown in the ISS ultraviolet (UV1) and strong methane band (MT3) images is correlated with the thermal wave in the CIRS temperature maps, with low temperatures in the CIRS maps (upwelling) corresponding to dark regions in the UV1 images (UV-absorbing particles) and bright regions in the MT3 images (high clouds and haze). The long period of the NEB wave suggests that it is a planetary (Rossby) wave. The combined observations from the ISS and CIRS are utilized to discuss the vertical and meridional propagation of the NEB wave, which offers a possible explanation for why the NEB wave is confined to specific latitudes and altitudes. Further, the ISS UV1 images reveal a circumpolar wave centered at 48.5°S (planetocentric) and probably located in the stratosphere, as suggested by the ISS and CIRS observations. The simultaneous comparison between the ISS and CIRS also implies that the large dark oval in the polar stratosphere of Jupiter discovered in the ISS UV1 images (Porco et al., 2003) is the same feature as the warm regions at high northern latitudes in the CIRS 1-mbar temperature maps (Flasar et al., 2004). This comparison supports a previous suggestion that the dark oval in the ISS UV1 images is linked to auroral precipitation and heating (Porco et al., 2003).

3.2 Introduction

Atmospheric waves can serve as probes of atmospheric internal structures in the same way that seismic waves probe the internal structure of Earth (Flasar and Gierasch, 1986; Bosak and Ingersoll, 2002). Also, waves are important for transporting momentum, energy, molecules, and particles between different latitudes and altitudes. Their presence provides information about the forces that drive them. Among the giant planets, waves are discovered to be ubiquitous in the atmospheres from thermal fields and optical images (Magalhaes et al., 1989, 1990; Orton et al., Deming et al., 1989, 1997; Godfrey, Achterberg and Flasar, 1996; Godfrey, 1988; Sanchez-Lavega and Richard Hueso, 1998). For Jupiter, optical images have revealed wave patterns over a large range of spatial scales. Planetary waves with horizontal wavelength longer than 10,000 km were reported at high latitudes in Jupiter's stratosphere by the optical imaging system on Hubble Space Telescope (HST) (Sanchez-Lavega et al., 1998). At the same time, gravity waves with horizontal wavelength around 300 km were discovered in the planet's equatorial atmosphere in Voyager images (Flasar and Gierasch, 1986). Jupiter's horizontal thermal maps (Orton et al., 1991, 1994; Deming et al., 1997) and vertical temperature structure (French and Gierasch, 1974; Young et al., 2005) also revealed the large-scale planetary waves and meso-scale gravity waves. The equatorial 5 μm hot spots, which allow 5 μm thermal emission from deeper atmospheric level to escape due to their low cloud opacity, are observed in optical images (Allison, 1990), thermal maps (Ortiz et al., 1998; Orton et al., 1998), and numerical modeling (Showman and Dowling, 2000). The hot spots are interpreted as Jupiter's planetary waves in the above studies. For the other giant planets,

waves are also discovered to be ubiquitous in the atmospheres from thermal fields and optical images (Godfrey, 1988; Hinson and Magalhaes, 1991, 1993; Achterberg and Flasar, 1996).

More recently, the Cassini ISS discovered an obvious longitudinal wave in Jupiter between 10°N and 19°N latitude (planetocentic) from the ultraviolet (258 nm, UV1) and strong methane band (889 nm, MT3) images (Porco et al., 2003). Subsequently, the Cassini CIRS reported a thermal wave at the same latitude ranges from temperature maps (Flasar et al., 2004). Unfortunately, these two Cassini observations are not simultaneous so it was difficult to correlate the two waves and determine their relative phase. Some previous work (Magalhaes et al., 1989; Orton et al., 1994; Sanchez-Lavega et al., 1998) that tried to connect optical waves to the thermal waves suffered from the same problem. Fortunately, the Cassini ISS obtained multi-filter images of Jupiter (the ride-along data set) during the working time of the CIRS observations, which provide a good opportunity to study the correlation between the optical waves and thermal waves.

In this paper, we discuss the waves that were discovered by the ISS and CIRS. The wave between 10°N and 19°N latitude (planetocentic) is a Rossby wave. By comparing the phase speed of the wave with the local wind speed, we are able to identify a region in latitude-altitude space where the wave can propagate. At the boundaries of the region the wave is either absorbed or reflected. These studies help identify the regions where the wave is generated. The simultaneous observations are also used to connect the large dark

oval in the polar region discovered by the ISS UV1 images and the warm regions in the CIRS 1-mbar temperature maps.

The following section (Section II) is a description of the data sets used in this paper. Our observations of waves are discussed in Section III. Theoretical considerations are in Section IV. In Section V, we summarize our discussion in the context of previous observations. Planetocentric latitudes, System III west longitude, and positive velocity in the eastward direction are used in this paper.

3.3 Description of data sets and processing

Our observations are made using three data sets: 1) the continuous ISS multi-filter images acquired over the 45-day period October 1 to November 14, 2000, 2) the ISS ride-along imaging data set, which was taken during the working time of the CIRS regular observations over the 10-day period January 1-10, 2001, and 3) temperature maps constructed from the CIRS data taken at the same time as the ride-along imaging data set, January 1-10, 2001. The spatial resolution of the Cassini ISS images at the equator ranges from ~ 500 km/pixel at the beginning of October in 2000 to ~ 100 km/pixel at the beginning of January in 2001. The CIRS thermal maps have spatial resolution of ~ 1º in the latitudinal and longitudinal directions, which corresponds to ~ 1000 km in the tropical regions of Jupiter.

The ISS acquired high-quality time-lapse images in different filters during its lengthy 6-month (October 1, 2000 to March 22, 2001) Jupiter flyby. The ISS multi-filter imaging data sets before the middle of December of 2000 are fairly regular in time and space, which covered the jovian global disk once per one or two jovian rotations, i.e. once every 10h or 20h. The corresponding imaging strategy for these continuous images has been described elsewhere (Porco et al., 2003, 2005; Li et al., 2005). The phase angle between the spacecraft and Jupiter was 20 degrees at the beginning of the flyby (October 1, 2000). The spacecraft began a month-long sweep through a large range of phase angles after its phase angle passed through zero on December 14 of 2000 (Fig. 1).

The image navigation, map projections, and radiometric calibration for these ride-along images are the same as used for the continuous ISS images (Porco et al., 2003, 2005; Li et al., 2005). For photometric calibration, the classical Minnaert correction (Minnaert, 1941) does not work well for these ride-along images because the phase angle is large and the physical properties of the atmosphere depend strongly on latitude. Therefore, we adopt a more empirical approach to define the Minnaert correction factor f. One divides by this number to get the normalized brightness at zero incidence and phase angles.

$$f = (\cos i)^{k(\phi)} (\cos e)^{l(\phi)}, \qquad (1)$$

where i is the solar incidence angle and e is the emission angle. The indices $k(\phi)$ and $l(\phi)$ are set as functions of latitude ϕ. In order to maximize the feature contrast and minimize the seams, which appear when the neighboring images taken at different times

are put together to make global maps, we make k and l change independently even though it violates the reciprocity principle (Minnaert, 1941). Further, in the MT3 and UV1 images, we subtracted the mean brightness of every line of pixels, corresponding to lines of constant latitude in the map-projected images, to enhance the contrast of the small-scale features and reveal some features covered by the equatorial haze.

The CIRS team produced temperature maps with high vertical and horizontal resolution (Flasar et al., 2004a, 2004b). Some CIRS thermal maps at specific pressure-levels (400-mbar, 243-mbar, 4-mbar, and 1-mbar) at different times (January 1, 5, and 10, 2001) are utilized to make a simultaneous comparison with the ISS ride-along images in this paper.

3.4 Observations and analysis

3.4.1. Waves in the Cassini ISS multi-filter images

Figure 2 shows an example of cylindrical-projected global maps in different filters constructed from the continuous ISS multi-filter image set. The ISS continuous images were taken at intervals of 40 seconds for the three filters (UV1, MT3 and CB3), which makes the constructed global maps in the three filters shown in the Fig. 2 virtually simultaneous. The mean value of brightness in every constant-latitude line in the MT3 and UV1 images is removed so that the feature contrast covered by the equatorial haze in MT3 and UV1 can be seen. In the UV1 (258 nm) and MT3 (889 nm) global maps, the most conspicuous wave is observed between 10° and 19°N latitudes with a clear anti-

correlation between the UV1 and MT3 maps. The anti-correlation implies that this North Equatorial Belt (NEB) wave is composed of UV-absorbing small particles mixed with the high-altitude scattering haze, both of which absorb in the UV1 and scatter in the MT3. Also, the gases in the atmosphere absorb in the MT and scatter in the UV. The number of wavelengths in the planetary circumference for the NEB wave is 12-13, which corresponds to a wavelength of 34,000-37,000 km at 14.5°N. The quasi-periodic bright areas around 60°W, 120°W, 180°W, 240°W, and 300°W in the top and bottom boundaries of the MT3 global map (panel **B**) come from incomplete removal of limb darkening.

The so-called 5 μm hot spots revealed by the 5 μm thermal measurements are also observed by the Cassini ISS images at the visible bands and methane-absorption bands. The CB3 global map in Fig. 2 displays these hot spots, which are dark patches located in Jupiter's bright equatorial band. These hot spots are different from the NEB wave in the UV1 and MT3 global maps: First, they are located at a different latitude, and second, they have a different longitudinal pattern than the NEB wave. The MT3 global map of Fig. 2 shows both the NEB wave centered at 14.5°N and these hot spots centered at 5°N, which confirms that they are different phenomena. Previous studies show that the number of hot spots encircling the planet changed from 13 during the Voyager 1 encounter to 11 during the Voyager 2 encounter (Smith et al., 1979a, 1979b). The number decreased to 8-10 at the time of Cassini, as seen in the CB3 global map of Fig. 2.

Figure 2 shows that the NEB wave cannot be seen in the continuum band CB3 global map centered at 938 nm, even though that band is close in wavelength to the MT3 band at 889 nm. The NEB wave pattern shows clearly only in the UV1 and MT3 among the 9 filters of the Cassini ISS (Fig. 3). Some features seen in the other 7 filters may be related to features of the wave that are seen in the UV1 and MT3 filters (Porco et al., 2003), but the correlation is weak. We suggest two possibilities: One is that the NEB wave exists at the pressure levels sampled by the 7 filters, but the mechanism to produce contrast from the wave activity is weak there. The other is that the NEB wave does not exist at the altitudes sampled by the 7 filters. The effective pressure-levels (optical depth τ =1 in the absence of cloud opacity) in the UV1 and MT3 filters are 350-mbar and 600-mbar respectively (West et al., 2004; Li et al., 2005). These pressure-levels are higher in altitude than the effective pressure-levels in the other 7 filters. The cloud features seen in the continuum band images are estimated to be at a pressure-level ~ 0.7 bar (Banfield et al., 1998), so the second possibility would imply that the bottom of the NEB wave is above the 0.7 bar surface.

A circumpolar wave system centered at 48.5°S is seen in the UV1 global map of Fig. 2, but not in the other 8 filters of the ISS images. The polar-projected map of panel **A** of Fig. 2 is displayed in Fig. 4, which clearly shows that the wave encircles the polar region in the southern hemisphere. The stratospheric haze on Jupiter has significant opacity at UV wavelengths at high latitudes (Tomasko et al., 1986; West, 1988; Rages et al., 1999; West et al., 2004), which is probably due to auroral destruction of methane with subsequent ion and neutral chemistry (Hord et al., 1979; Pryor and Hord, 1991). In

addition, estimates of the pressure levels of high-latitude features in ultraviolet images (Banfield et al., 1996; Vincent et al., 2000) suggest that, at high latitudes, the ultraviolet filter mainly senses the stratosphere. The above discussion combined with the fact that the circumpolar wave only shows in the UV1 images suggests that it is probably located in the stratosphere. The number of wavelengths in the corresponding planetary circumference for the circumpolar wave is estimated to be 18-20, which corresponds to a wavelength of 15,000-17,000 km at 48.5°S.

Many circumpolar waves were observed in mid-latitudes of the northern hemisphere in the UV1 global map of Fig. 2 (Porco et al., 2003). These circumpolar waves in the northern hemisphere do not show in the other 8 filters of the Cassini ISS images either, which similarly suggests that these waves are located in the stratosphere. The chaotic appearance of these waves makes it difficult to measure their features.

The NEB wave and circumpolar mid-latitude wave approximately kept their wave-numbers during the period of the continuous ISS images set over 45 days (October 1 to November 15, 2000) with small changes in the brightness and shapes of wave crests and troughs. Phase velocities relative to System III are measured by choosing clear parts of the two waves and tracking the motions of the crests. Figure 5 shows the time series of the clear parts for the two waves in the UV1 filter. Panel **A** is for the NEB wave with the time separation 5 days, and panel **B** is for the circumpolar wave with the time separation 1.7 days. The figure shows that the NEB wave steadily moves to the west with a drift of 11° of longitude during a 40-day period and the circumpolar wave steadily moves to the

east with a drift of 8.5° of longitude during a 15-day period. The average phase velocities are calculated by averaging the movements of the three crests in the two waves, which are displayed in Fig. 6 as red dots with error-bars (panel **A** is for the NEB wave and panel **B** is for the circumpolar wave). The error-bars are estimated by the standard deviation of the velocities of the three crests. The two average phase velocities relative to System III are c_x = -3.9 m s^{-1} for the NEB wave and c_x = 4.2 m s^{-1} for the circumpolar wave. The wave periods relative to System III for the two waves are estimated as ~ 100 days for the NEB wave and ~50 days for the circumpolar wave by taking account of the corresponding zonal wavelength and phase velocity.

Figure 6 shows the ambient flows at the pressure levels of the UV1 filter (red line) and CB2 filter (green line) within the latitude ranges of the two waves. The velocities of the ambient flows in the UV1 filter come by tracking the small features unique to the UV1 images in the continuous ISS multi-filter image sets acquired over a 45-day period (Li et al., 2005). The small features are distinct from the wave itself, which has a larger scale. The comparison with the CIRS thermal wind suggests that the ambient flows from UV1 images are located at a pressure level of 0.5 bar (Li et al., 2005). The UV1 ambient flows outside equatorial regions are probably located at a higher altitude than 0.5 bar due to the increase of stratospheric opacity at high latitudes (Tomasko et al., 1985; West, 1988; Rages et al., 1999; West et al., 2004). The green line comes from an automatic-correlation measurement based on the time-lapse CB2 images in the ISS data set (Porco et al., 2003), which represents an ambient flow at the pressure level ~ 0.7 bar (Banfield et al., 1998). The phase velocities of the waves and the corresponding UV1 ambient flows

come from the same ISS UV1 image set over a 45-day period, which implies that the waves and the UV1 ambient flows are around the same pressure-level. Figure 6 shows that the two waves propagate westward relative to the UV1 flow at its altitude, although they propagate eastward relative to the CB2 flow at its altitude. Since the CB2 flow is at a lower altitude than the wave, this difference has important implications for wave propagation, which will be discussed in Sections IV.B and IV.C).

3.4.2 The NEB wave in ISS and CIRS images

The MT3 filter images during the ride-along imaging period (Jan 1 to Jan 10, 2001) are spaced in a regular pattern compared to the UV1 filter images, so we can make MT3 global maps during the period. Figure 7 shows a simultaneous comparison between an ISS MT3 global map and the CIRS global temperature field. Panel **A** is the CIRS 400-mbar global temperature field on 1 January 2001. The CIRS global temperature maps discussed in this paper are the actual retrieved temperatures at specific pressure levels (Flasar et al., 2004). Panel **B** is the ISS MT3 global map at the same time. Panel **C** is the same as Panel **B** except the mean value of every constant-latitude line was removed to increase the feature contrast. The simultaneous comparison displays a clear negative correlation between the ISS MT3 bright regions and the CIRS high temperatures for the NEB wave. It also suggests that the bright regions of the NEB wave in UV1 images are positively correlated with high temperatures in the CIRS maps because of the anti-correlation between the UV1 and MT3 for the NEB wave. The following near-simultaneous comparison between the ISS UV1 and CIRS (Fig. 8) confirms this point.

During the ride-along imaging period, the UV filter images are irregular in time and space and relatively scarce compared to the MT3 filter images. Therefore, we cannot make a whole UV1 global map during the period. Panel **B** in Fig. 8 shows a UV1 map from longitude 135° to 300°W and latitude 12°S to 69°N on 7 January 2001. Likewise, the mean value of every constant-latitude line is removed to increase the feature contrast. We do not have the CIRS temperature map at exactly the same time, so the CIRS 400-mbar temperature maps in January 5 (panel **A**) and January 10 (panel **C**) are used for the comparison in Fig. 8. All three CIRS 400-mbar thermal maps (January 1, 5 and 10, 2001) are put together (Fig. 9) to measure the movement of the NEB thermal wave. Figure 9 shows that most of these thermal features move to the west with a longitude displacement ~ 2° during the 10-day period, which is roughly consistent with the measurement by the continuous UV1 images (11° during the 40-day period). The 2° longitude displacement during the 10-day period is only a small fraction of the wavelength of the NEB wave, so the comparison between the ISS UV1 image and the CIRS maps in Fig. 8 can be regarded as near-simultaneous observations. Figure 8 displays a clear positive correlation for the NEB wave between the bright regions in the ISS UV1 map and the high temperatures in the CIRS thermal maps. In summary, the simultaneous comparison between the MT3 global map and the CIRS temperature field and the near-simultaneous comparison between the UV1 map and the CIRS thermal maps both suggest that the NEB wave appearing in the ISS images and the CIRS temperature field are parts of the same phenomenon. The low temperatures in the CIRS maps imply upward displacement of low-entropy air from below. The upward displacement is probably associated with these

UV-absorbing small particles either by bringing them up from below or forming them during the process of upward displacement.

Figure 10 shows CIRS thermal maps at four pressure levels – 400, 243, 4, and 1 mbar. The NEB wave is apparent at 400 and 243 mbar but not at the 4 or 1 mbar levels. The simplest interpretation is that the wave does not exist at the higher levels.

Ground-based observation (Orton et al., 1994) revealed waves in the temperature field (thermal waves) between 1980 and 1993, which are located around 13°N latitude and the 250-mbar pressure level with zonal wavelengths of order 40,000 to 70,000 km and phase velocity of –5.5 m s^{-1} relative to System III. Hubble Space Telescope (HST) wide field planetary camera 2 (WRPC2) observations taken between 1995 and 1996 in the visible wavelengths and methane bands (Simon-Miller et al., 2001) also showed a wave system with roughly the same wavelength and latitudes as the NEB wave in this paper. The similarity between the waves discovered by the previous observations and the NEB wave observed by Cassini during 2000-2001 suggests that the NEB wave is a recurring phenomenon or a long-lived system.

3.4.3 The circumpolar wave in ISS and CIRS images

No high-latitude UV1 images in the southern hemisphere of Jupiter are found from the ISS ride-along imaging data set during January 1-10, 2001, so we can not connect the circumpolar wave centered at 48.5°S to the CIRS thermal maps directly. However, these

CIRS temperature maps at different pressure levels (400-mbar, 243-mbar, 4-mbar, and 1-mbar) in January 1 of 2001, which is displayed in Fig. 10, do not show this wave pattern around 48.5°S. Therefore, the circumpolar wave centered at 48.5°S latitude probably exists in a pressure levels between 243-mbar and 4-mbar if we assume that the circumpolar wave lived through the first week of January in 2001.

3.4.4 The 65ºN oval in ISS and CIRS images

The ISS 2.5-month (October 1 to mid-December, 2000) UV1 movie displays a large dark oval centered at 65°N in Jupiter with the same size and shape as the Great Red Spot (Porco et al., 2003). Although this feature is not long-lived, a nearly identical feature had been seen in HST images taken in 1997 (West et al., 2004). The UV1 global map of Fig. 2 (panel **A**) shows a dark oval formed in the beginning of November in 2000 with position (65°N, 170°W), and is indicated by a white arrow. The dark oval does not show in the strong methane band (MT3) and the corresponding continuum band (CB3). This and the fact that the UV1 light cannot penetrate to the troposphere in the polar region due to the intense stratospheric haze (Tomasko et al., 1986; West, 1988; Rages et al., 1999; West et al., 2004), suggest that the dark oval is located in the stratosphere (Porco et al., 2003). The oval formed and grew from early October to mid-November, then elongated and died at the end of the 2.5-month period (Porco et al., 2003). Other observations suggest that large oval formation in the polar region is a recurring phenomenon (West et al., 2004). Panel **B** of Fig. 11 shows a new dark oval indicated by a white arrow, which is centered at 65°N and 180°W and formed on 8 January 2001 after the old large oval died

in the middle of December. The new dark oval implies that the polar oval is a recurring event. Flasar et al. (2003) also reported large warm regions in January of 2001 at the same latitude (65°N) in the CIRS 1-mbar temperature maps, but it is speculative to connect the CIRS warm regions to the UV1 dark oval in November of 2000 because the two observations are not simultaneous. Our UV1 maps in January 7 make it possible to study the correlation.

Figure 11 shows a near-simultaneous comparison between the 1-mbar CIRS temperature maps and the ISS UV map. Panel **B** of Fig. 11 is the same as panel **B** of Fig. 8, which is the UV1 map on 7 January 2001. Panel **A** and panel **C** are the CIRS 1-mbar temperature maps in January 5 and 10, respectively. Figure 11 suggests that the location and shape of the warm regions do not change much from January 5 to 10. The figure also shows that the dark oval in the UV map has the same location (65°N, 180°W) and oval shape as the warm regions in the CIRS temperature maps. This comparison suggests that the dark oval in the UV1 images is connected to the high-latitude warm regions in the CIRS temperature maps. This relation is opposite to the NEB wave, where dark regions in UV1 images are connected to cold temperatures in the CIRS thermal maps. There the explanation was that the upward displacement of low-entropy air, corresponding to low temperatures in the CIRS maps, brings these small UV-absorbing particles from below or helps to form them. The correlation between the dark oval in the UV1 images and the warm regions in the CIRS thermal maps suggests that auroral processes play an important role in heating the air and forming the particles (Porco et al., 2003). Downward displacement of high-entropy air might bring these UV-absorbing particles down from

above. The location of the new dark oval in January (65°N, 180°W) within the main auroral oval supports the connection between the dark oval and auroral process (Porco et al., 2003; Flasar et al. 2004). In addition, the warm regions shown in the CIRS 1-mabr temperature maps do not show in the CIRS 4-mbar temperature maps (Fig. 11), which suggests the dark oval in the UV1 images is probably located above the 4-mbar pressure surface. This conclusion is consistent with the previous inference from limb darkening observations, which also implies that the dark oval is at 1-mbar or higher (West, 1988; West et al., 2004).

However, the warm regions in the CIRS temperature maps (panel **A** and **C** of Fig. 11) are larger than the dark oval in the UV1 map (panel **B** of Fig. 11). Likewise, Figs. 7 and 8 also show that the NEB wave in the CIRS temperature maps is larger than the NEB wave in the UV1 and MT3 images. We do not have an explanation why the size difference exists between brightness features in the ISS images and the thermal features in the CIRS temperature maps.

3.5 Theoretical considerations

3.5.1 Gravity waves versus planetary waves

The low frequency (period ~ 100 days) suggests that these are planetary waves - they cannot be gravity waves or acoustic waves. If the NEB wave were a gravity wave, its frequency relative to the zonal flow $\bar{u}$ would be (Holton, 2004, p. 208)

$$(\nu - k\bar{u})^2 = f_0^{\,2} + \frac{N^2 K_h^{\,2}}{m^2} \qquad (2)$$

where ν is frequency, k is zonal wave-number, $\bar{u}$ is the ambient zonal wind, f_0 is the Coriolis parameter at the latitude of the NEB wave (14.5°N), N is the buoyancy (Brunt-Vaisala) frequency, K_h is the horizontal wave-number, and m is the vertical wave-number. The Coriolis parameter $f_0 = 9.1\times10^{-5}\,s^{-1}$ at the latitude 14.5°N. The term $k\bar{u}$ is much smaller than the Coriolis parameter f_0 for the NEB wave with $k = 1.77\times10^{-7}\,\mathrm{m}^{-1}$ and $\bar{u} < 50$ m s^{-1} at the latitude 14.5°N. Therefore $|\nu| > |f_0|$, implying a period shorter than 0.8 days, but this is inconsistent with the period of the NEB wave, which is ~100 days. Previous observations (French and Gierasch, 1974) also show that the period of jovian gravity waves in the upper atmosphere is less than 1 day. Therefore, we can rule out the gravity wave as the candidate of the NEB wave. The 48.5°S circumpolar wave can be ruled out as gravity wave for the same reason. Therefore, we think that the two waves (14.5°N wave and 48.5°S wave) are planetary waves.

3.5.2 Meridional trapping of the NEB wave

The NEB wave is observed between latitudes of 10° and 19°. We treat it as a planetary (Rossby) wave and ask if the wave is trapped within this band. With the data at hand, there are limitations to this analysis. Wave propagation and trapping depend on the zonal wind profile and static stability, and these are not precisely known at all the latitudes and altitudes of interest. Also, the vertical and horizontal structure of the wave is known at only a few latitudes and altitudes. Therefore a full-wave solution is not warranted, and we

use the Wentzel-Kramer-Brillouin (WKB) approximation instead. Further, we use the WKB approximation beyond its range of validity, which is when the wavelength is much less than the scale of variation of the medium in which it propagates. However as stated by Morse and Feshbach (1953, p. 1105), even when this condition is not satisfied, the WKB method is often a convenient starting point for further analysis.

Consistent with this approximation, we assume that the NEB wave has solutions of the form $\exp[(z/2H) + i(kx - c_x kt + \int mdz)]\cos(\int ldy)$. Substituting this into the equation for small-amplitude quasi-geostrophic planetary waves on a β-plane (e.g., Salby, 1996, p. 463), we obtain the following dispersion relation for the square of the meridional wavenumber;

$$l^2 = \frac{\beta_e}{\overline{u} - c_x} - \frac{f^2}{N^2}\left(m^2 + \frac{1}{4H^2}\right) - k^2 \qquad (3)$$

Quasi-geostrophic theory is valid here because the relative frequency $k(\overline{u} - c_x)$ is much smaller than f at the latitude of the NEB wave (14.5°N).

If l^2 is positive within a specfic latitude range and negative outside that range, then the wave may be trapped within that range. Trapping therefore depends not only on the properties of the wave like m^2, k^2, and c_x, but also on the properties of the medium like β_e, $\overline{u}$, N^2, H^2, and f^2. Here β_e is the meridional gradient of zonal-mean vorticity, and H is

the scale height. Other variables have been defined in Eq. (2). In a zonal-mean flow $\overline{u}(y,z)$, β_e is defined by (Salby, 1996, p. 465):

$$\beta_e = \beta - \frac{\partial^2 \overline{u}}{\partial y^2} - \frac{1}{\overline{\rho}} \frac{\partial}{\partial z}\left(\overline{\rho} \frac{{f_0}^2}{N^2} \frac{\partial \overline{u}}{\partial z} \right) = \beta + \beta_y + \beta_z , \qquad (4)$$

The meridional gradient of zonal-mean vorticity β_e is composed of three parts: the gradient of the planetary vorticity $\beta = \partial f / \partial y$, the vorticity gradient associated with the curvature of the ambient flows in the meridional direction $\beta_y = -\partial^2 \overline{u} / \partial y^2$, and the term associated with vertical shear of the ambient flows $\beta_z = -(1/\overline{\rho})(\partial/\partial z)\left[(\overline{\rho} f^2 / N^2)(\partial \overline{u}/\partial z)\right]$. The vertical coordinate z in β_z is defined as $z = -H \ln(p/p_0)$ in the log-pressure coordinates, where H is the reference scale height and p_0 is a reference pressure, e.g., one bar.

The estimation of β_e depends on the meridional and vertical structure of the zonal wind $\overline{u}(y,z)$, which we obtain from the CIRS data. We assume that the NEB wave is located around the 400-mbar and 243-mbar levels based on the observations that the wave shows there but not at the 4-mbar and 1-mbar levels (Fig. 10). We use the CIRS 315-mbar zonal winds, which are near the middle of the two pressure-levels (400-mbar and 243-mbar). The first term β has the value $4.9 \times 10^{-12} s^{-1} m^{-1}$ at 14.5°N and changes smoothly with latitude (panel **B** of Fig. 12). We estimate β_y by fitting the CIRS 315-mbar zonal wind with two cosine functions and calculating β_y based on that function. Figure 12 shows the

result (panel **A**) and the corresponding β_y (panel **B**). Assuming that N^2 is constant and combining with the thermal wind equation, we can re-write the third term β_z of Eq. (4) in the form

$$\beta_z = \frac{gf}{TN^2}\left[\frac{\partial^2 T}{\partial z \partial y} - \left(\frac{1}{H} + \frac{1}{T}\frac{\partial T}{\partial z}\right)\frac{\partial T}{\partial y}\right] \tag{5}$$

Therefore, the third term β_z can be estimated from the CIRS temperature fields with relatively higher spatial resolution (~ 1° latitude) compared to the CIRS zonal winds fields (~2.2° latitude). We approximate $\partial^2 T/\partial z \partial y$, $\partial T/\partial y$, and $\partial T/\partial z$ at 315-mbar by $(1/\Delta z)\left[(\partial T/\partial y)_{243} - (\partial T/\partial y)_{400}\right]$, $(1/2)\left[(\partial T/\partial y)_{243} + (\partial T/\partial y)_{400}\right]$, and $(1/\Delta z)\left(T_{243} - T_{400}\right)$, respectively. The meridional gradients of temperature $(\partial T/\partial y)_{243}$ and $(\partial T/\partial y)_{400}$ are estimated by a central-difference scheme of the first derivative and the CIRS thermal maps at 243-mbar and 400-mbar pressure-levels. The estimation of β_z by this method is shown in the panel **B** of Fig. 12. In addition, the frequency N^2 in Eq. (3) is defined as $N^2 = g\,\partial \ln\theta/\partial z$, which we estimate using the CIRS average potential temperature θ at the two pressure-levels (243-mbar and 400-mbar). The resulting expression is $N^2 = g/(0.5\overline{\theta}_{243} + 0.5\overline{\theta}_{400})\left[(\overline{\theta}_{243} - \overline{\theta}_{400})/\Delta z\right] = 3\times10^{-4}\,s^{-2}$ for 315-mbar, which is consistent with the value in Voyager times (Achterberg and Ingersoll, 1989). The scale height $H = R\overline{T}/g$ is calculated to be $1.8\times10^4\,m$ at the 315-mbar by setting the $\overline{T}$ as the average

temperature of the 400-mbar and 243-mbar pressure-levels. Figure 12 (panel **B**) shows β_e within the latitude range [5ºN, 25ºN].

Figure 10 shows that the NEB wave appears in both CIRS 400-mbar and 243-mbar maps without obvious phase shift. In addition, Figs. 2 and 3 suggest that the NEB wave penetrates down at least to the pressure level of the UV1 filter, which is around 0.5 bar (Li et al., 2005). Therefore, the half-wavelength of the NEB wave is larger than the altitude difference between the 243-mbar and 500-mbar levels, which means that the vertical wavelength of the NEB wave is larger than 1 scale height.

In the WKB approximation, the meridionally trapped wave has to satisfy $\int_{y_1}^{y_2} l(y)dy = (n+1/2)\pi$ (Morse and Feshbach, 1953, pp. 1099-1099), where y_1 and y_2 are the turning points – the meridional boundaries of the trapping region – the latitudes where $l^2 = 0$. Since the wave appears to have only a single maximum in latitude, the number n is set to 1 in our case although this violates the condition of the WKB method. Evaluating the meridional wave-number $l(y)$ with Eq. (3) for different values of the vertical wave-number m, we find that the condition $\int_{y_1}^{y_2} l(y)dy = (3/2)\pi$ is satisfied when $m = 0.39\times10^{-4}\,\mathrm{m}^{-1}$, corresponding to a vertical wave-length 160 km. This is around 9 scale heights at the 315-mbar level, which is at least consistent with the previous conclusion that the vertical wavelength of the NEB wave is larger than 1 scale height. We also tried larger values of the meridional mode number n ($n = 2,3,4,\cdots$), but the condition $\int_{y_1}^{y_2} l(y)dy = (n+1/2)\pi$ could only be satisfied with negative m^2. The

trapping latitude range in that case is larger than 30 degrees (i.e., the lower turning point y_1 < 0º and the polar turning point y_2 > 30ºN), which is inconsistent with the observational trapping latitude range ~ 9 degrees (y_1 ~ 10ºN and y_2 ~ 19ºN).

Figure 13 shows l^2 as a function of latitude at the 315 mbar level, assuming m is constant with latitude and equal to 0.39×10^{-4} m^{-1}, the value that satisfies $\int_{y_1}^{y_2} l(y)dy = (3/2)\pi$. In general, m could vary with latitude and altitude. In a full treatment using the WKB approximation, one would launch rays in various directions from various locations and compute m^2 and l^2 along the ray path. Such detailed calculations are not justified in our case, first because we have almost no information about m, and second because the WKB approximation is not valid for small m and l. Figure 13 and the equation $\int_{y_1}^{y_2} l(y)dy = (3/2)\pi$ are useful only as a guide to show that trapping is possible within the latitude band centered around 14.5°N.

Figure 13 shows that l^2 becomes negative when moving away from the latitude of the NEB wave (14.5°N): The wave is trapped within this range by reflections at the latitude boundaries (Salby, 1996, p. 465). The reversal of the sign of l^2 around 12.5°N and 24°N is mainly due to the increasing eastward wind $\bar{u}$ when moving away from the latitude of the NEB wave (14.5°N). This makes the term $\beta_e/(\bar{u} - c_x)$ in Eq. (3) very small and offers a possible trapping mechanism in the meridional direction. Figure 13 suggests that the trapping is not complete at the lower latitude: Wave energy could leak out to the south, since the region of negative l^2 is neither deep nor wide.

Although the preceding analysis does imply qualitatively that the wave is trapped near 14.5°, the latitudes at which l^2 changes sign (12.5°N and 24°N) do not agree quantitatively with the observed boundaries of the wave (10°N and 19°N). In addition, uncertainties exist in the estimation of β_e and the vertical wave-number m. Detailed discussion of the propagation of the NEB wave has to involve a full wave analysis, but the theory will introduce more unknown parameters like the initial conditions. Such analysis is beyond the scope of this paper.

3.5.3 Vertical propagation of the NEB wave

When the zonal wind varies with height, the wave may encounter a *critical level*, which is defined as a level where $\overline{u} - c_x = 0$. The classical theory (Salby, 1996) says that $m \to \infty$ at the critical level and the wave is absorbed. Figure 6 shows that the phase velocity of the NEB wave is smaller than the UV1 ambient flow at ~ 0.5 bar (Li et al., 2005) and larger than the corresponding CB2 ambient flow at ~ 0.7 bar (Banfield et al., 1998). Figure 14 verifies this point again by comparing the phase velocity with the CIRS zonal winds at 315-mbar and 499-mbar. These facts suggest that the phase velocity of the NEB wave will be equal to the ambient flow ($\overline{u} - c_x = 0$) somewhere between the pressure-level ~ 0.5 bar and the pressure-level ~ 0.7 bar. Therefore, the NEB wave will be absorbed between 0.5 bar and 0.7 bar when its perturbation energy propagates downward. This conclusion seems to support the second explanation for why the wave is not seen clearly in the other 7 filters of the ISS (Figs. 2 and 3) — it does not exist at the

pressure-levels sampled by these filters. The vertical structure of the zonal winds from CIRS (Flasar et al., 2004; Simon-Miller et al., 2006) shows that the wind at 14.5°N is westward relative to the wave at 0.7 bar (CB2), changes sign near 499-mbar, is eastward at 315-mbar, changes sign again near 4-mbar, and finally becomes westward at 1-mbar. This suggests that the NEB wave can propagate between the 499 and 4 mbar levels and will be absorbed around the pressure-level ~ 4-mbar. The analysis is consistent with the CIRS observations that the NEB wave is seen in the 243-mbar and 400-mbar temperature maps, but not seen in the 1-mbar and 4-mbar temperature maps (Fig. 10).

3.5.4 Generating mechanism of the NEB wave

The property that the NEB wave is quasi-stationary relative to System III suggests that it is deep-rooted, although it cannot be seen in the continuum band images, which are sensitive to the deep jovian atmosphere. In addition, the NEB wave cannot propagate up from below through the critical level, since $\bar{u} - c_x = 0$ between the pressure-level ~ 0.5 bar and the pressure-level ~ 0.7 bar. Either the wave is generated between 0.5 bar and 4 mbar, or else it propagates in from the sides, having been generated below and to the north or south of 14.5°N latitude. Moist convective storms are always active in the 6°-15°N cyclonic regions (Little et al., 1999; Porco et al., 2003). Some strong convective storms can penetrate to altitudes above the 0.5-bar level (Li et al., 2005). The dynamical disturbance and the corresponding heating associated with these convective storms could be a generating mechanism for the NEB wave if we assume it is generated between 0.5 bar and 4 mbar.

Likewise, the circumpolar wave at 48.5°S could not be seen in the continuum band images, which suggests that it is generated in the upper troposphere or stratosphere. Some long-lived vortices are located at the latitudes of the circumpolar wave. An example of such vortices is shown in the global MT3 and CB3 maps of Fig. 2 with location at 48.5°S, 355°W. Flow disturbance above these vortices could create an obstacle in the flow that gives rise to the high-altitude circumpolar waves including the wave centered at 48.5°S. Furthermore, the upward momentum transportation associated with breaking or dissipation of small-scale gravity waves could be the origin of planetary waves in the upper atmosphere (Smith, 2003).

In general, Kelvin-Helmholtz (KH) instability due to strong wind shear can serve as a mechanism to generate atmospheric waves. Bosak and Ingersoll (2002) show that such instability can occur in the lower troposphere around 5-10 bar but not in the upper troposphere because the Richardson number is larger than 1.0 due to the large static stability there. In addition, Bosak and Ingersoll (2002) show that the waves due to KH instability have horizontal wavelength on the order of 300 km, which is several times the thickness of the shear layer. This is much smaller than the wavelengths of the NEB wave and the circumpolar wave in this study. Therefore, the KH instability can be ruled out as a generating mechanism for the two waves in this study.

The third possible generating mechanism is baroclinic instability. Achterberg and Flasar (1996) suggested that a changing potential vorticity gradient can be a source of planetary

waves in Saturn's upper troposphere. Our estimation of the potential vorticity gradient (β_e in Fig. 12) shows that the gradient is always positive within the latitude range of the NEB wave at the 315-mbar pressure-level, which suggests that the ambient flows are stable at the 315-mbar pressure-level. However, there are uncertainties in our estimates of the potential vorticity gradient β_e as we discussed in section *IV.B*. Here we assume that the deeper visible cloud deck (~ 0.7 bar) has the same value of β_z as the 315-mbar pressure-level and calculate the potential vorticity gradient β_e at the visible cloud deck based on the CB2 zonal wind measurements. The resulting β_e at the pressure-level of the visible cloud deck is shown in Fig. 15. Figure 15 shows that the potential vorticity gradient β_e is negative around the center of the NEB wave (latitude 14.5ºN) at the visible cloud deck (~ 0.7 bar), which is the result of the increasing curvature of the eastward jets when going deeper. Therefore, the baroclinic instability could be a candidate of the source of the NEB wave.

3.6 Summary and discussion

One NEB wave and one circumpolar wave were observed in the ISS multi-filter images. Their properties (wavelength, period, and movement relative to the ambient flows) suggest that the two waves are planetary waves. The simultaneous comparison between the ISS and CIRS (Porco et al., 2003; Flasar et al., 2004) confirms that the waves seen by the two instruments are the same. Furthermore, the combined observations from the ISS and CIRS offer a possible explanation of why the NEB wave is trapped in the vertical and meridional directions.

The near-simultaneous comparison between the ISS and CIRS observations connects the large dark oval in polar region in the UV1 images to the warm regions in the CIRS thermal maps. The large oval is dark in UV1 and warm in the CIRS, which suggests that it is composed of UV-absorbing particles transported down from above. In addition, the CIRS thermal maps suggest that the UV1 dark oval is located above the 4-mbar pressure surface.

Sanchez-Lavega et al.(1998) noticed that Jupiter's 67°S circumpolar waves (wavelength 15,000 km) and Saturn's hexagon at 79°N have an interesting relationship between the numbers n of wavelengths in the corresponding planetary circumference: $n(67^0 S)/n(79^0 N) \approx \cos(67^0)/\cos(79^0)$, The circumpolar wave system centered at 48.5°S in this study and the 67°S wave discovered by Sanchez-Lavega and Hueso (1998) have the same relationship: $n(48.5^0 S)/n(67^0 S) \approx \cos(48.5^0)/\cos(67^0)$. In other words, the two circumpolar waves on Jupiter have the same wavelength because the radius is proportional to cosine of the latitude. The two waves share other properties. Firstly, they are both quasi-stationary relative to the System III (phase velocity 4 m s^{-1} for the 48.5°S wave and 2 m s^{-1} for the 67°S wave). Secondly, the CIRS polar stratospheric zonal winds (Simon-Mille et al., 2006) based on the thermal wind equation and the CIRS thermal maps suggest that the 67°S circumpolar wave is embedded in the stratospheric eastward jets, which is same with the 48.5°S wave in this paper. As we discussed in the section *IV.D,* the negative β_y due to the eastward jets can change the sign of the potential

vorticity gradient β_e, which offers a possible source not only for the NEB wave but also for the circumpolar waves.

3.7 Reference

Achterberg, R.K., Ingersoll, A.P., 1989. A normal-mode approach to jovian atmospheric dynamics. J. Atmos. Sci. 46, 2448-2462.

Achterberg, R.K., Flasar, F.M., 1996. Planetary-scale thermal waves in Saturn's upper troposphere. Icarus 119, 350-369.

Allison, M.D., 1990. Planetary waves in Jupiter's equatorial atmosphere. Icarus 83, 282-307.

Banfield, D., Gierasch, P.J., Squyres, S.W., Nicholson, P.D., Conrath, B.J., Matthews, K., 1996. 2 um spectrophotometry of Jovian stratospheric aerosols - Scattering opacities, vertical distributions, and wind speeds. Icarus 121, 389-410.

Banfield, D., Gierasch, P.J., Bell, M., Ustinov, E., Ingersoll, A.P., Vasavada, A.R., West, R.A., Belton, M.J.S., 1998. Jupiter's cloud structure from Galileo imaging data. Icarus 135, 230-250.

Deming, D., Reuter, D., Jennings, D., Bjoraker, G., McCabe, G., Fast, K., Wiedemann, G., 1997. Observations and analysis of longitudinal thermal waves on Jupiter. Icarus 126, 301-312.

Flasar, F.M., Gierasch, P.J., 1986. Mesoscale waves as a probe of Jupiter's deep atmosphere. J. Atmos. Sci. 43, 2683-2707.

Flasar, F.M., Kunde, V.G., Achterberg, R.K., Conrath, B.J., Simon-Miller, A.A., Nixon, C.A., Gierasch, P.J., Romani, P.N., Bezard, B., Irwin, P., Bjoraker, G.L., Brasunas, J.C., Jennings, D.E., Pearl, J.C., Smith, M.D., Orton, G.S., Spilker, L.J., Carlson, R., Calcutt, S.B., Read, P.L., Taylor, F.W., Parrish, P., Barucci, A., Courtin, R., Coustenis, A., Gautier, D., Lellouch, E., Marten, A., Prange, R., Biraud, Y., Fouchet, T., Ferrari, C., Owen, T.C., Abbas, M.M., Samuelson, R.E., Raulin, F., Ade, P., Cesarsky, C.J., Grossman, K.U., Coradini, A., 2004. An intense stratospheric jet on Jupiter. Nature 427, 132-135.

Flasar, F.M., 45 colleagues, 2004. Exploring the Saturn system in the thermal infrared: The Composite Infrared Spectrometer. Space Science Reviews 115,169-297.

French, R.G., Gierasch, P.J., 1974. Waves in the jovian upper atmosphere. J. Atmos. Sci. 31, 1707-1712.

Gill, A.E., 1982. Atmosphere-Ocean Dynamics. Academic Press.

Godfrey, D.A., 1988. A hexagonal feature around Saturn's north pole. Icarus 76, 335-356.

Hinson, D.P., Magalhaes, J.A., 1991. Equatorial waves in the stratosphere of Uranus. Icarus 94, 64-91.

Hinson, D.P., Magalhaes, J.A., 1993. Inertio-gravity waves in the atmosphere of Neptune. Icarus 105, 142-161.

Holton, J.R., 2004. Introduction to Dynamic Meteorology, 4rd edition. Academic Press.

Hord, C.W., West, R.A., Simmons, K.E., Coffeen, D.L., Sato, M., Lane, A.L., Bergstralh, J.T., 1979. Photometric observations of Jupiter at 2400 angstroms. Science 206, 956-959.

Li, L., Ingersoll, A.P., Vasavada, A.R., Simon-Miller, A.A., Del Genio, A.D., Ewald, S.P., Porco, C.C., West, R.A., 2006. Vertical wind shear on Jupiter from Cassini images. J. Geophys. Res. in press.

Little, B., Anger, C.D., Ingersoll, A.P., Vasavada, A.R., Senske, D.A., Breneman, H.H., Borucki, W.J., the Galileo SSI Team, 1999. Galileo images of lightning on Jupiter. Icarus 142, 306-323.

Magalhaes, J.A., Weir, A.L., Conrath, B.J., Gierasch, P.J., Leroy, S.S., 1989. Slowly moving thermal features on Jupiter. Nature 337, 444-447.

Minnaert, M., 1941. The reciprocity principle in lunar photometry. Astrophys. J., 93, 403-410.

Morse, P.M., Feshbach, H., 1953. Methods of Theoretical Physics, part II. McGRAW-HILL BOOK COMPANY, INC.

Ortiz, J.L., Orton, G.S., Friedson, A.J., Stewart, S.T, Fisher, B.M., Spencer, J.R., 1998. Evolution and persistence of 5-um hot spots at the Galileo probe entry latitude. J. Geophys. Res. 103, 23051-23069.

Orton, G.S., Friedson, A.J., Caldwell, J., Hammel, H.B., Baines, K.H., Bergstralh, J.T., Martin, T.Z., Malcolm, M.E., West, R.A., Golisch, W.F., Griep, D.M., Kaminski, C.D., Tokunaga, A.T., Baron, R., Shure, M., 1991. Thermal maps of Jupiter: Spatial organization and time dependence of stratospheric temperature, 1980 to 1990. Science 252, 537-542.

Orton, G.S., 18 colleagues, 1994. Spatial organization and time dependence of Jupiter's tropospheric temperatures, 1980-1993. Science 265, 625-631.

Orton, G.S., 16 colleagues, Characteristics of the Galileo probe entry site from Earth-based remote sensing observations. J. Geophys. Res. 103, 22791-22814.

Porco, C.C., West, R.A., McEwen, A., Del Genio, A.D., Ingersoll, A.P., Thomas, P., Squyres, S., Dones, L., Murray, C.D., Johnson, T.V., Burns, J.A., Brahic, A., Neukum, G., Veverka, J., Barbara, J.M., Denk, T., Evans, M., Ferrier, J.J., Geissler, P., Helfenstein, P., Roatsch, T., Throop, H., Tiscareno, M., Vasavada, A.R., 2003. Cassini imaging of Jupiter's atmosphere, satellites, and rings. Science 299, 1541-1547.

Porco, C.C., West, R.A., Squyres, S., McEwen, A., Thomas, P., Murray, C.D., Delgenio, A., Ingersoll, A.P., Johnson, T.V., Neukum, G., Veverka, J., Dones, L., Brahic, A., Burns, J.A., Haemmerle, V., Knowles, B., Dawson, D., Roatsch, T., Beurle, K., Owen, W., 2004. Cassini Imaging Science: Instrument characteristics and anticipated scientific investigations at Saturn. Space Science Reviews 115 (1-4), 363-497.

Pryor, W.R., Hord, C.W., 1991. A study of photopolarimeter system UV absorption data on Jupiter, Saturn, and Neptune: Implications for auroral haze formation. Icarus 91, 161-172.

Rages, K., Beebe, R., Senske, D., 1999. Jovian stratospheric hazes: The high phase angle view from Galileo. Icarus 139, 211-226.

Salby, M.L, 1996. Fundamentals of atmospheric dynamics. Academic Press.

Sanchez-Lavega, A., Hueso, R, Acarreta, J.R., 1998. A system of circumpolar waves in Jupiter’s stratosphere. Geophys. Res. Lett. 25, 4043-4046.

Showman, A.P., Dowling, T.E., 2000. Nonlinear simulations of Jupiter's 5-micro hot spots. Science 289, 1737-1740.

Simon-Miller, A.A., Banfield, D., Gierasch, P.J., 2001. An HST study of jovian chromophores. Icarus 149, 94-106.

Simon-Miller, A.A., Conrath, B.J., Gierasch, P.J., Orton, G.S., Achterberg, R.K., Flasar, F.M., Fischer, B.M., 2006. Jupiter's atmospheric temperatures: from Voyager IRIS to Cassini CIRS, Icarus 180, 98-112.

Smith, A.K., 2003. The origin of stationary planetary waves in the upper mesosphere. J. Atmos. Sci. 60, 3033-3041.

Sromovsky, L.A., Revercomb, H.E., Krauss, R.J., Suomi, V.E., 1983. Voyager 2 observations of Saturn's northern mid-latitude cloud features: Morphology, motions and evolution. J. Geophys. Res. 88, 8650-8666.

Tomasko, M.G., Karkoschka, E., Martinek, S., 1986. Observations of the limb darkening of Jupiter at ultraviolet wavelengths and constraints on the properties and distribution of stratospheric aerosols. Icarus 65, 128-243.

Vincent, M.B., Clarke, J.T., Ballester, G.E., Harris, W.M., West, R.A., Trauger, J.T., Evans, R.W., Stapelfeldt, K.R., Crisp, D., Burrows, C.J., Gallagher, J.S., Griffiths, R.E.,

Hester, J., Hoessel, J.G., Holtzman, J.A., Mould, J.R., Scowen, P.A., Watson, A.M., Westphal, J.A., 2000. Jupiter's polar regions in the ultraviolet as imaged by HST/WFPC2: Auroral-aligned features and zonal motions. Icarus 143, 205-222.

West, R.A, 1988. Voyager 2 imaging eclipse observations of the jovian high altitude haze. Icarus 75, 381-398.

West, R.A., Baines, K.H., Friedson, A.J., Banfield, D., Ragent, B., Taylor, F.W., 2004. Jupiter: The Planet, Satellites and Magnetosphere. Cambridge Planetary Science, edited by Bagenal, F., Dowling, T.E., McKinnon, W.B., Jewitt, D., Murray, C., Bell, J., Lorenz, R., Nimmo, F..

Figure 3.1 Phase angle during the Cassini Jupiter flyby. The Jupiter flyby observation began in October 1 of 2000 and ended in March 22 of 2001. The phase angle decreased to minimal value (1 degree) in December 14 of 2000. Irregular blanks during the series of dots indicate no ISS or CIRS data in the corresponding time. The maximal period of missing data is from December 19 to 29 in 2000.

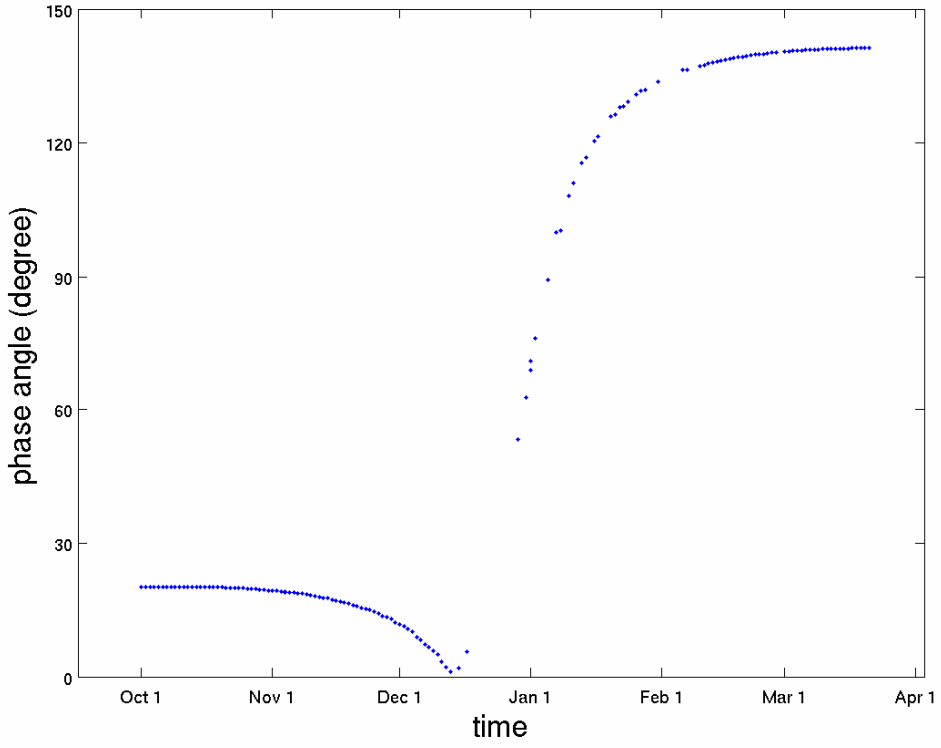

Figure 3.2 Cylindrical-projected ISS global maps in multi-filter filters. The ISS images used in the three global maps were taken on 1 November 2000 with intervals of 40 seconds between the three filters (UV1, MT3, and CB3). The mean brightness of every line of pixels in the MT3 and UV1 images is removed so that the feature contrast covered by the equatorial haze in MT3 and UV1 can be seen. Note that the quasi-periodic bright areas around 60°W, 120°W, 180°W, 240°W, and 300°W in the top and bottom boundaries of the MT3 global map are not real features. They mainly come from incomplete photometric calibration due to high incidence and emission angles in polar region.

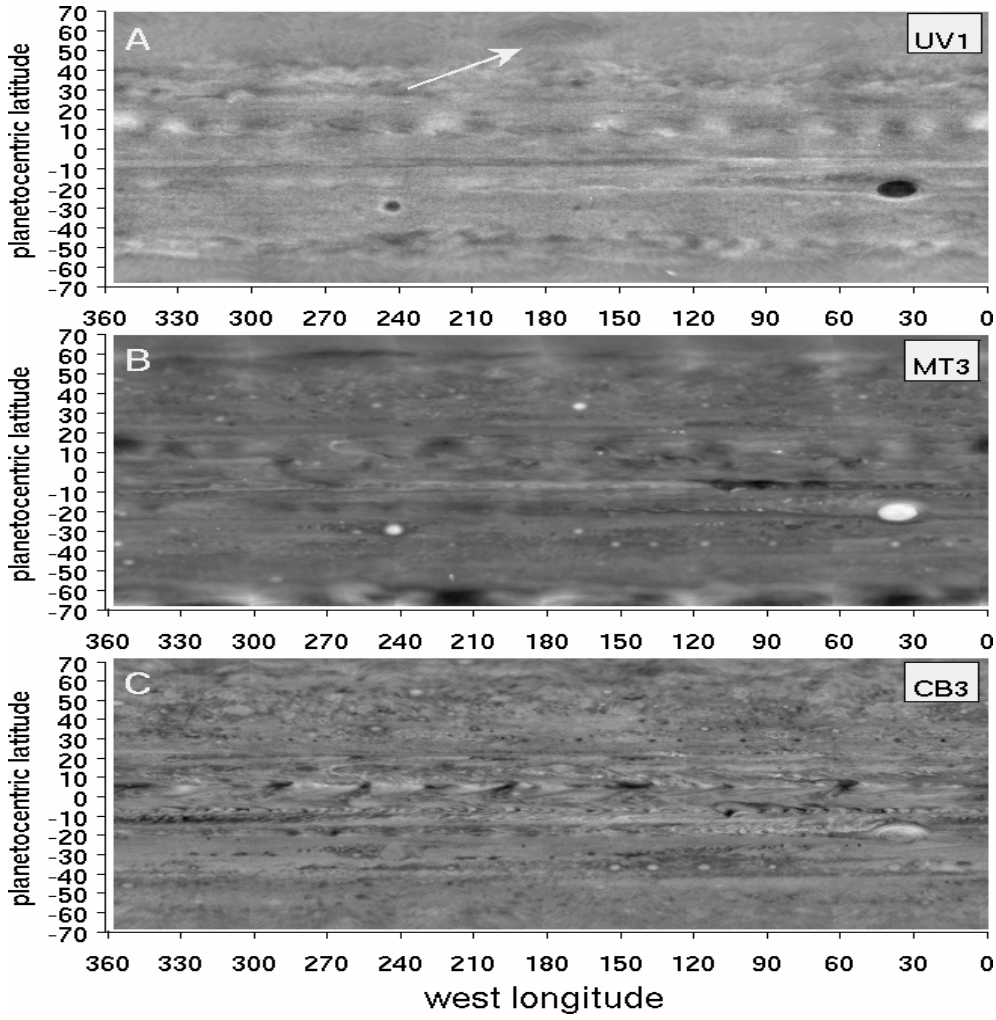

Figure 3.3 Cylindrical-projected ISS maps of the NEB waves in nine filters. The images were taken on 1 November 2000 with intervals of 40 seconds, which makes them virtually simultaneous.

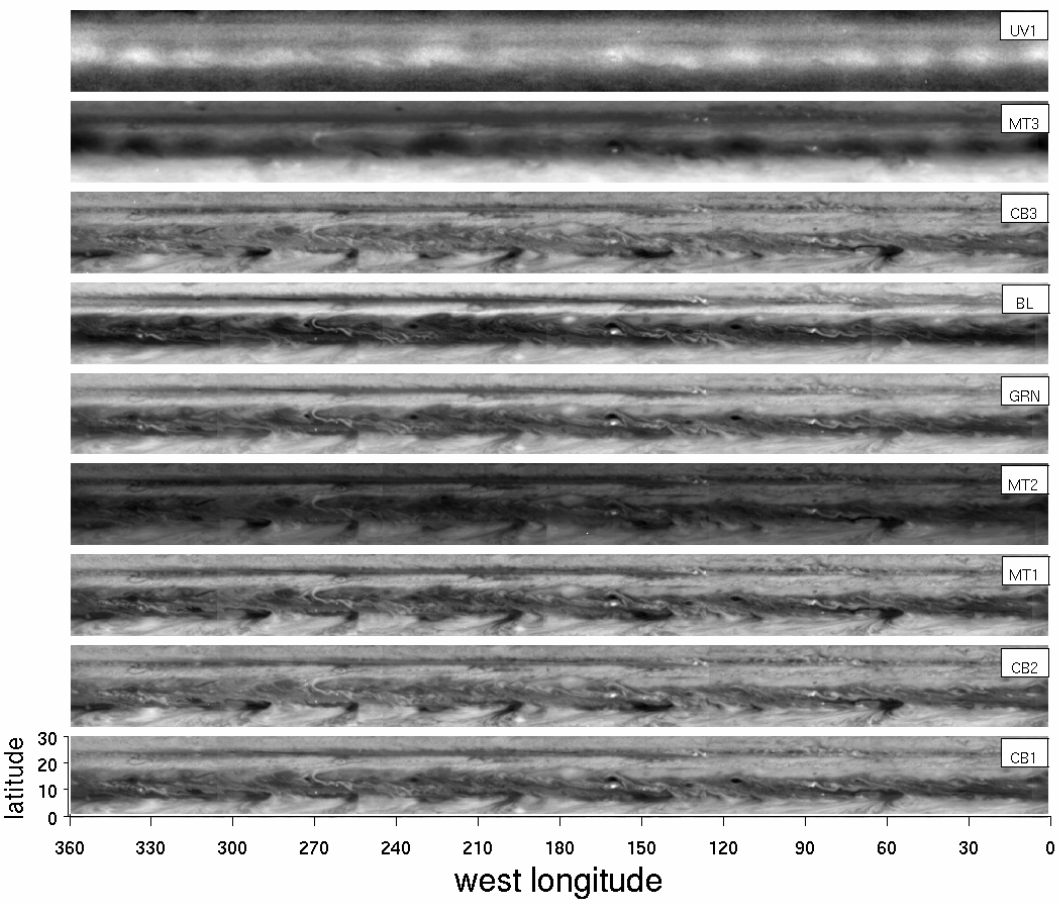

Figure 3.4 Polar-projected map of southern hemisphere of the UV1 global map of Fig. 2. The 30°N and 60°N latitude circles are shown in the figure.

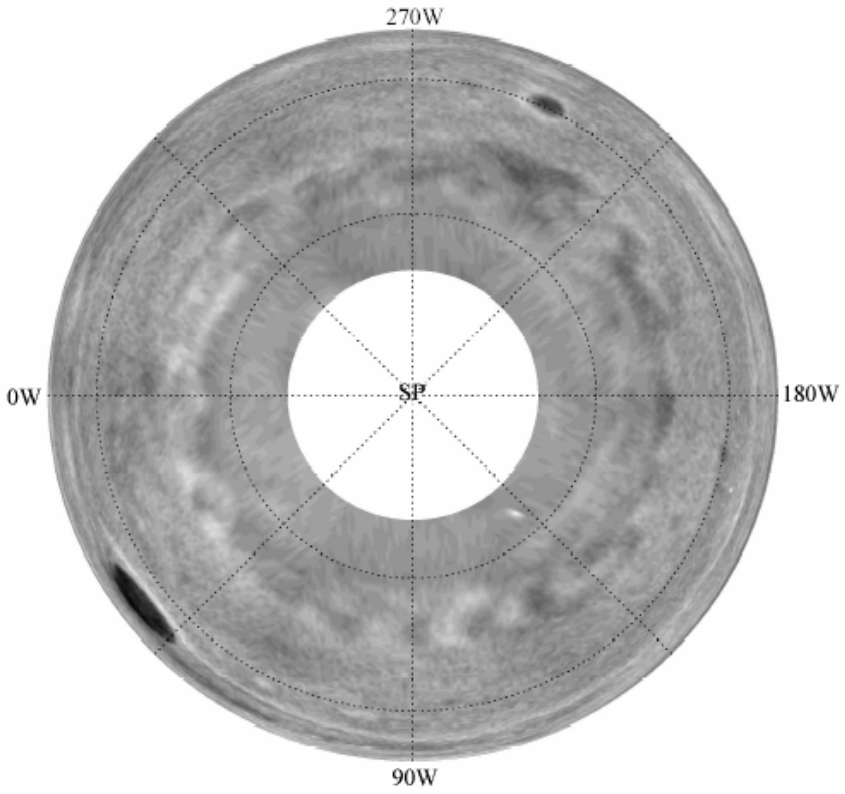

Figure 3.5 Time series of the NEB wave and the circumpolar wave in the UV1 filter. (A) Time series of the NEB wave with the time separation 5 days, which began on 2 October 2000 and ended on 10 November 2000. (B) Time series of the circumpolar wave with the time separation 1.7 days, which began on 28 October 2000 and ended on 12 November 2000. The dashed lines indicate the movements of the three crests.

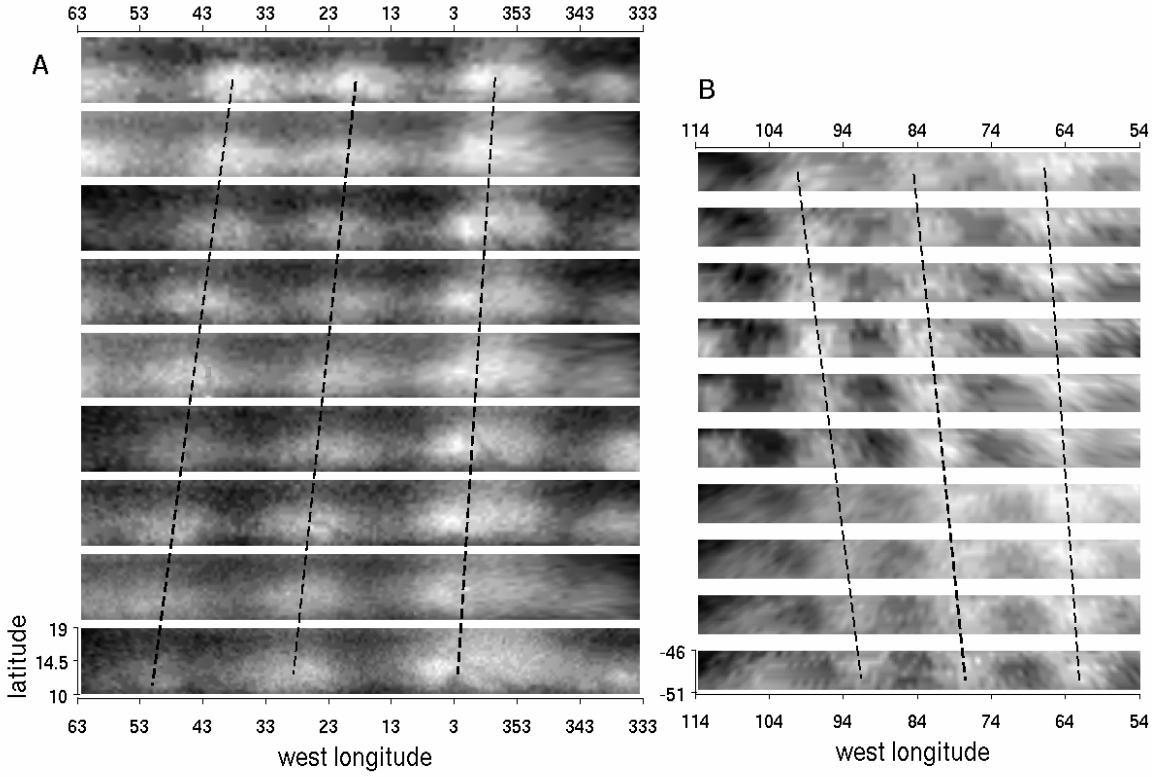

Figure 3.6 Velocities of the ambient flows within the latitude ranges of the NEB wave and the circumpolar wave in the UV1 and CB2 filters and average phase velocities of the two waves. (A) The NEB wave. (B) The circumpolar wave. The red solid lines are the velocities of the ambient flows in the UV1 filter coming from previous measurements by tracking the small features unique to the UV1 (Li et al., 2005). The green solid lines are the velocities of the ambient flows in the CB2 filter coming from an automatic-correlated measurement based on the time-lapse CB2 images in the Cassini ISS data sets (Porco et al., 2003). The red dots with error-bars are the mean phase velocities of the two waves by averaging the velocities of the three crests in (A) and (B) of figure 2. The error-bars are estimated by the standard deviation of the velocities of the three crests.

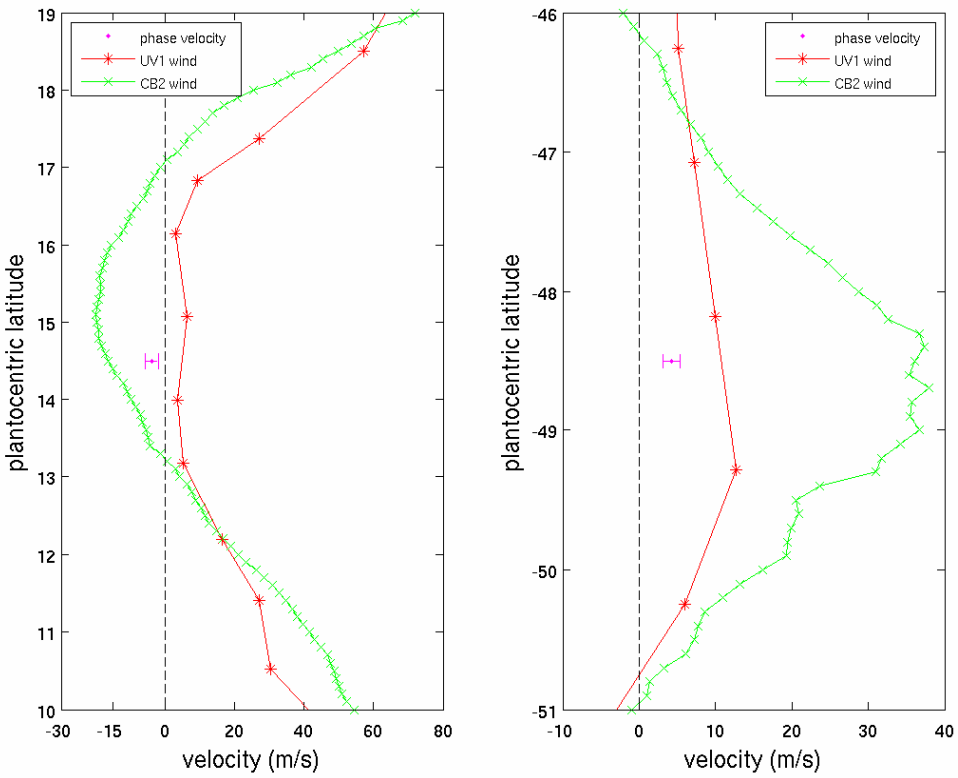

Figure 3.7 Simultaneous comparison between the CIRS global temperature map and the ISS MT3 global map in the equatorial regions. (A) The CIRS global temperature map at pressure level 400 mbar on 1 January 2001. White areas in (A) indicate gaps in the CIRS data coverage. (B) The ISS MT3 global map at the same time with (A). (C) Same with (B) except for removing mean value of every constant-latitude line to increase the feature contrast.

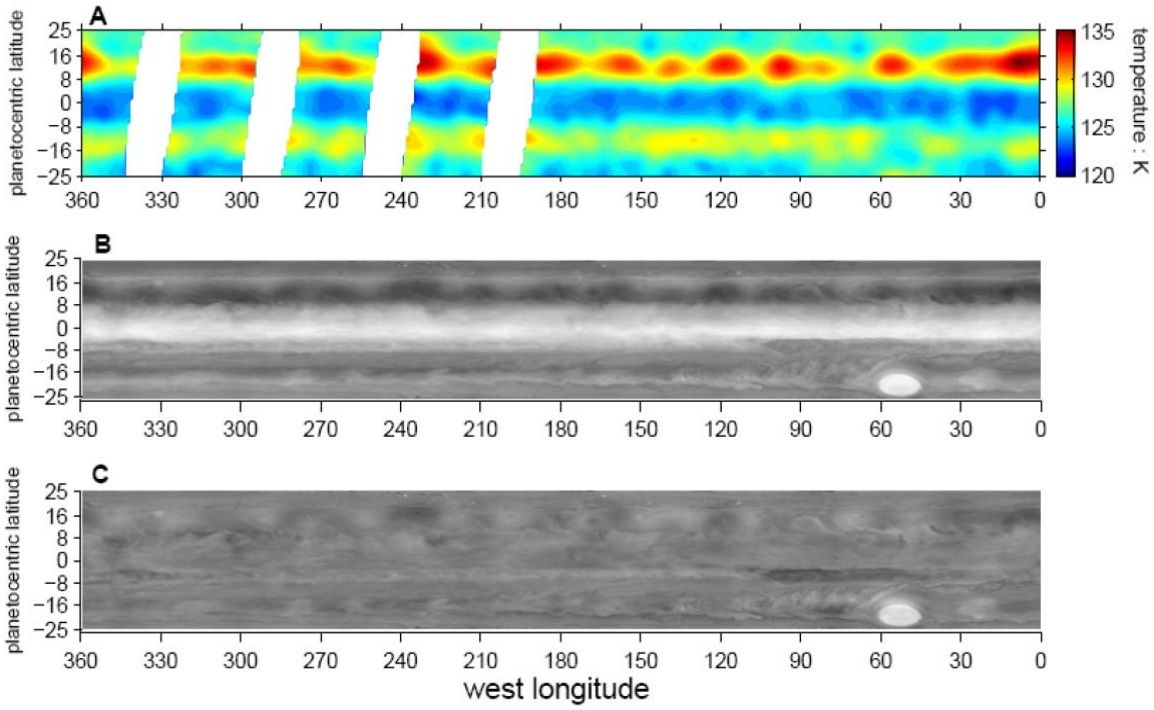

Figure 3.8 Near-simultaneous comparison for the NEB wave between the CIRS temperature maps and the ISS UV1 map. (A) The CIRS 400-mbar temperature map between longitude 135° to 300°W and latitude 12°S to 69°N on 5 January 2001. (B) The ISS UV1 map in the same location (longitude 135° to 300°W and latitude 12°S to 69°N) on 7 January 2001. The mean value of every constant-latitude line in the UV1 map is removed to increase the feature contrast. (C) Same with (A) except for a different time (10 January 2001). White areas in (A) and (C) and in the boundaries of (B) indicate gaps in the data coverage.

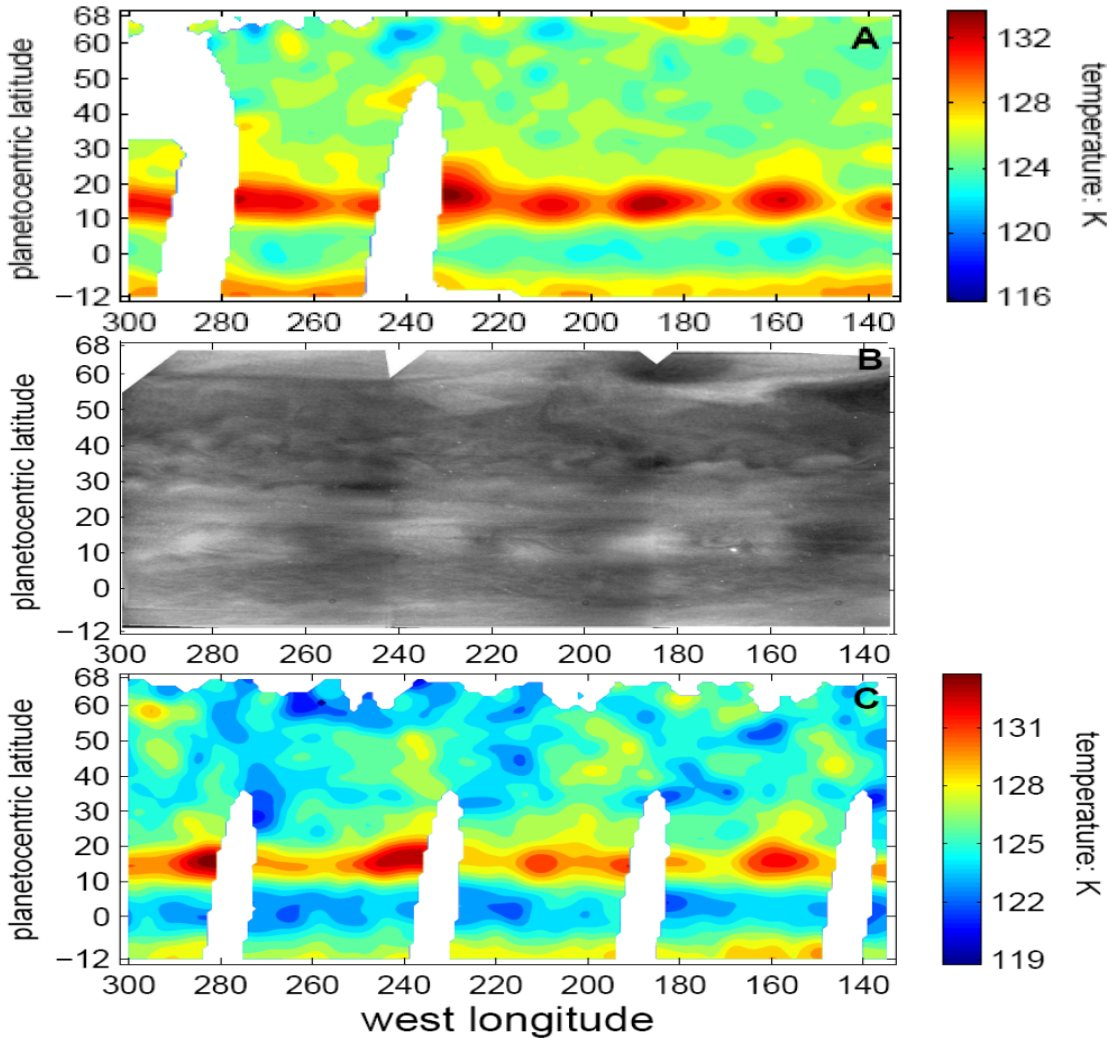

Figure 9. Time series of the NEB wave in the CIRS 400-mbar thermal maps. Panel (A), (B), and (C) are the CIRS 400-mbar thermal maps on 1, 5 and 10, January 2001, respectively. White areas in (A), (B) and (C) indicate gaps in the data coverage.

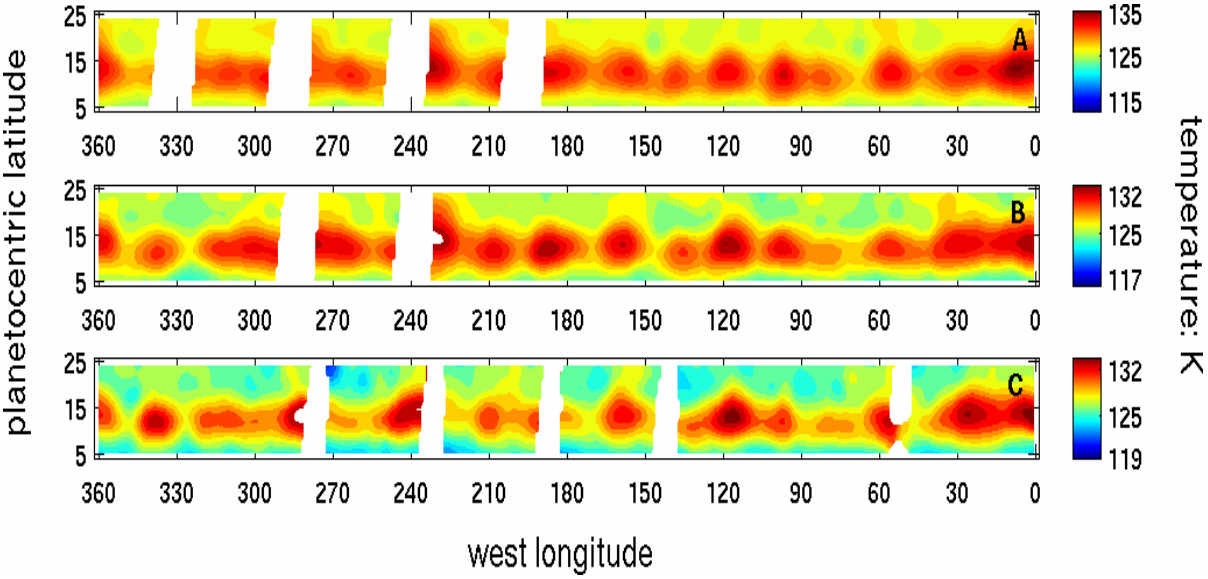

Figure 3.10 Simultaneous CIRS thermal maps at different pressure-levels. (A) The CIRS 1-mbar global temperature map on 1 January 2001. (B), (C), and (D) are same as (A) except for different pressure-levels (4-mbar, 243-mbar, and 400-mbar, respectively). White areas in these temperature maps indicate gaps in the CIRS data coverage.

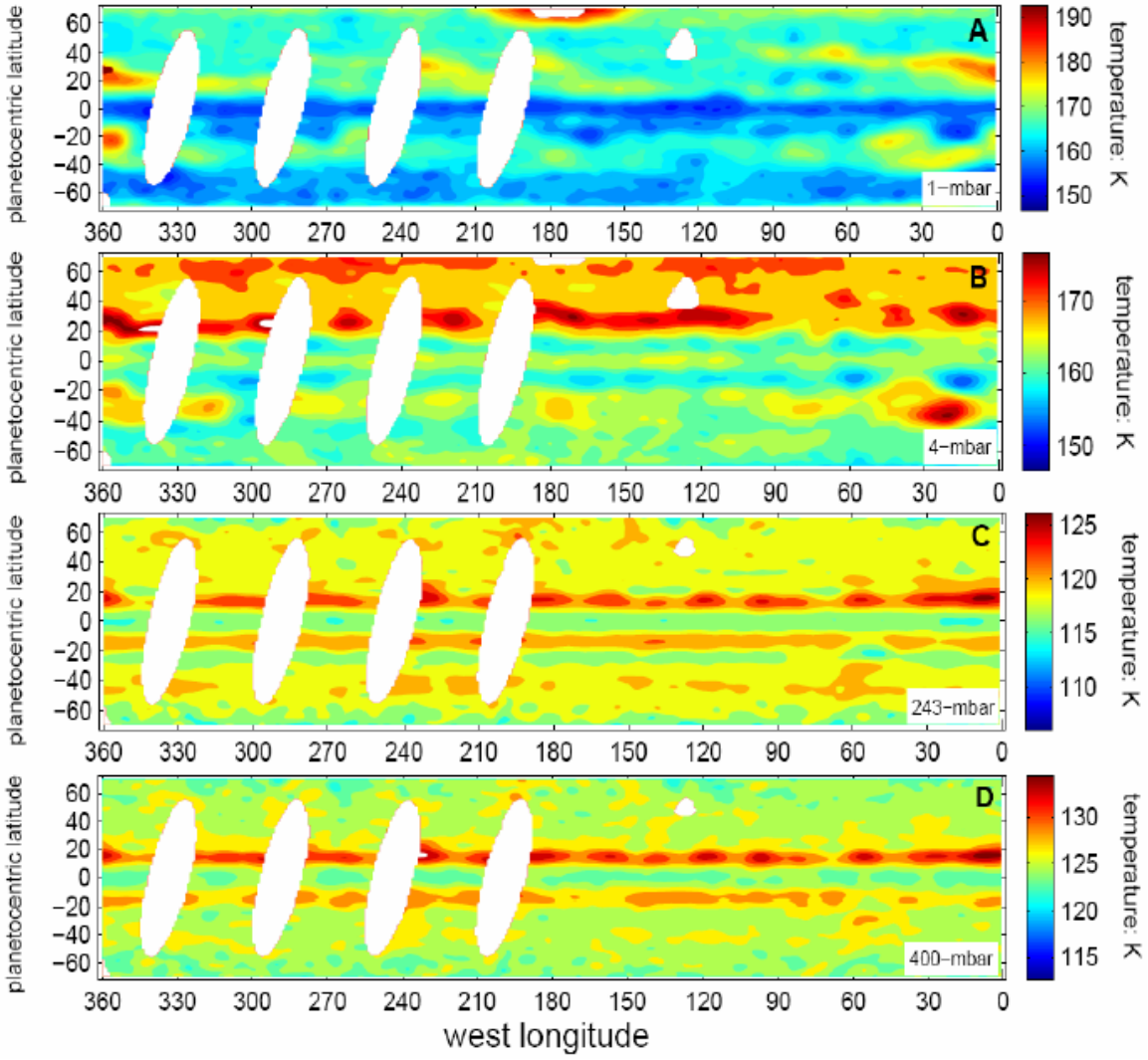

Figure 3.11 Near-simultaneous comparison on the large oval feature between the CIRS temperature maps and the ISS UV1 map. This figure is same as Fig. 8 except that the CIRS temperature maps are in a high-altitude pressure-level (1-mbar). The dark oval in the ISS UV1 maps is indicated by a white arrow.

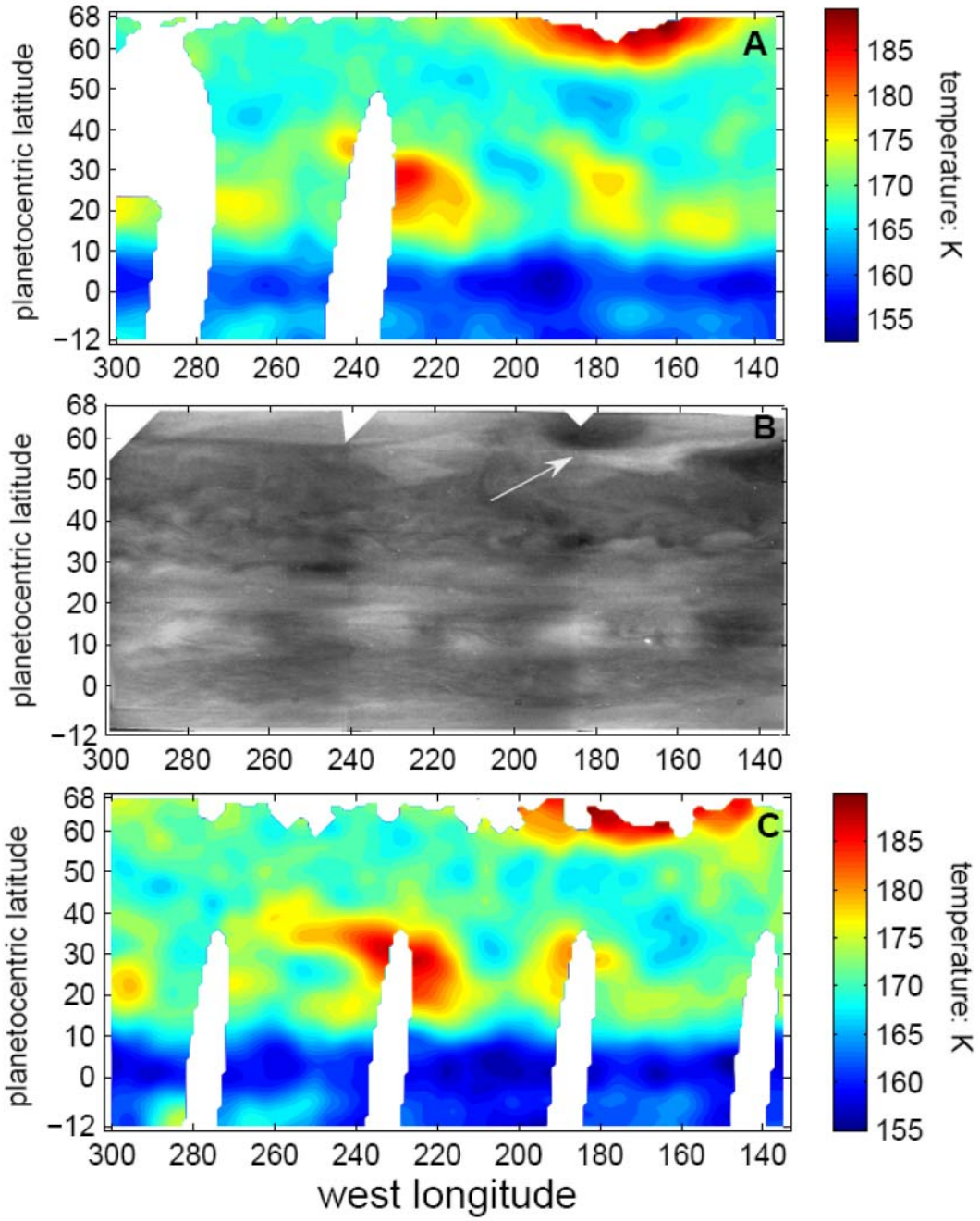

Figure 3.12 CIRS 315-mbar zonal wind profile and meridional gradients of vorticity within the latitude range of the NEB wave. (A) The CIRS 315-mbar zonal wind profile around the latitude range of the NEB wave and a cosine function fit. The cosine function is set to have different amplitudes for the 21°N eastward jet and the 7.5°N westward jet. (B) The vorticity gradients $\beta, \beta_y, \beta_z,$ and β_e at 315-mbar.

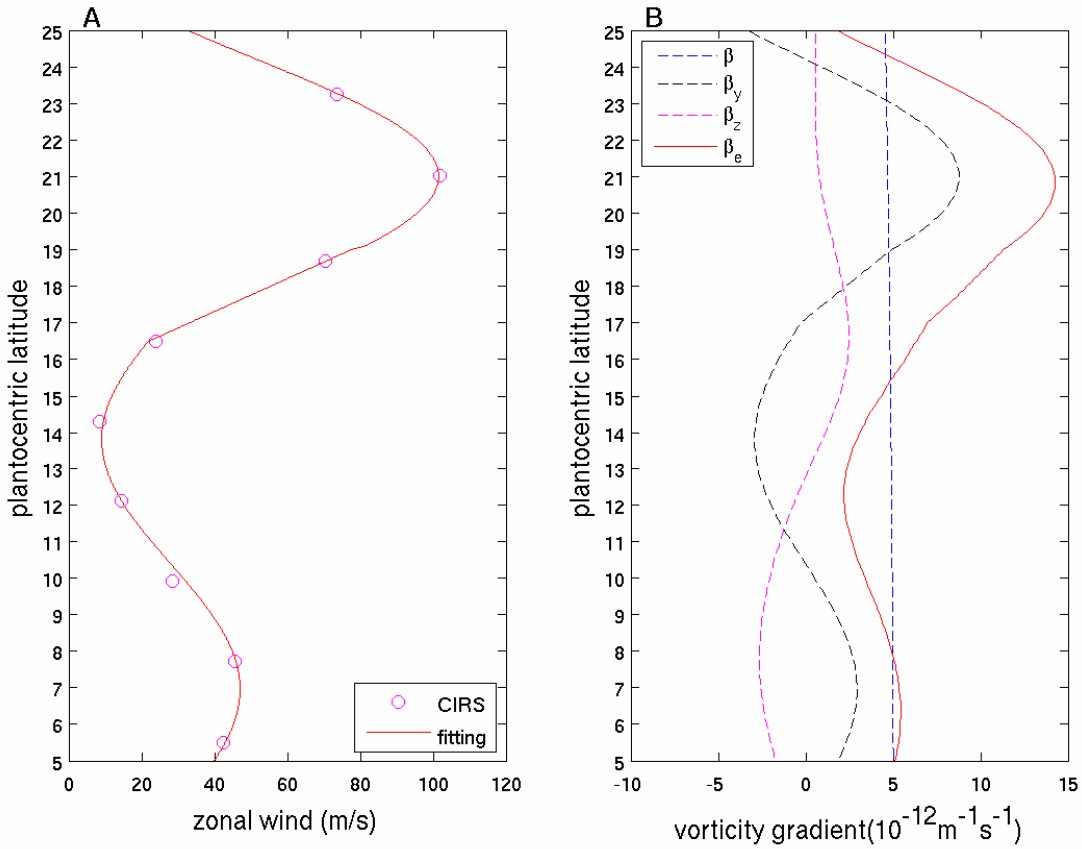

Figure 3.13 The square of the meridional wave-number of the NEB wave. The calculation of the meridional wave-number l^2 is based on Eq. (3) and the values of β_e in Fig. 12. The vertical wave-length L_z=160 km ($m = 0.39 \times 10^{-4}\,\mathrm{m}^{-1}$) is kept constant within the 315-mbar pressure surface in the above calculation.

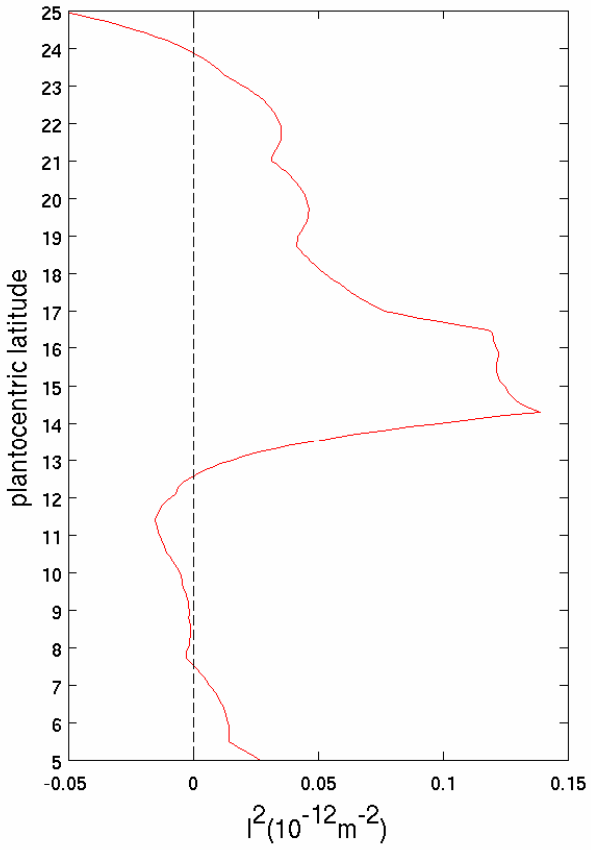

Figure 3.14 CIRS zonal wind profiles at different pressure levels, phase velocity of the NEB wave, and CB2 zonal winds at the pressure level of visible cloud deck. The red dot with error-bar represents the phase velocity of the NEB wave. The CB2 zonal winds are same as the CB2 zonal winds used in the Fig. 8, but more latitudes are included.

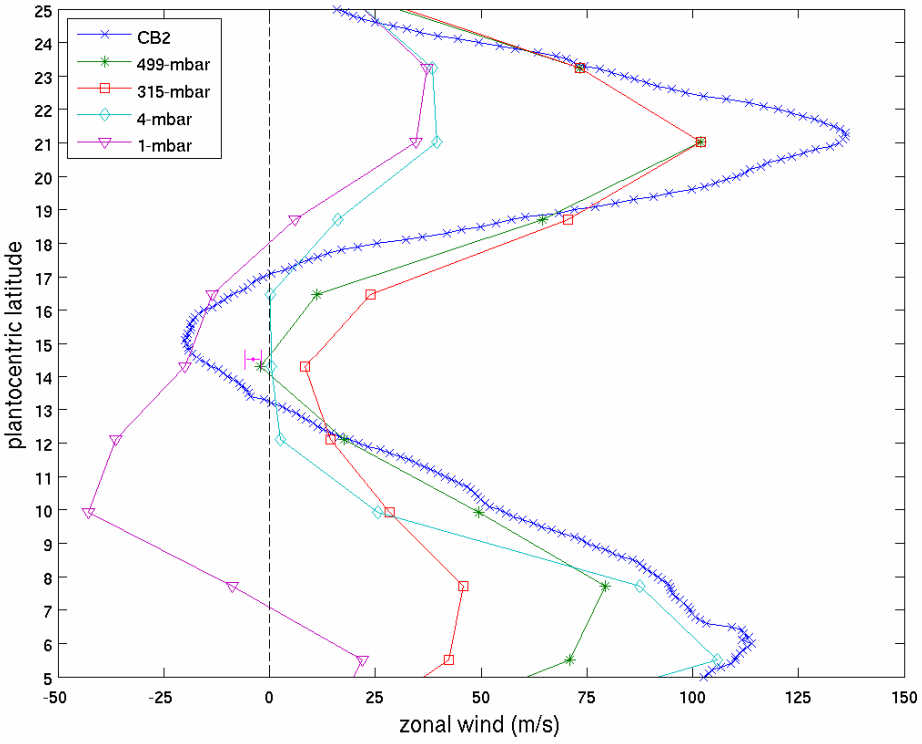

Figure 3.15 CB2 zonal wind profile and meridional gradients of vorticity within the latitude range of the NEB wave at the visible cloud deck (~ 0.7 bar). (A) The CB2-mbar zonal wind profile around the latitude range of the NEB wave and a cosine function fit. (B) The vorticity gradients $\beta, \beta_y, \beta_z,$ and β_e at ~ 0.7bar. The β_y at 315mbar is used for the CB2 pressure-level because the temperature fields at ~ 0.7 bar is unavailable.

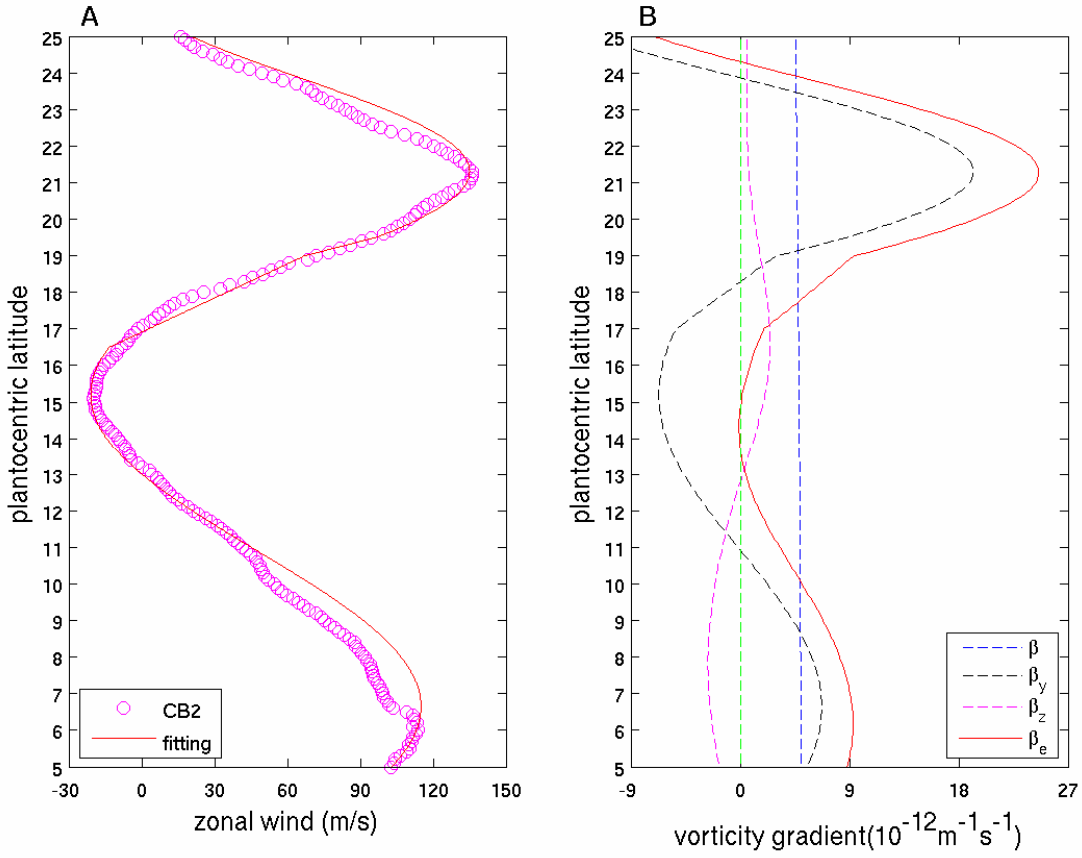

Chapter 4: Interaction of Moist Convection with Zonal Jets on Jupiter and Saturn

4.1 Abstract

Observations (Little *et al*., 1999; Porco *et al.*, 2003; Li *et al.*, 2004; Dyudina *et al.*, 2004; Gierasch *et al.*, 2000; Sanchez-Lavega *et al.*, 1999; Porco *et al.*, 2005) suggest that moist convection plays an important role in the large-scale dynamics of Jupiter's and Saturn's atmospheres. Here we use a reduced-gravity quasi-geostrophic model, with a parameterization of moist convection that is based on observations, to study the interaction between moist convection and zonal jets on Jupiter and Saturn. Stable jets with approximately the same width and strength as observations are generated in the model. The observed zonal jets violate the barotropic stability criterion (Li *et al.*, 2004; Ingersoll *et al.*, 1981; Limaye, 1986), but the modeled jets do so only if the flow in the deep underlying layer is westward. The model results suggest that a length scale and a velocity scale associated with moist convection control the width and strength of the jets. The length scale and velocity scale offer a possible explanation of why the jets of Saturn are stronger and wider than those of Jupiter.

4.2 Introduction

Multiple zonal jets in each hemisphere of Jupiter have been constant (Porco *et al.*, 2003; Garcia-Melendo and Sanchez-Lavega, 2001) in location and intensity since Voyager times even though some westward jets violate the barotropic stability criterion (Li *et al.*, 2004; Ingersoll *et al.*, 1981; Limaye, 1986). The jets outside the equatorial regions on Saturn are constant with time. HST observations (Sanchez-Lavega *et al*., 2003) and recent Cassini observations (Porco *et al.*, 2005) suggest that the equatorial jets may be constant in time as well, and that only the altitude of the visible clouds has changed.

Rhines (1975) first demonstrated that zonal jets emerge from decaying turbulence, during a process known as an inverse energy cascade. Williams (1978) first applied these ideas to Jupiter. Voyager observations (Ingersoll *et al.*, 1981; Beebe *et al.*, 1980; Ingersoll *et al.*, 1984) showed that the inverse cascade of energy plays an important role in the atmospheres of Jupiter and Saturn. Many two-dimensional turbulence models have addressed the large-scale dynamics of the giant planets in this way. The forced-dissipative turbulence models (Huang and Robinson, 1998; Marcus *et al*., 2000) use either a random Markov process or positive and negative sources of vorticity at a prescribed scale. The decaying turbulence models (Cho and Polvani, 1996) drive their simulation by an initial eddy field. One model (Panetta, 1993) is forced by a prescribed vertical shear of the zonal wind, which generates the turbulence. In all these models, the forces are prescribed, and are not affected by any feedback from the flow that develops. All models succeed in producing jets from turbulence, but the jets are not as intense as

the observed jets in Jupiter and Saturn: In these models, the largest value of the curvature of zonal jets U_{yy} is never larger than 0.3β. Here U is the mean zonal wind (positive eastward), y is the northward coordinate, and β is the planetary vorticity gradient. On Jupiter the largest values of U_{yy} are of order 2β (Li *et al*., 2004; Ingersoll *et al*., 1981; Limaye, 1986).

Models of the thermochemical structure suggest that moist convection (MC) exists in the atmospheres of Jupiter and Saturn (Lewis, 1969; Weidenschilling and Lewis, 1973). Observations from Voyager, ground-based telescopes, and HST show that a rich meteorological activity including convective storms exists there as well (Hunt *et al*., 1982; Carlson *et al*., 1992; Sanchez-Lavega, *et al*., 1999). The Galileo orbiter and Cassini flyby revealed important new information about MC in Jupiter's atmosphere. The relative humidity of water varies from 10^{-2} to 1.0 at the 260 K level (Roos-Serote *et al*., 2000). Lightning, which is a good indicator of MC, is associated with small (<1000 km), distinct, widely-separated cloud features that appear suddenly in the cyclonic regions (Little *et al*., 1999; Porco *et al*., 2003) and extend to great height (Banfield *et al*., 1998). The MC features are anticyclones (Li *et al*., 2004; Gierasch *et al*., 2000), although they appear in cyclonic shear zones. Generally they are either swallowed by the larger anticyclonic ovals like the Great Red Spot (GRS) or pulled apart by the shear of the zonal jets (Li *et al*., 2004).

One interpretation (Gierasch *et al*., 2000; Ingersoll *et al*., 2000) of these observations is that MC is providing energy to the large-scale flow structures in Jupiter's atmosphere.

Our model is based on the following concepts: The weather layer, which is the region between the base of the water cloud at ~6 bars and the level of emission to space at ~0.4 bars, rests hydrostatically on a much deeper lower layer. The interface is stable, so the potential temperature of the weather layer is greater than that of the lower layer. Heat from the planet's interior converts lower layer parcels into parcels whose potential temperature is equal to that of the weather layer. These parcels rise into the weather layer during a MC event. Steady radiative cooling converts weather layer fluid back into low-entropy fluid of the lower layer, so there is a net long-term balance. The MC events are triggered whenever the weather layer thickness falls below a certain threshold, which means that the MC events appear in the cyclonic regions, as observed. The injection of mass into the weather layer generates mesoscale anticyclonic (negative) vorticity (Little *et al*., 1999; Li *et al*., 2004; Gierasch *et al*., 2000), and the steady radiative cooling generates large-scale cyclonic (positive) vorticity. During the adjustment between the mesoscale forcing from MC and the large-scale forcing from radiation, the mechanical energy of mesoscale vortices is transferred to large-scale structures, *i.e.*, the GRS and zonal jets, by merging with them in an inverse energy cascade (Ingersoll *et al*., 1981; Beebe *et al*., 1980; Ingersoll *et al*., 1984).

There have been several numerical simulations of MC on Jupiter and Saturn (Stoker 1986; Yair *et al*., 1992, 1995; Hueso *et al*., 2002; Hueso and Sanchez-Lavega, 2001, 2004). However, the numerical simulation of the interactions between MC and the large-scale dynamics is a relatively new field partly due to the large difference in scale between the mesoscale processes and the large-scale dynamics. In this paper, we parameterize MC

using the available observations, and we study its role in maintaining the large-scale flow structures in the atmospheres of Jupiter and Saturn. We take the motions below the weather layer into account in order to get intense westward jets with curvature larger than β. These ideas are tested by a reduced-gravity quasigeostrophic (QG) model.

The assumptions of the QG model do not hold near the equator, so we cannot study the equatorial jets, which are strong and westerly on Jupiter and Saturn. A shallow water model (Cho and Polvani, 1996) generates strong easterly jets at the equator. Deep convection extending through the planet from north to south (Busse, 1976) makes westerly equatorial jets possible in theory. Numerical models of deep convection (Sun *et al*., 1993; Christensen, 2001; Aurnou and Olson, 2001; Yano *et al*., 2003) successfully reproduce the westerly equatorial jets, but the models generate fewer jets in the middle and high latitudes. We do not address these issues. The global wind profile including strong equatorial jets will be postponed for further research.

4.3 Numerical method

Two-dimensional flow in a rapidly rotating fluid is governed by the QG potential vorticity equation (Pedlosky, 1987; Andrews *et al*., 1987):

$$\frac{\partial q}{\partial t} + J(\psi, q) = S + F \qquad (1)$$

where the potential vorticity q is $\nabla^2\psi + \beta y - \psi / {L_d}^2$, ψ is the streamfunction, which is proportional to the thickness of the weather layer, β is the planetary vorticity gradient, and L_d is the radius of deformation. The non-linear term is the Jacobian $J = \psi_x q_y - \psi_y q_x$. Friction F is represented by horizontal eddy diffusion: $F = \kappa_h \nabla^2 \zeta$, where the relative vorticity ζ is $\nabla^2\psi$ and κ_h is the horizontal eddy diffusion coefficient. The vorticity source S consists of two parts: 1) a positive constant S_r that represents uniform radiative cooling and 2) negative bursts, localized in space and time, that represent MC. When radiative cooling and dynamics make the thickness of the weather layer drop below a critical threshold at some place, MC will be excited there and will increase the thickness of the local weather layer. The assumption of MC excited in the regions where the thickness of the local weather layer is small implies that MC will only appear in the cyclonic bands, which are small-thickness regions in Jupiter. MC therefore creates intense regions of anticyclonic vorticity in regions where the large-scale vorticity is cyclonic, which is consistent with the observations (Little *et al*., 1999; Porco *et al.*, 2003; Li *et al.*, 2004; Dyudina *et al.*, 2004; Gierasch *et al.*, 2000).

We parameterize the vorticity source due to MC by a function with negative parabolic shape in lifetime and radius. The lifetime, radius and amplitude of the vorticity source due to MC are constrained by observations from Voyager, Galileo, Cassini, HST and ground-based telescopes. Large uncertainties exist in these observations, so we explore the parameter space around a standard model. Galileo and Cassini observations (Little *et al*., 1999; Porco *et al.*, 2003) show that the size of MC ranges from a few hundred

kilometers to a few thousand kilometers. Cassini continuum images (Li *et al.*, 2004) suggest that the lifetime of MC is 3.5 days, but these measurements refer to storms with lifetime larger than 40 hours and diameter larger than 700 kilometers. Obviously, some small convective storms have shorter lifetime. Our standard model has lifetime of 1 day and diameter of 1000 kilometers, although we varied the lifetime between 0.3 and 6 days and the radius between 250 and 4000 km. The amplitude of the vorticity source due to MC is S_{mc}, which is given by S_r / C_{mc}, where S_r is the radiation vorticity source, and C_{mc} is the fractional area of MC over the global disk, under the assumption that the negative vorticity source due to MC is balanced by the positive vorticity source due to uniform radiative cooling. The fractional area of MC is set to 1×10^{-4} based on the Galileo and Cassini observations (Little *et al.*, 1999; Dyudina *et al.*, 2004). The calculation of the radiation vorticity source S_r is given in the appendix. We varied the amplitude of the vorticity source due to MC by a factor of 20. The horizontal eddy diffusion κ_h is set to 10^3 $\mathrm{m^2\,s^{-1}}$ to give horizontal eddy diffusion the same net effect as vertical eddy diffusion, assuming that the vertical eddy diffusion is $\sim 10^{-1}$ $\mathrm{m^2\,s^{-1}}$ in the upper troposphere of Jupiter (Edgington *et al.*, 1999) and the horizontal scale is 100 times the vertical scale for the jovian weather layer. The radius of deformation L_d on Jupiter is unknown but has been estimated by different studies. Ingersoll and Cuong (1981) suggested the radius of deformation is in the range of 500 – 5000 km. Achterberg and Ingersoll (1989) concluded that the radius of deformation is likely on the order of 1000 km by comparing their model results with the observations. Dowling and Ingersoll (1989) estimated the radius of deformation from the potential vorticity and offered a value of L_d

~ 2000 km. In this study, we set the standard value of L_d as 5000 km to guarantee small S_r, so that the corresponding S_{mc} can change in a relatively large range (see Eq. (7) in Appendix). In addition, the numerical experiments in the next section show that our QG model is insensitive to the radius of deformation. Without loss of generality, we keep S_r and β constant in all experiments, which is equivalent to fixing the units of length and time.

Our numerical code for solving equation (1) is a finite-difference scheme with Arakawa's energy- and enstrophy-conserving algorithm in space (Arakawa, 1966) and the modified fourth-order Adams-Bashforth algorithm in time (Press *et al*., 1986). The latter is initiated by the Runge-Kutta method (Press *et al*., 1986). A periodic boundary condition is used in the *x* (zonal) direction, so a fast Fourier transform and an inverse fast Fourier transform can be performed. Channel walls are used in the *y* (meridional) direction (Holton, 1979, p. 252). Such boundary conditions allow the weather layer to change its total momentum. All numerical experiments begin with a random initial streamfunction pattern. The standard domain size is 32 thousand kilometers in the x and y directions in order to include multiple jets, although we have run cases with larger domains in the x and y directions. The space resolution is generally 250 km in both directions and the time step is 1000 s in order to capture MC. We have verified that the results are independent of the resolution, domain size, and random initial pattern. Figure 1 displays two different initial random patterns and the corresponding steady patterns of streamfunction. The figure shows that the same steady pattern is developed from the different initial random

patterns. In Fig. 2 we run the numerical model with different domain sizes by setting the same initial random pattern as in Fig. 1a and holding the same group of parameters ($T_{mc} = 1$ day, $R_{mc} = 1000$ km, $S_{mc} = 1.0 \times 10^{-9}$ s^{-2}, $L_d = 5000$ km, and $\kappa_h = 10^3$ m^2 s^{-1}). Figure 2 shows that the coherent zonal pattern still forms and the zonal wind profile does not change when the domain size is expanded, although some large-scale vortices are clearly displayed in the largest x domain experiment (Fig. 2d). Notice that the vortices at ~ 26000 km in Fig. 2d alternate in longitude (y direction) with oppositely-signed vortices at $y \sim 20000$ km, which is suggestive of a Karman vortex street (Youssef and Marcus, 2003). These large-scale vortices showed in Fig. 2d are aligned around the same latitude so that they do not change the zonal wind profile. However, the co-existence of large-scale vortices and stable zonal wind is a very interesting phenomenon, which is worthy of further study. The experiments shown in Figs.1 and 2 suggest that our numerical model is independent of the initial random pattern, the spatial resolution, and the domain size. Therefore, we use the same initial random pattern (Fig. 1a), the same spatial resolution (250 km), and the same domain size (32000 km in the x and y directions) for all following numerical experiments.

4.4 Simulation results

Large uncertainties exist in the radius of deformation, the horizontal eddy diffusion, and the parameters associated with MC. A series of numerical experiments are performed to explore the parameter space. An example of these numerical experiments, which is run with standard values of parameters except for the increased amplitude of the vorticity

source S_{mc}, is shown in Fig. 3. Figures 3a - 3f show a time series of stable zonal jets developing from a random initial pattern during the process of adjustment between MC and radiation. A statistically steady large-scale pattern is generated after 1 year, shown in Fig. 3e. Figure 3e also includes a MC event near the center of the domain. Figure 3f shows the location of all MC events over a four-year period after the large-scale flow had reached a statistically steady state. This figure demonstrates that MC only appears in cyclonic bands. Figure 4 is the corresponding zonal wind profile for the steady state phase of the experiment shown in Fig. 3. The width of the modeled stable jets (half wavelength of the zonal wind profile) is a few thousand kilometers, and the peak zonal wind is around 20 m s^{-1}. Both width and strength of the modeled jets have the same order of magnitude as the observed jets outside the equatorial regions on Jupiter. Figure 5 displays the time series of energy of the experiment shown in Fig. 3. The time series of energy suggests that the developed zonal jet pattern is in a statistically steady state after the initial adjustment.

Parameter space exploration in certain ranges around standard values is shown in Fig. 6. In general, no clear zonal patterns are developed beyond these ranges. The figure shows that the width L_{jet} and strength V_{jet} of the jets in our experiments are insensitive to the radius of deformation and the horizontal eddy diffusion coefficient. The width L_{jet} and strength V_{jet} vary directly with the parameters associated with MC: R_{mc}, T_{mc}, and S_{mc}. Hence, we define a velocity scale $V = R_{mc}T_{mc}S_{mc}/2$ and a length scale $L = \sqrt{V/\beta}$. Figure 7 shows that L_{jet}/L and V_{jet}/V do not change as we vary the parameters associated with

MC. In other words, our experiments suggest that the width and amplitude of stable jets are controlled by the length scale L and velocity scale V. Actually, the velocity scale V represents the tangential velocity that is generated at the edge of a MC event at the end of its lifetime. The length scale L is the same as the Rhines scale $\sqrt{V_{jet}/\beta}$ when the velocity scale V is proportional to the amplitude of the jets V_{jet}. The above results also suggest that the parameters of MC do not change the curvature U_{yy} of the zonal wind profile because the curvature is proportional to V_{jet}/L_{jet}^{2}. Further exploration of parameter space of MC verifies this point: Figure 8 shows that the ratio between the curvature of the jets and the planetary vorticity gradient varies around 0.5, but the ratio is never larger than 1. This is consistent with the barotropic stability criterion, which says that flow is stable when $\beta - U_{yy} > 0$ and may be unstable when $\beta - U_{yy}$ changes sign.

To get the observed strong zonal wind with $\beta - U_{yy}$ changing sign around the westward jets, we invoke motions below the weather layer. The Galileo probe measured winds down to the 20-bar level and found that the equatorial eastward jet increased with depth within the weather layer and stayed constant at a high velocity from 5 bars to 20 bars (Atkinson *et al.,* 1998). Study of the coupled magnetic field and zonal flow in the interior of Jupiter (Liu and Stevenson, 2003; Kirk and Stevenson, 1987) suggests that retrograde (westward) deep flow will exist in middle and high latitudes and prograde (eastward) deep flow will exist in equatorial regions. In this paper, the deep flow is assumed to be zonal and steady in the whole domain. The corresponding QG model including the zonal

deep flows is dynamically equivalent to a one-layer model with meridionally varying solid bottom topography, called the reduced-gravity model (Dowling and Ingersoll, 1989). The gravity g is interpreted as $g' = g\Delta\rho/\rho$, where $\Delta\rho$ is the density difference between the weather layer and the deep layer, and ρ is the mean density of the weather layer. The stability criterion for the weather layer jets is changed into (Pedlosky, 1987. pp. 478-478):

$$\beta - U_{yy} + \frac{1}{L_d^{\,2}}(U - U_2) = \beta_{eff} - U_{yy} > 0 \qquad (2)$$

where the deep zonal velocity is U_2, and the effective planetary vorticity gradient is $\beta_{eff} = \beta + (U - U_2)/L_d^{\,2}$. The inequality (2) shows that the weather layer jets would be stable provided $(U - U_2) > L_d^{\,2}(U_{yy} - \beta)$. Since β_{eff} is largest when the deep flow U_2 is strong and westward relative to the weather layer flow U, the curvature U_{yy} will increase as U_2 becomes more negative. Figure 9 shows that the observed sharp westward jets with curvature U_{yy} larger than β can be simulated with a uniform westward deep flow. The westward deep flow offers a possible and simple explanation of why the weather layer jets remain stable even though they violate the barotropic stability criterion.

The experiments for Jupiter suggest that the width and strength vary directly with the lifetime, radius, and amplitude of MC. The limited observations from Voyager, HST, ground-based telescopes, and Cassini (Sanchez-Lavega *et al*., 1999; Porco *et al*., 2005)

have shown giant convective storms in Saturn's atmosphere with diameter around a few thousand kilometers and lifetime around a few weeks. In addition, observations (Beebe, *et al*., 1992; Sanchez-Lavega, *et al*., 1991,1996) and numerical simulations (Sayanagi *et al*., 2004) suggest that very giant convective storms play an important role in the dynamics of Saturn's equatorial atmosphere. These observations also suggest that Saturn has fewer convective storms than Jupiter. We can simulate the wide and strong zonal jets of Saturn relative to Jupiter by increasing the lifetime and radius of MC and decreasing the fractional area of MC over the global disk. Figure 10 shows a comparison between the model result and the observed zonal wind profiles in the middle latitudes of Saturn, and is to be compared with Figs. 4 and 9 for the middle latitudes of Jupiter. The result suggests that the large differences of width and strength of the jets between Jupiter and Saturn are probably due to the different characteristics of MC (lifetime, size and frequency). What controls the characteristics of MC in Jupiter and Saturn is proposed for further study.

4.5 Conclusions and discussions

Our study suggests that MC can drive the zonal jets in the atmospheres of Jupiter and Saturn. The width and strength of the jets are controlled by the length scale and velocity scale associated with MC. The length scale and velocity scale also offer an explanation for the different width and strength of jets on Jupiter and Saturn. Sharp westward jets with curvature larger than the planetary vorticity gradient can be simulated with westward flow below the weather layer.

There are strong equatorial eastward jets in Jupiter and Saturn. Our QG model and previous QG models of the giant planets (Panetta 1993; Marcus and Lee, 2000) are not suitable to study the equatorial regions. Decaying turbulence in a shallow water model cannot generate eastward equatorial jets (Cho and Polvani, 1996). Observations (Little *et al.,* 1999; Sanchez-Lavega *et al.,* 1999; Porco *et al.,* 2003, 2005; Li *et al.,* 2004) show that MC is active in the equatorial regions of Jupiter and Saturn. Therefore, the idea of MC driving jets should be tested in equatorial regions with new numerical models.

Laboratory models are important as a way to study atmospheric dynamics. Previous laboratory models drive the jets either with a radial temperature gradient in a rotating bowl cooled from above (Condie and Rhines 1994) or sources and sinks of the same size on the bottom of a rotating annular tank (Sommeria *et al*. 1989). Here, we suggest that the latter laboratory experiment should be redone with uniform small sinks and a few large sources from the bottom.

4.6 Appendix: Calculation of radiation vorticity source

To calculate the radiation vorticity source S_r, we start with conservation of mass for the weather layer

$$Dh/Dt + h_0 \nabla \cdot \vec{V} = \dot{h}_r + \dot{h}_{mc} \tag{3}$$

where the thickness h of the weather layer is $h_0 + h'$, and the average thickness h_0 is much larger than the perturbation thickness h'. The divergence of the horizontal velocity is $\nabla \cdot \vec{V}$, the rate of thickness increase due to mass removed from the weather layer by net radiation is $\dot{h}_r$, a negative quantity, and the rate of thickness increase due to mass added to the weather layer by MC from the deep underlying layer is $\dot{h}_{mc}$, a positive quantity. The outgoing energy flux due to net radiation is assumed as F_r. Therefore, we have $F_r = -C_p \Delta\theta \rho \dot{h}_r$, where C_p is the specific heat, $\Delta\theta$ is the potential temperature of the weather layer minus that of the deep layer, and ρ is the mean density of the weather layer.

The large-scale vorticity equation (Holton, 1979) of the weather layer is

$$D\zeta/Dt + \beta v + f_0 \nabla \cdot \vec{V} = 0 \tag{4}$$

The streamfunction ψ is defined as $g'h'/f_0$, where $g' = g\Delta\rho/\rho = g\Delta\theta/\theta$ is the reduced gravity of the two-layer QG model and f_0 is the Coriolis parameter.Combining Eqs. (3) and (4) and eliminating $\nabla \cdot \vec{V}$, we have

$$D\zeta / Dt + \beta v - (f_0 / h_0)(Dh / Dt - \dot{h}_r - \dot{h}_{mc}) = 0 \quad (5)$$

From $\psi = (h' / f_0)(g\Delta\theta / \theta)$, we have $Dh / dt = Dh' / dt = (f_0\theta / g\Delta\theta) D\psi / dt$. Substituting Dh / dt into Eq (5), we have

$$D\zeta / Dt + \beta v - (1 / L_d^{\,2}) D\psi / Dt = \partial q / \partial t + J(\psi, q) = -(f_0 / h_0)(\dot{h}_r + \dot{h}_{mc}) \quad (6)$$

where the potential vorticity q is $\nabla^2\psi + \beta y - \psi / L_d^{\,2}$ and the radius of deformation L_d is $\sqrt{g\, h_0\, \Delta\theta / (f_0^{\,2}\theta)}$. Therefore, substituting $\dot{h}_r$ into Eq. (6) and using the pressure $P = \rho g h_0$, we have

$$S_r = -(f_0 / h_0)\dot{h}_r = \gamma\, g\, F_r / (P\, f_0\, L_d^{\,2}) \quad (7)$$

where γ is the ratio of the gas constant R to the specific heat C_p. So by setting $\gamma = 1/3$, $g = 24$ m s^{-2}, $F_r = 5.7$ W m^{-2}, $P = 5\times10^5$ Pa, $f_0 = 1.7\times10^{-4}$ s^{-1}, and $L_d = 5000$ km, we have $S_r = 2.14\times10^{-14}$ s^{-2} for Jupiter. Likewise, we have $S_r = 1.26\times10^{-15}$ s^{-2} for Saturn by setting $\gamma = 0.28$, $g = 9$ m s^{-2}, $F_r = 2$ W m^{-2}, $P = 10\times10^5$ Pa, $f_0 = 1.6\times10^{-4}$ s^{-1}, and $L_d = 5000$ km.

4.7 References

Achterberg, R.K., Ingersoll, A.P., 1989. A normal-mode approach to jovian atmospheric dynamics. J. Atmos. Sci. 46, 2448-2462.

Andrews, D.G., Holton, J.R., Leovy, C.B., 1987. Middle atmosphere dynamics. Academic Press.

Arakawa, A., 1966. Computational design for long-term numerical integration of the equations of fluid motion: Two-dimensional incompressible flow. J. Comput. Phys. 1, 119-143.

Atkinson, D.H., Pollack, J.B., Seiff, A., 1998. The Galileo Probe Doppler Wind Experiment: Measurement of the deep zonal winds on Jupiter. J. Geophys. Res. 103, 22911-22928.

Aurnou, J.M., Olson, P.L., 2001. Strong zonal winds from thermal convection in a rotating spherical shell. Geophys. Res. Lett. 28, 2557-2559.

Banfield, D., Gierasch, P.J., Bell, M., Ustinov, E., Ingersoll, A.P., Vasavada, A.R., West, R.A., Belton, M.J.S., 1998. Jupiter's cloud structure from Galileo imaging data. Icarus 135, 230-250.

Beebe, R.F., Ingersoll, A.P., Hunt, G.E., Mitchell, J.L., Muller, J.P., 1980. Measurements of wind vectors, eddy momentum transports, and energy conservations in Jupiter's atmosphere from Voyager 1 images. Geophys. Res. Lett. 7, 1-4.

Beebe, R.F., Barnet, C., Sada, P.V., Murrell, A.S., 1992. The onset and growth of the 1990 equatorial disturbances on Saturn. Icarus 95, 163-172.

Busse, F.H., 1976. A simple model of convection in the jovian atmosphere. Icarus 29, 255-260.

Carlson, B.E., Lacis, A.A., Rossow, W.B., 1992. The abundance and distribution of water vapor in the jovian troposphere as inferred from Voyager IRIS observations. Astrophys. J. 388, 648-668.

Cho, J.Y.K., Polvani, L.M., 1996. The morphogenesis of bands and zonal winds in the atmospheres on the giant outer planets. Science 273**,** 335-337.

Christensen, U.R., 2001. Zonal flow driven by deep convection in the major planets. Geophys. Res. Lett. 28, 2553-2556.

Condie, S.A., Rhines, P.B., 1994. A convective model for the zonal jets in the atmospheres of Jupiter and Saturn. Nature 367, 711-713.

Dowling, T.E., Ingersoll, A.P., 1989. Jupiter's Great Red Spot as a shallow water system. J. Atmos. Sci. 46, 3256-3278.

Dyudina, U.A., Del Genio, A.D., Ingersoll, A.P., Porco, C.C.,West, R.A., Vasavada, A.R., Barbara, J.M., 2004. Lightning on Jupiter observed in the H_α line by the Cassini imaging science subsystem. Icarus 172**,** 24-36.

Edgington, S.G., Atreya, S.K., Trafton, L.M., Caldwell, J.J., Beebe, R.F., Simon, A.A., West, R.A., 1999. Ammonia and eddy mixing variations in the upper troposphere of Jupiter from HST Faint Object Spectrograph observations. Icarus 142, 342-356.

Garcia-Melendo, E., Sanchez-Lavega, A., 2001. Study of the stability of jovian zonal winds from HST images: 1995-2000. Icarus 152, 316-330.

Gierasch, P. J., Ingersoll, A.P., Banfield, D., Ewald, S.P., Helfenstein, P., Simon-Miller, A., Vasavada, A., Breneman, H.H., Senske, D.A., 2000. Observation of moist convection in Jupiter's atmosphere. Nature 403, 628-630.

Holton, J.R., 1979. Introduction to Dynamic Meteorology, 2nd edition. Academic Press.

Huang, H.P., Robinson, W.A., 1998. Two-dimensional turbulence and persistent zonal jets in a global barotropic model. J. Atmos. Sci. 55, 611-632.

Hueso, R, Sanchez-Lavega, A., 2001. A three-dimensional model of moist convection for the giant planets: the Jupter case. Icarus 151**,** 257-274.

Hueso, R., Sanchez-Lavega, A., Guillot, T., 2002. A model for large-scale convective storms in Jupiter. J. Geophys. Res. 107**,** 5075-5085.

Hueso, R., Sanchez-Lavega, A., 2004. A three-dimensional model of moist convection for the giant planets II: Saturn's water and ammonia moist convetive storms. Icarus 172**,** 255-271.

Hunt, G.E., Godfrey, D., Muller, J.P., Barrey, R.F.T., 1982. Dynamical features in the northern hemisphere of Saturn from Voyager 1 images. Nature 297, 132-134.

Ingersoll, A.P., Beebe, R.F., Mitchell, J.L., Garneau, G.W., Yagi, G.M., Muller, J.P., 1981. Interactions of eddies and mean zonal flow on Jupiter as inferred from Voyager 1 and 2 images. J. Geophys. Res. 86**,** 8733-9743.

Ingersoll, A.P., Beebe, R.F., Conrath, B.J., Hunt, G.E., 1984. in Saturn (eds Gehrels, T. and Matthews, M.S.). Univ. Arizona Press 195-238.

Ingersoll, A.P., Cuong, P.G., 1981. Numerical model of long-lived jovian vortices. J. Atmos. Sci. 38, 2067-2076.

Ingersoll, A.P., Gierasch, P.J., Banfield, D., Vasavada, A.R., 2000. Moist convection as an energy source for the large-scale motions in Jupiter's atmosphere. Nature 403, 630-632.

Kirk, R.L., Stevenson, D.J., 1987. Hydromagnetic constraints on deep zonal flow in the giant planets. Astrophys. J. 316, 836-846.

Lewis, J.S., 1969. The clouds of Jupiter and the NH_3-H_2O and NH_3-H_2S systems. Icarus 10, 365-378.

Li, L., Ingersoll, A.P., Vasavada, A.R., Porco, C.C., Del Genio A. D., Ewald, S.P., 2004. Life cycles of spots on Jupiter from Cassini images. Icarus 172, 9-23.

Limaye, S.S., 1986. Jupiter: New estimates of the mean zonal flow at the cloud level. Icarus 65, 335-352.

Little, B., Anger, C.D., Ingersoll, A.P., Vasavada, A.R., Senske, D.A., Breneman, H.H., Borucki, W.J., 1999. Galileo images of lightning on Jupiter. Icarus 142, 306-323.

Liu, J.J., Stevenson, D.J., 2003. Constraints on the observed zonal flows from the magnetic fields in giants. Bull. Amer. Astron. Soc. 35**,** 1008.

Marcus, P.S., Kundu, T., Lee, C, 2000. Vortex dynamics and zonal flows. Phys. Plasmas. 7, 1630-1640.

Panetta, R.L., 1993. Zonal Jets in wide baroclinically unstable regions - persistence and scale selection. J. Atmos. Sci. 50, 2073-2106.

Pedlosky, J., 1987. Geophysical Fluid Dynamics, 2nd edition. Springer-Verlag, New York. pp. 478-478.

Porco, C.C., 23 colleagues, 2003. Cassini images of Jupiter's atmosphere, satellites, and rings. Science 299, 1541-1547.

Porco, C.C., 34 colleagues, 2005. Cassini Imaging Science: Initial results on Saturn's atmosphere. Science 307, 1243-1247.

Press, W.H., Teukolsky, S.A., Vetterling, W.T., Flannery, B.P., 1986. Numerical Recipes: The Art of Scientific Computing. Cambridge University Press.

Rhines, P. B., 1975. Waves and turbulence on a beta-plane. J. Fluid Mech. 69, 417-443.

Roos-Serote, M., Vasavada, A.R., Kamp, L., Drossart, P., Irwin, P., Nixon, C., Carlson, R.W., 2000. Proximate humid and dry regions in Jupiter's atmosphere indicate complex local meteorology. Nature 405, 158-160.

Sanchez-Lavega, A., Acarreta, J.R., Hueso, R., Rojas, J.F., Lecacheux, J., Colas, F., Gomez, J.M, 1999. An overview of Saturn's equatorial storms: 1990-1997. Astrophys. Space Sci. 263, 351-354.

Sanchez-Lavega, A., Colas, F., Lecacheux, J., Laques, P., Miyazaki, I., Parker, D., 1991. The Great White Spot and disturbances in Saturn's equatorial atmosphere during 1990. Nature 353, 397-401.

Sanchez-Lavega, A., Lecacheux, J., Gomez, J.M., Colas, F., Laques, P., Noll, K., Gilmore, D., Miyazaki, I., Parker, D., 1996. Large-scale storms in Saturn's atmosphere during 1994. Science 271, 631-634.

Sanchez-Lavega, A., Perez-Hoyos, S., Rojas, J.F., Hueso, R., French, R.G., 2003. A strong decrease in Saturn's equatorial jet at cloud level. Nature 423, 623-625.

Sayanagi, K.M., Showman, A.P., Kursinski, E.R., 2004. Effect of a large convective storm on the atmospheric dynamics of a jovian planet. Bull. Amer. Astron. Soc. 36**,** 1135.

Sommeria, J., Meyers, S.D., Swinney, H.L., 1989. Laboratory model of a planetary eastward jet. Nature 337, 58-61.

Stoker, C.R., 1986. Moist convection: a mechanism for producing the vertical structure of the jovian equatorial plumes. Icarus 67, 106-125.

Sun, Z.-P., Schubert, G., Glatzmaier, G.A, 1993. Banded surface flow maintained by convection in a model of the rapidly rotating giant planets. Science 260, 661-664.

Weidenschilling, S.J., Lewis, J.S., 1973. Atmospheric and cloud structures of the jovian planets. Icarus 20, 465-476.

Williams, G.P., 1978. Planetary circulation: 1. Barotropic representation of jovian and terrestrial trubulence. J. Atmos. Sci. 35, 1399-1426.

Yair,Y., Levin, Z., Tzivion, S., 1992. Water-cumulus in Jupiter's atmosphere: numerical experiments with an axis-symmetric cloud model. Icarus 98, 72-81.

Yair, Y., Levin, Z., Tzivion, S., 1995. Microphysical processes and dynamics of a jovian thundercloud. Icarus 114, 278-299.

Yano, J.-I., Talagrand, O., Drossart, P., 2003. Origins of atmospheric zonal winds. Nature 421, 36-36.

Youssef, A., Marcus, P.S., 2003. The dynamics of jovian white ovals from formation to merger. Icarus 162, 74-93.

Figure 4.1 Dependence of QG model on different initial random patterns. **a** and **c are** two initial random patterns with different amplitudes and length scales. **b** and **d** are the corresponding steady patterns. For these runs the parameter values are: $T_{mc} = 1$ day, $R_{mc} = 1000$ km, $S_{mc} = 1.0 \times 10^{-9}$ s^{-2}, $L_d = 5000$ km, and $\kappa_h = 10^3$ m^2 s^{-1}. The domain size is 32000 km in the x and y directions, which is equivalent to 30 longitude degrees (at latitude 30°) in the x direction and 25 latitude degrees in the y direction.

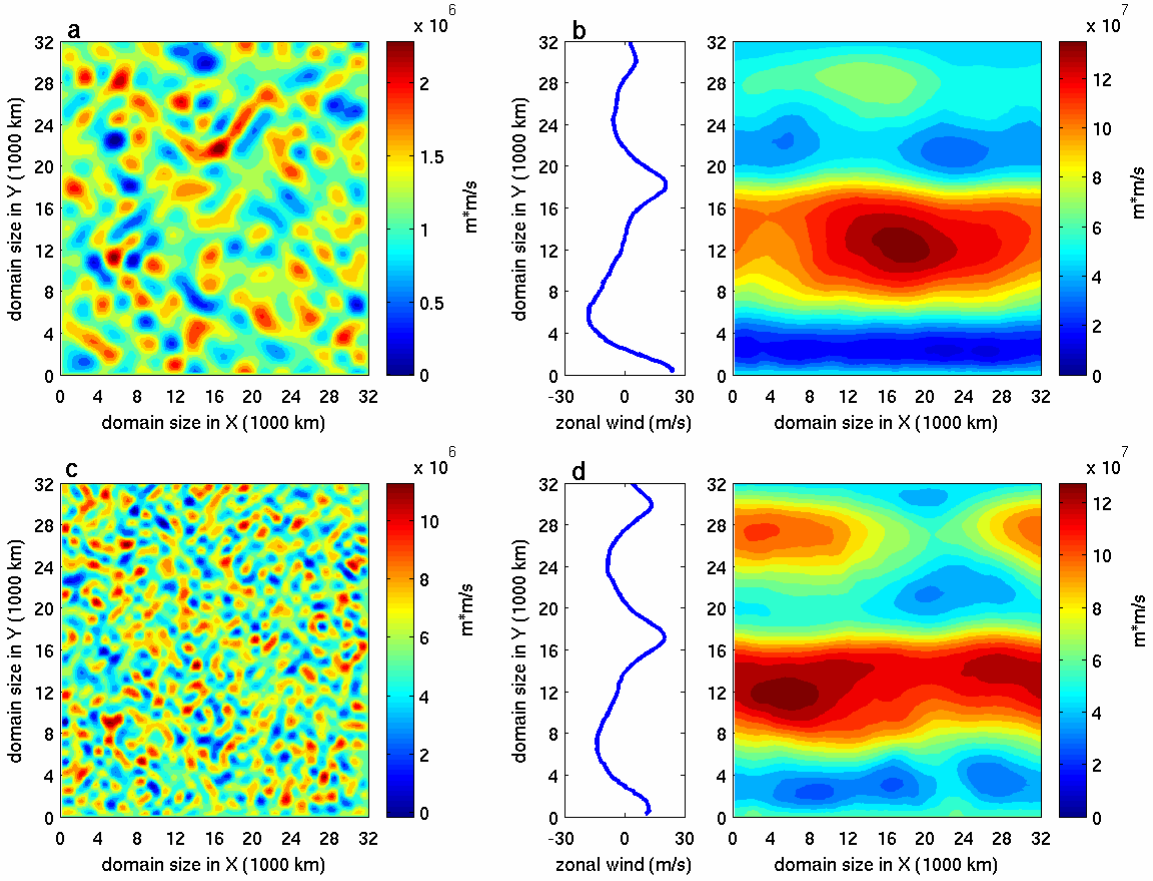

Figure 4.2 Dependence of QG model on the spatial resolution and domain size. **a** , steady state of the experiment shown in Fig.1 with space resolution 250 km and domain size 32,000 km in both directions (30 longitude degrees in the x direction and 25 latitude degrees in the y direction). **b,** steady state with space resolution 125 km and domain size 32,000 km in both directions (30 longitude degrees in the x direction and 25 latitude degrees in the y direction). **c,** steady state with space resolution 250 km and domain size 64,000 km in both directions (60 longitude degrees in the x direction and 50 latitude degrees in the y direction). **d,** steady state with space resolution 250 km and domain size 32,000 km in y direction and 128,000 km in x direction (120 longitude degrees in the x direction and 25 latitude degrees in the y direction). In all experiments of this figure, we use the same initial random pattern as in Fig. 1a and the same group of parameters as in Fig. 1.

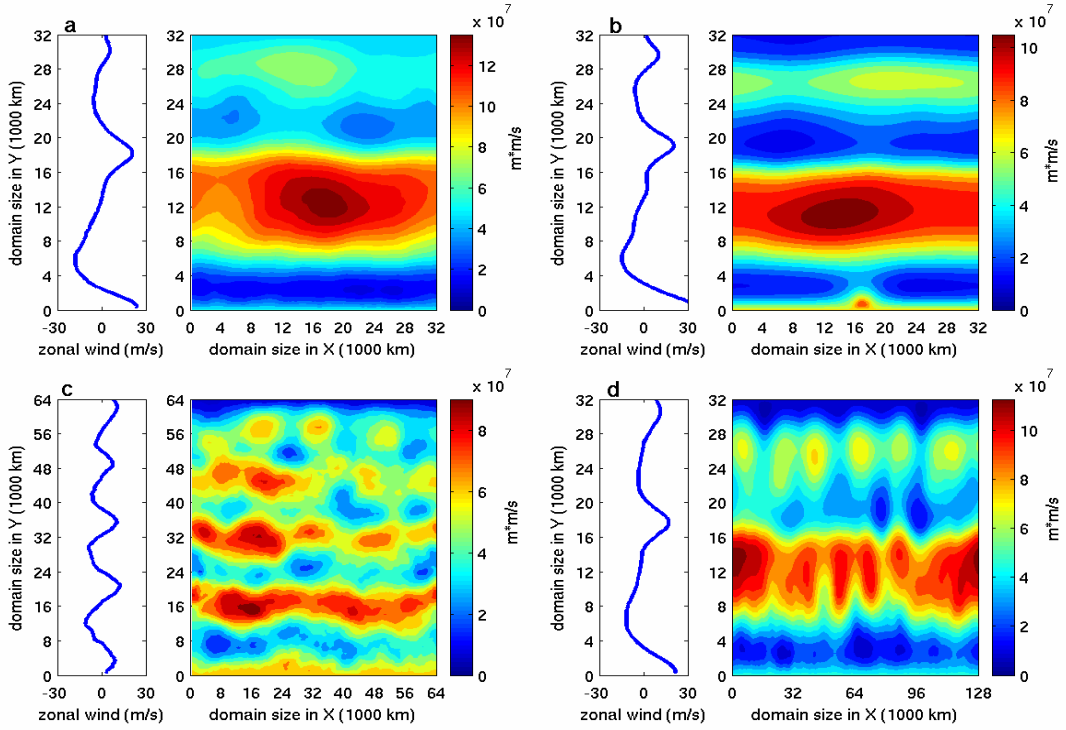

Figure 4.3 Time evolution of streamfunction pattern for $T_{mc} = 1$ day, $R_{mc} = 1000$ km, $S_{mc} = 1.1 \times 10^{-9}$ s^{-2}, $L_d = 5000$ km, and $\kappa_h = 10^3$ m^2 s^{-1}. **a,** time = 0 (initial random pattern). **b,** time = 1 hour. **c,** time = 1 day. **d,** time = 1 month. **e,** time = 1 year. **f,** time = 5 years. In this and all other experiments of Jupiter the values of S_r and β are 2.14×10^{-14} s^{-2} and 4.26×10^{-12} m^{-1} s^{-1}, respectively. The positions of all MCs between 1 year and 5 years are shown in **f** (each bright cross 'x' represents the position of one MC)**.** The domain size is 32000 km in the x and y directions, which is equivalent to 30 longitude degrees in the x direction and 25 latitude degrees in the y direction.

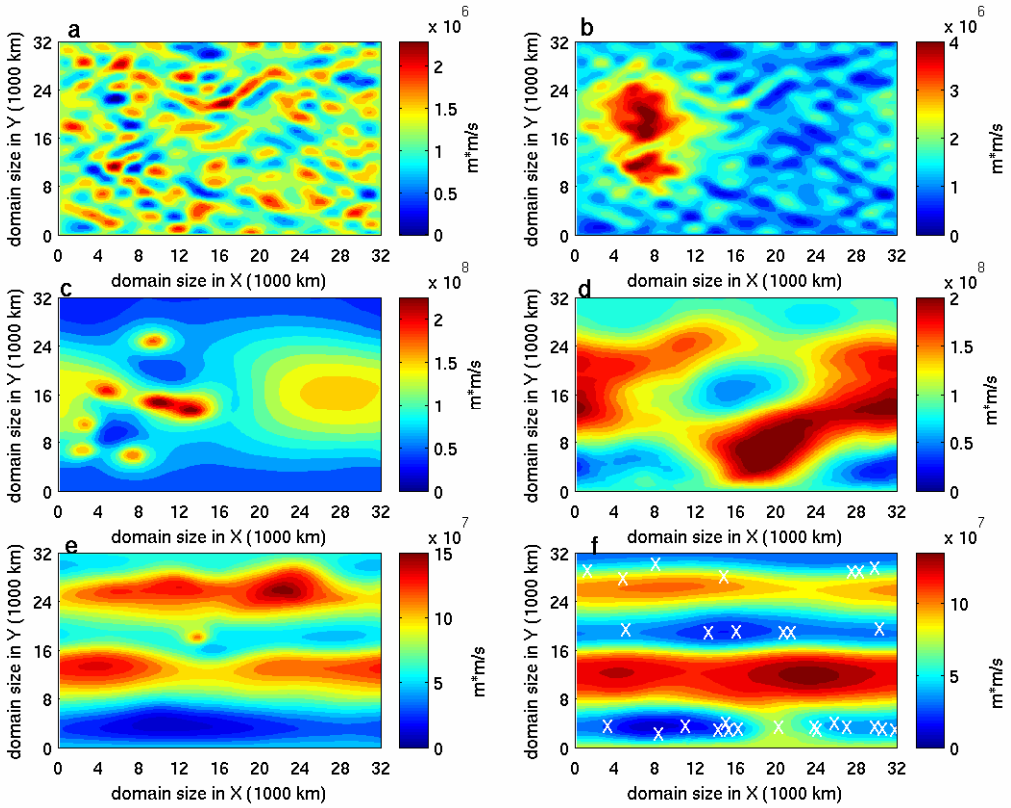

Figure 4.4 Zonal wind profile for the steady state portion of the experiment shown in Fig.3.

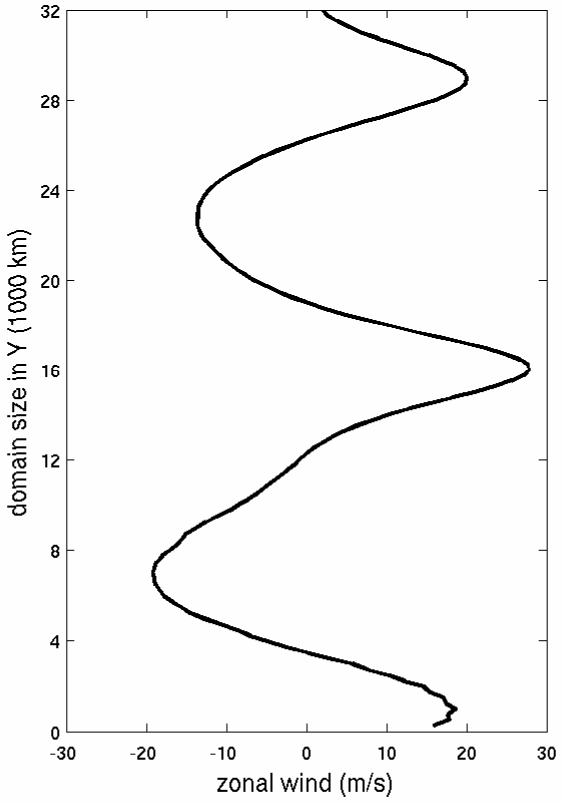

Figure 4.5 Time series of global averaged energy for the experiment shown in Fig. 3: potential energy PE (solid line), total kinetic energy KE (dashed line), and zonal kinetic energy KE_{zonal} (dotted line) – the part associated with the zonal wind U. The initial energies are not zero, but they are small compared to the energies in the steady state.

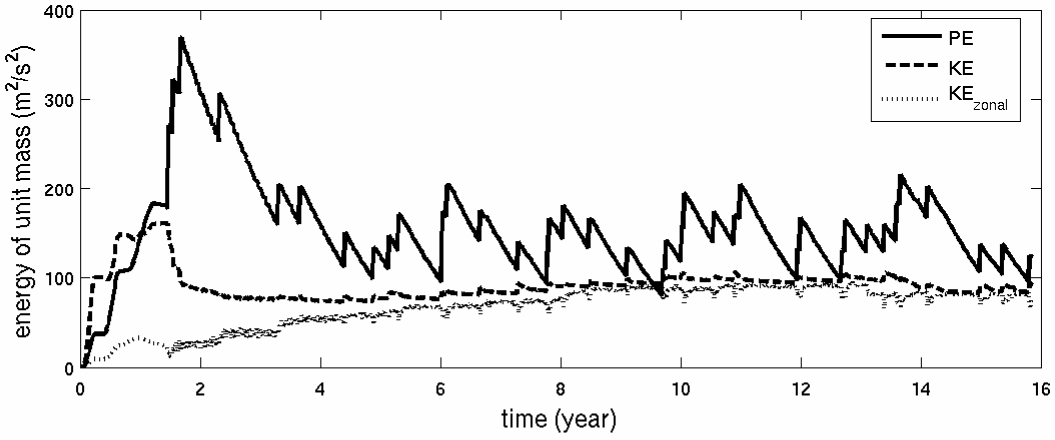

Figure 4.6 Parameter space explorations. **a,** Width of jets L_{jet} (half wavelength of zonal wind profile) as a function of different parameters: (I) radius of deformation L_d (unit: km); (II) horizontal eddy diffusion coefficient κ_h (unit: m^2s^{-1}); (III) lifetime T_{mc} of MC (unit: day); (IV) radius L_{mc} of MC (unit: km); (V) amplitude S_{mc} of vorticity source of MC (unit: 10^{-12} s^{-2}). **b,** Same as **a** except for the amplitude of jets V_{jet} . The asterisk symbol * in **a** and **b** represents the experiment with the standard values ($L_d = 5000$ km, $\kappa_h = 10^3$ $m^2 s^{-1}$, $T_{mc} = 1$ day, $R_{mc} = 1000$ km and $S_{mc} = 2.14 \times 10^{-10}$ s^{-2}).

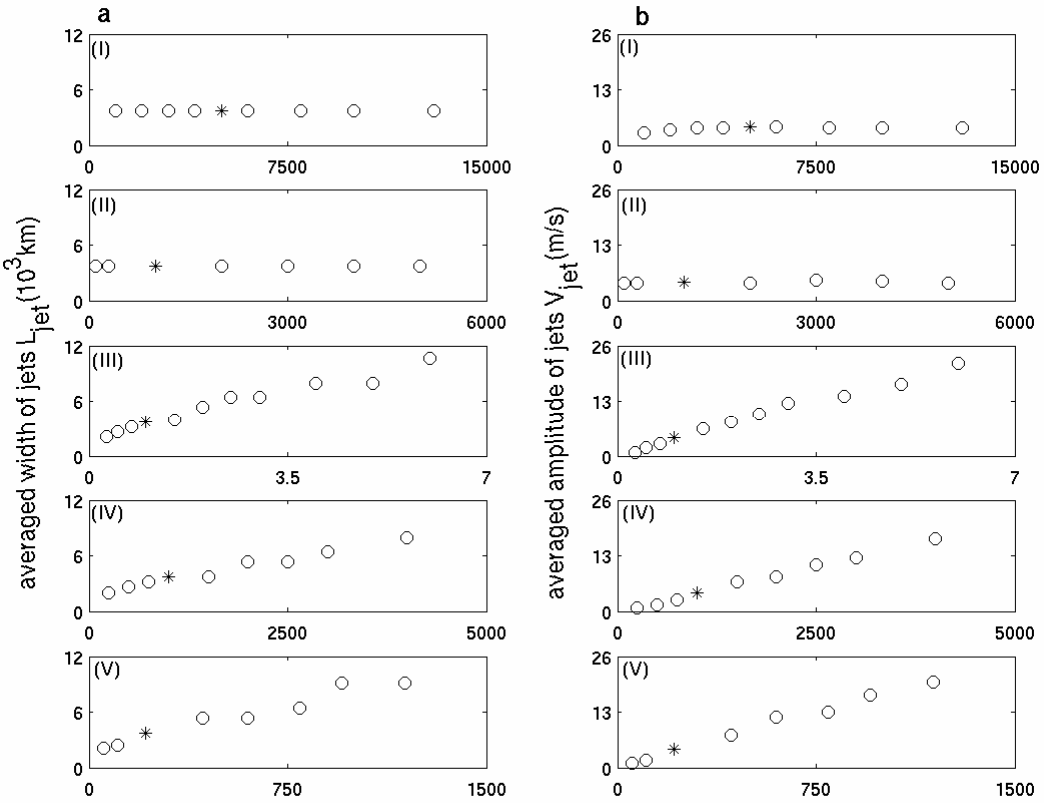

Figure 4.7 The ratios L_{jet}/L and V_{jet}/V for different values of the parameters associated with MC. **a,** L_{jet}/L. **b,** V_{jet}/V. (I) only changing the lifetime of MC; (II) only changing the radius of MC; (III) only changing the average amplitude of MC. The asterisk symbol * in **a** and **b** represents the experiment with the standard values.

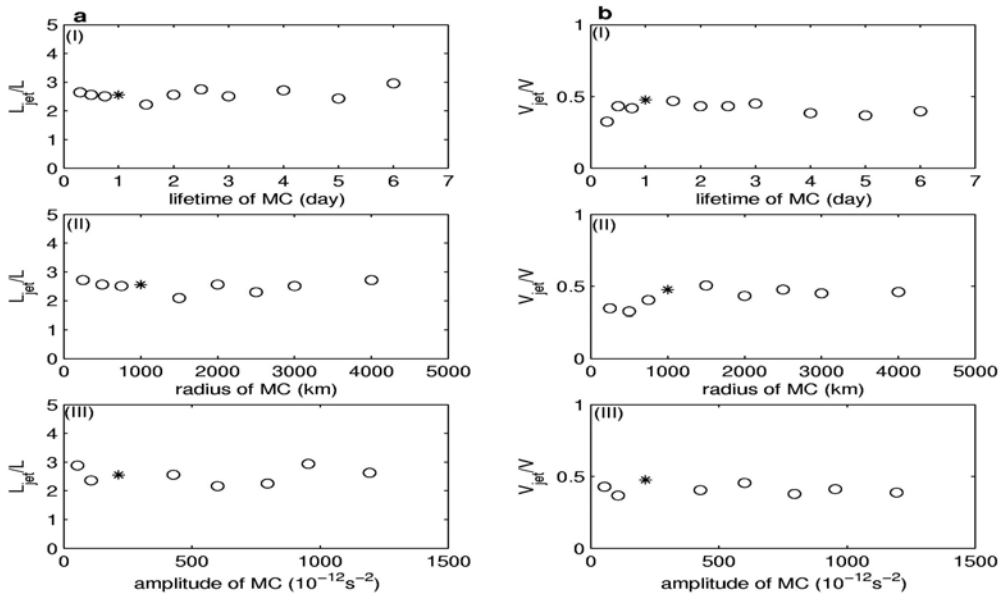

Figure 4.8 Exploring the ratio U_{yy}/β in the space of lifetime and radius of MC, for four different amplitudes of MC. **a,** $S_{mc}=1.0\times10^{-10}$ s^{-2}. **b,** $S_{mc}=2.0\times10^{-10}$ s^{-2}. **c,** $S_{mc}=3.0\times10^{-10}$ s^{-2}. **d,** $S_{mc}=4.0\times10^{-10}$ s^{-2}.

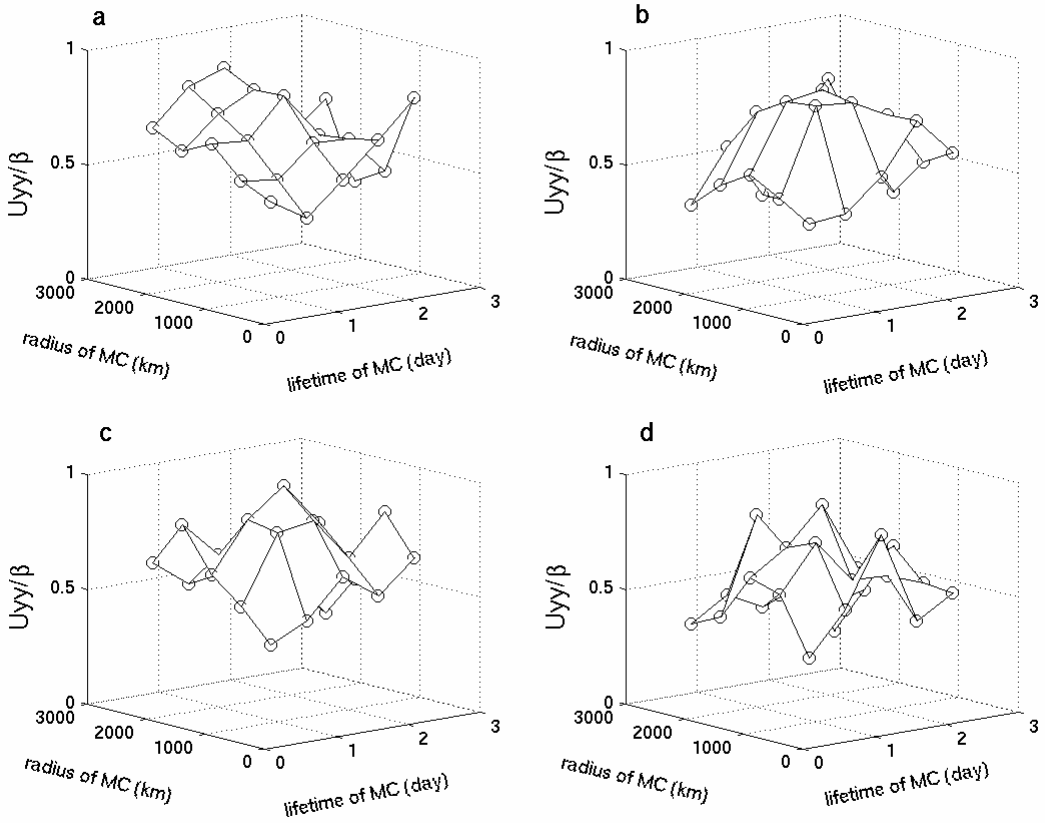

Figure 4.9 Observed and simulated zonal wind profiles in the middle latitudes of Jupiter. **a,** Observed wind profile in the middle latitudes of Jupiter from Cassini. The range of latitudes is chosen with the same size as the domain size of our experiments. **b,** Modeled zonal wind profile of Jupiter with same parameters in Fig.1 except for westward deep flow $U_2 = -80$ m/s. The thin solid curves are defined by $d^2U/dy^2 = \beta$, and are centered on the westward jet maxima.

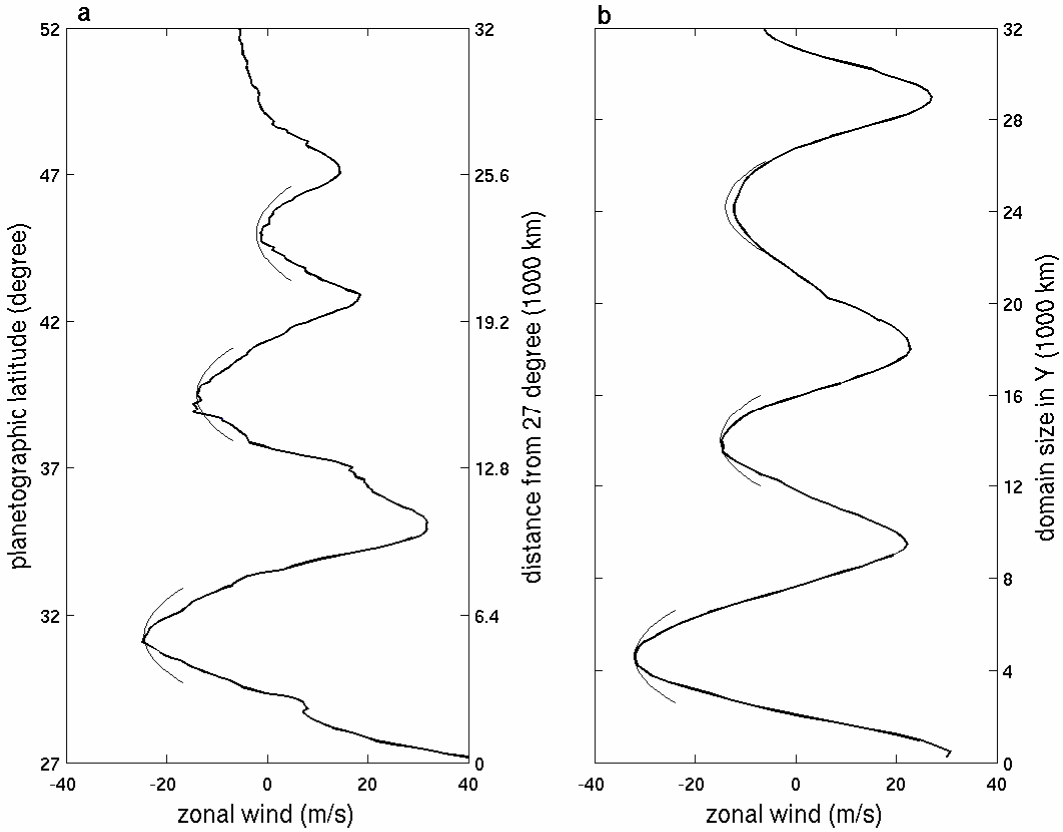

Figure 10 Observed and simulated zonal wind profiles in the middle latitudes of Saturn. **a,** Observed wind profile in the middle latitudes of Saturn from Voyager. **b,** Modeled zonal wind profile of Saturn with T_{mc} = 1 day, L_{mc}=4000 km, $S_r = 1.26\times10^{-15}$ s^{-2}, $S_{mc} = 4.2\times10^{-11}$ s^{-2} (fractional area $C_{mc} = 3.0\times10^{-5}$), L_d = 5000 km, and κ_h=10^3 $m^2\,s^{-1}$.